

**SYNTHESIS AND CHARACTERIZATION OF  
SCHIFF BASE LIQUID CRYSTALS WITH  
BENZOTHAZOLE RING**

**KEW HO YANG**

**BACHELOR OF SCIENCE (HONS) CHEMISTRY**

**FACULTY OF SCIENCE**

**UNIVERSITI TUNKU ABDUL RAHMAN**

**MAY 2025**

**KEW HO YANG**

**B.Sc. (Hons) Chemistry**

**2025**

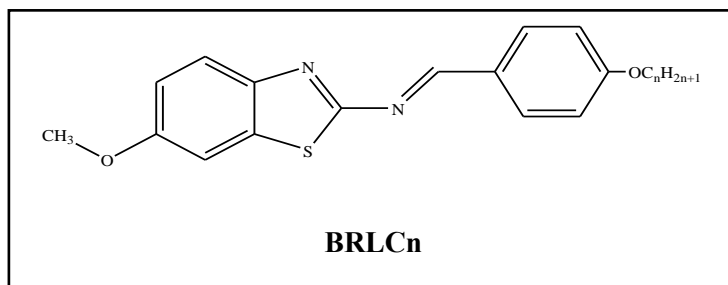
**SYNTHESIS AND CHARACTERIZATION OF SCHIFF BASE LIQUID  
CRYSTALS WITH BENZOTHAZOLE RING**

**By KEW HO YANG**

A project report submitted to the Department of Chemical Science,  
Faculty of Science,  
Universiti Tunku Abdul Rahman,  
in partial fulfillment of the requirements for the degree of  
Bachelor of Science (Honours) Chemistry  
May 2025

## ABSTRACT

A series of benzothiazole ring Schiff base ether liquid crystals (*E*)-1-(4-(alkyloxy)phenyl)-*N*-(6-methoxybenzo[d]thiazol-2-yl)methanimine, **BRLCn** ( $C_nH_{2n+1}O-$ , where  $n = 12, 14, 16$ , and  $18$ ) were successfully synthesized, characterized and the mesomorphic properties were investigated.



Two major steps were involved for synthesis. The first step is the Schiff base condensation between 2-amino-6-methoxy benzothiazole and 4-hydrobenzaldehyde with the aid of glacial acetic acid formed imine linkage (C=N) between two aromatic benzene rings. The second step is the formation of ether linkage, **BRLCn** through the etherification between **BMB1** and bromoalkane.

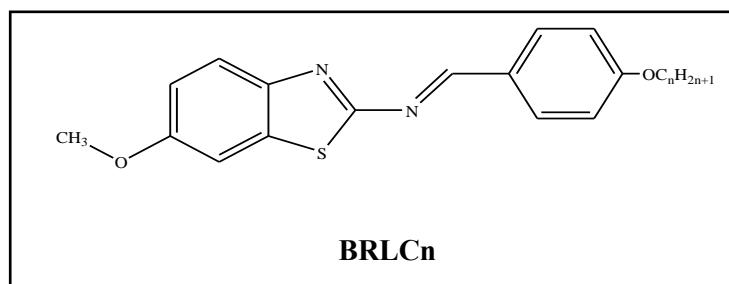
The molecular structures of the synthesized compounds were determined using Fourier Transform (FTIR), 1D NMR (<sup>1</sup>H and <sup>13</sup>C) and 2D NMR (COSY, HMBC, and HMQC). The mesomorphic properties of synthesized compounds were identified using Differential Scanning Calorimetry (DSC) as well as the photophysical properties using UV-Vis spectroscopy. All the compounds **BRLCn** (where  $n = 12, 14, 16$ , and  $18$ ) exhibit two liquid crystal phases.

Keywords: Synthesis, Schiff Base, Liquid Crystals, NMR Spectroscopy, Differential Scanning Calorimetry

Subject Area: QD241-441 Organic Chemistry

## ABSTRAK

Siri ester berpangkalan bes Schiff benzothiazole, (*E*)-1-(4-(alkyloxy)phenyl)-*N*-(6-methoxybenzo[d]thiazol-2-yl)methanimine, **BRLCn** di mana *n* mewakili bilangan atom karbon dalam rantai alkyloxy telah dihasilkan dengan berjaya, dicirikan, dan sifat mesomorpik telah disiasat.



Dua langkah utama terlibat dalam sintesis ini. Langkah pertama adalah kondensasi bes Schiff antara 2-amino-6-methoxy benzothiazole and 4-hydrobenzaldehyde dengan bantuan asid asetik untuk menghasilkan ikatan imine ( $\text{C}=\text{N}$ ) di antara dua benzena aromatik. Langkah kedua adalah pembentukan ether bes Schiff, **BRLCn** melalui eterifikasi antara BMB1 dan bromoalkana.

Struktur molekul sebatian yang disintesis ditentukan menggunakan Transformasi Fourier (FTIR), 1D NMR ( $^1\text{H}$  dan  $^{13}\text{C}$ ), 2D NMR (COSY, HMBC, dan HMQC). Sifat mesomorfik sebatian yang disintesis dikenal pasti menggunakan Kalorimeter Pembezaan Pengimbasan (DSC) serta sifat fotofisika menggunakan spektroskopi UV-Vis. Semua sebatian siri **BRLCn**, di mana  $n = 12, 14, 16$ , dan  $18$  menunjukkan dua fasa kristal cecair.

Kata Kunci: Sintesis, Bes Schiff, Kristal Cecair, Spektroskopi NMR, Kalorimeter Pembezaan Pengimbasan

Bidang Subjek: QD241–441 Kimia Organik

## **ACKNOWLEDGEMENTS**

First and foremost, I would like to express my heartfelt gratitude to my supervisor, Assistant Professor Dr. Ha Sie Tiong, for his invaluable advice, guidance, and encouragement. His support was instrumental in ensuring the smooth progress of my project. I sincerely appreciate his generosity in sharing his knowledge and providing me with essential insights throughout my FYP research.

Additionally, I extend my appreciation to the Faculty of Science at Universiti Tunku Abdul Rahman for the support provided in completing my research on liquid crystals. A special thanks to Mr. Seou Chi Kien for his continuous guidance and advice, which greatly enhanced my laboratory skills and analytical abilities during my project. I am also grateful to my senior, Ms. Salini A/P Puranachantiran, for sharing her expertise and laboratory techniques with me.

Lastly, I wish to express my deepest gratitude to my family for their financial support, without which I would not have had the opportunity to pursue my university education. My sincere thanks also go to my friends, whose encouragement and support, both mentally and physically, motivated me throughout this journey.

## **COPYRIGHT**

This final year project is submitted in partial fulfillment of the requirements for the degree of Bachelor of Science (Honours) Chemistry at Universiti Tunku Abdul Rahman (UTAR). This final year project represents the work of the author, except where due acknowledgment has been made in the text. No part of this final year project may be reproduced, stored, or transmitted in any form or by any means, whether electronic, mechanical, photocopying, recording, or otherwise, without the prior written permission of the author or UTAR, in accordance with UTAR's Intellectual Property Policy.

© 2025, Kew Ho Yang. All right reserved

## TABLE OF CONTENTS

	<b>Page</b>
<b>ABSTRACT</b>	<b>ii</b>
<b>ABSTRAK</b>	<b>iii</b>
<b>ACKNOWLEDGEMENTS</b>	<b>iv</b>
<b>COPYRIGHT</b>	<b>v</b>
<b>TABLE OF CONTENTS</b>	<b>vi</b>
<b>LIST OF TABLES</b>	<b>x</b>
<b>LIST OF FIGURES</b>	<b>xi</b>
<b>LIST OF ABBREVIATIONS</b>	<b>xiv</b>
<b>LIST OF APPENDICES</b>	<b>xv</b>
 <b>CHAPTER</b>	
<b>1 INTRODUCTION</b>	
1.1 Introduction to Liquid Crystal	1
1.2 History of Liquid Crystal	3
1.3 Categories of Liquid Crystal Phases	
1.3.1 Nematic Phase	5
1.3.2 Cholesteric Phase	5
1.3.3 Smectic Phase	6
1.4 Molecular Pattern and Chemical Framework of Liquid Crystal	8
1.5 Objectives	10
 <b>2 LITERATURE REVIEW</b>	
2.1 Schiff Base Liquid Crystals	11
2.2 Relationship between Molecular Structure and Mesomorphic Behaviour	
2.2.1 Effects of Alkyl Chain Length on Mesomorphic Properties	13
2.2.2 Effects of Core group on Mesomorphic Properties	18
2.2.3 Effects of Terminal Group on Mesomorphic Properties	21
2.2.4 Effects of Linkage Group on Mesomorphic Properties	23

<b>3</b>	<b>METHODOLOGIES</b>	
3.1	Chemicals	29
3.2	Instrumentations	30
3.3	Experimental Synthesis	31
3.3.1	Preparation of ( <i>E</i> )-4-(((6-methoxybenzo[d]thiazol-2-yl)imino)methyl)phenol, <b>BMB1</b>	32
3.3.2	Preparation of ( <i>E</i> )-1-(4-(alkyloxy)phenyl)- <i>N</i> -(6-methoxybenzo[d]thiazol-2-yl)methanimine, <b>BRLCn</b> (n = 12, 14, 16 and 18)	32
3.3.2.1	Preparation of ( <i>E</i> )-1-(4-(dodecyloxy)phenyl)- <i>N</i> -(6-methoxybenzo[d]thiazol-2-yl)methanimine, <b>BRLC12</b>	32
3.3.2.2	Preparation of ( <i>E</i> )-1-(4-(tetradecyloxy)phenyl)- <i>N</i> -(6-methoxybenzo[d]thiazol-2-yl)methanimine, <b>BRLC14</b>	33
3.3.2.3	Preparation of ( <i>E</i> )-1-(4-(hexadecyloxy)phenyl)- <i>N</i> -(6-methoxybenzo[d]thiazol-2-yl)methanimine, <b>BRLC16</b>	33
3.3.2.4	Preparation of ( <i>E</i> )-1-(4-(octadecyloxy)phenyl)- <i>N</i> -(6-methoxybenzo[d]thiazol-2-yl)methanimine, <b>BRLC18</b>	34



3.4	Characterizations	
3.4.1	Thin Layer Chromatography (TLC) Analysis	34
3.4.2	Fourier Transform (FTIR)	35
3.4.3	Nuclear Magnetic Resonance (NMR)	35
3.4.4	Differential Scanning Calorimetry (DSC)	36
3.4.5	Photophysical Properties Analysis	36
3.4.6	Melting Point Apparatus	37
4	<b>RESULTS AND DISCUSSION</b>	
4.1	Mechanism involved	
4.1.1	Synthesis of ( <i>E</i> )-4-(((6-methoxybenzo[d]thiazol-2-yl)imino)methyl)phenol, <b>BMB1</b>	38
4.1.2	Synthesis of ( <i>E</i> )-1-(4-(alkyloxy)phenyl)- <i>N</i> -(6-methoxybenzo[d]thiazol-2-yl)methanimine, <b>BRLCn</b> (n = 12, 14, 16 and 18)	39
4.2	Thin Layer Chromatography (TLC) Analysis	41
4.3	Fourier Transform (FTIR)	
4.3.1	Fourier Transform Infrared Spectroscopy (FTIR) Analysis of 2A6MB, 4HB and <b>BMB1</b>	43
4.3.2	Fourier Transform Infrared Spectroscopy (FTIR) Analysis of <b>BRLCn</b>	45
4.3.3	Attenuated Total Reflection (ATR-FTIR) Analysis of <b>BRLCn</b>	49
4.4	Nuclear Magnetic Resonance (NMR)	
4.4.1	<sup>1</sup> H NMR Spectral Analysis	53
4.4.2	<sup>13</sup> C NMR Spectral Analysis	57
4.4.3	2D COSY NMR Spectral Analysis	61
4.4.4	2D HMQC NMR Spectral Analysis	64
4.4.5	2D HMBC NMR Spectral Analysis	68

4.5	Liquid Crystalline Properties	
4.5.1	Differential Scanning Calorimetry Analysis	72
4.5.2	Effects of Number of Carbons at the Alkyloxy Chain on the Transition Temperature	76
4.6	Photophysical Properties Analysis	78
<b>5</b>	<b>CONCLUSION AND FURTHER STUDY</b>	<b>84</b>
	<b>REFERENCES</b>	<b>87</b>

## LIST OF TABLES

Table		Page
2.1	The phase behavior <b>(S)-MHOBSn</b> obtained during heating (Ossowska-Chrusciel et al., 2004)	17
2.2	Overall transition temperatures observed during heating for the of $\omega$ -unsaturated derivative (Fornasieri, Guittard, and G�ribaldi, 2003).	19
3.1	Chemical reagents used and their origin	29
3.2	Instruments used and their corresponding applications	30
4.1	R <sub>f</sub> values for the series of <b>BRLCn</b> compounds	42
4.2	FTIR spectral data of 2A6MB, 4HB, <b>BMB1</b>	48
4.3	FTIR spectral data of <b>BRLCn</b> compounds	48
4.4	ATR-FTIR spectral data of <b>BRLCn</b> compounds	52
4.5	Details data of <sup>1</sup> H NMR for <b>BRLC16</b> in CDCl <sub>3</sub>	55
4.6	Details data of <sup>13</sup> C NMR for <b>BRLC16</b> in CDCl <sub>3</sub>	59
4.7	<sup>1</sup> H- <sup>1</sup> H correlations from the 2D COSY NMR for <b>BRLC16</b>	62
4.8	<sup>1</sup> H- <sup>13</sup> C correlations from the 2D HMQC NMR for <b>BRLC16</b>	66
4.9	<sup>1</sup> H- <sup>13</sup> C correlations from the 2D HMBC NMR for <b>BRLC16</b>	70
4.10	Transition temperature for heating and cooling of the compound <b>BRLCn</b> , where n = 12, 14, 16, and 18	75
4.11	Molar absorptivity values for the <b>BRLCn</b> compounds at 284 nm and 344 nm	82

## LIST OF FIGURES

Figure		Page
1.1	Arrangement of molecules	2
1.2	(a) Photo of Friedrich Reinitzer and (b) Otto Lehmann; (c) Structure of Cholesteryl benzoate (Hussain, Pina and Roque, 2009)	4
1.3	Schematic representation of molecules distribution in (a) Nematic Phase; (b) Cholesteric Phase; (c) Smectic Phase (Smartglass World, 2023)	7
1.4	Texture and molecular arrangement (a) Smectic A; (b) Smectic C; and (c) Smectic C* (Dierking, 2003)	7
1.5	Typical rod-like shape of a liquid crystal molecule (Khoo, 2007)	9
1.6	Molecular structure of series <b>BRLCn</b> compounds, where n = 12, 14, 16, 18	10
2.1	General mechanism of formation of Schiff Base (Subasi, 2022)	12
2.2	Structure of <b>nCIAB</b> where n = 2-8, 10, 12, 14, 16, 18	14
2.3	Polarizing optical microscope of <b>PB1</b> showing fan-shaped texture of SmA; <b>PB2</b> & <b>PB3</b> showing focal conic fan-shaped texture of SmA phase at 254, 201 and 203 °C respectively upon cooling (Lee, Salleh & Cheng, 2021).	16
2.4	Structure of (5)- (+)-4-(1 -methyloheptyloxy)biphenyl-(4'-alkylphenyl)- thiobenzoates, <b>(S)-MHOBsn</b> where n, number of carbons = 4 to 10 (Ossowska-Chrusciel et al., 2004)	17
2.5	Structure of three series of $\omega$ -unsaturated compounds <b>Phm, Bm and PhBm</b> (m = 1,9; R <sub>F</sub> = C <sub>6</sub> F <sub>13</sub> )	18
2.6	Comparison of the temperature ranges of the mesophase for the compound <b>Phm, Bm, PhBm</b>	19
2.7	DSC curves for allyloxy compound <b>B1</b> (heating and cooling rate: 10°C min <sup>-1</sup> ) and <b>PhB1</b> first heating	20

2.8	Structure of 3-hydroxy-4-{[4-X-substitutedphenyl)imino]methyl}phenyloctadecanoate, <b>SB-X</b> (Ha <i>et al.</i> , 2010c)	22
2.9	Structure of 4-chlorobenzylidene-4'-alkanoyloxyaniline, <b>nCIAB</b> (where n = 2-8, 10, 12, 14, 16, 18) (Ong and Ha, 2013)	23
2.10	Structure of alkyl 4-{[(4-chlorophenyl)imino]methyl}benzoates, <b>nCICBA</b> (where n = 2-16) (Ha <i>et al.</i> , 2010a)	24
2.11	DSC thermograms of <b>nCIAB</b> (n = 2, 5, 6, 8) during cooling cycles (Ong and Ha, 2013)	25
2.12	DSC thermogram of undecyl 4-{[(4-chlorophenyl)imino]methyl}benzoate, <b>nCICBA</b> (n = 11) during heating and cooling cycles (Ha <i>et al.</i> , 2010a)	25
2.13	Schematic illustration of prepared hydrogen-bonded starshaped assemblies for the systematic investigation of the impact of the linking group on the liquid crystalline behaviour (Pfletscher, Mezger and Giese, 2018)	26
2.14	Overview of the phase transition (A) of nonyl-based HBA representatives obtained via POM upon cooling. A comparison of the observing findings with different linkage parts indicates the structural differences among each other (Pfletscher, Mezger and Giese, 2018)	28
3.1	Overall synthesis route for <b>BRLCn</b> formations	31
4.1	Mechanism for Schiff base condensation between 2A6MB and 4HB (Sani, Na'ibi and Dailami, 2018)	39
4.2	Williamson etherification for the formation of <b>BRLCn</b> (Ashenhurst, 2025)	40
4.3	TLC Plate for <b>BRLC16</b>	42
4.4	FTIR spectra of <b>BMB1</b> , 2A6MB, 4HB	46
4.5	FTIR spectrum of <b>BRLC16</b>	47
4.6	ATR-FTIR spectrum of <b>BRLC16</b>	50
4.7	Comparison of ATR-FTIR spectra for <b>BRLCn</b>	51

4.8	$^1\text{H}$ NMR spectrum for <b>BRLC16</b>	56
4.9	$^{13}\text{C}$ NMR spectrum for <b>BRLC16</b>	60
4.10	2D COSY NMR spectrum for <b>BRLC16</b>	63
4.11	2D HMQC NMR spectrum for <b>BRLC16</b>	67
4.12	2D HMBC NMR spectrum for <b>BRLC16</b>	71
4.13	DSC thermogram for <b>BRLC16</b>	72
4.14	Plot of transition temperature against number of carbons in alkyloxy chain	77
4.15	Graph of absorbance against wavelength between <b>BMB1</b> and <b>BRLC16</b>	80
4.16	Graph of absorbance against concentration for <b>BRLC16</b> at 284 nm	81
4.17	Graph of absorbance against concentration for <b>BRLC16</b> at 344 nm	82

## LIST OF ABBREVIATIONS

<b>BRLC12</b>	( <i>E</i> )-1-(4-(dodecyloxy)phenyl)- <i>N</i> -(6-methoxybenzo[d]thiazol-2-yl)methanimine
<b>BRLC14</b>	( <i>E</i> )-1-(4-(tetradecyloxy)phenyl)- <i>N</i> -(6-methoxybenzo[d]thiazol-2-yl)methanimine
<b>BRLC16</b>	( <i>E</i> )-1-(4-(hexadecyloxy)phenyl)- <i>N</i> -(6-methoxybenzo[d]thiazol-2-yl)methanimine
<b>BRLC18</b>	( <i>E</i> )-1-(4-(octadecyloxy)phenyl)- <i>N</i> -(6-methoxybenzo[d]thiazol-2-yl)methanimine
<b>BRLCn</b>	( <i>E</i> )-1-(4-(alkanolyoxy)phenyl)- <i>N</i> -(6-methoxybenzo[d]thiazol-2-yl)methanimine
<b>BMB1</b>	( <i>E</i> )-4-(((6-methoxybenzo[d]thiazol-2-yl)imino)methyl)phenol
<b>2A6MB</b>	2-amino-6-methoxybenzothiazole
<b>4HB</b>	4-hydroxybenzaldehyde
<b>DMF</b>	<i>N,N</i> -Dimethylformamide
<b>CDCl<sub>3</sub></b>	Deuterated chloroform
<b>TLC</b>	Thin Layer Chromatography
<b>FTIR</b>	Fourier Transform Infrared
<b>ATR</b>	Attenuated Total Reflectance
<b><sup>1</sup>H NMR</b>	Proton Nuclear Magnetic Resonance
<b><sup>13</sup>C NMR</b>	Carbon-13 Nuclear Magnetic Resonance
<b>COSY</b>	Homonuclear Correlation Spectroscopy
<b>HMBC</b>	Heteronuclear Multiple Bond Correlation
<b>HMQC</b>	Heteronuclear Multiple Quantum Coherence
<b>DSC</b>	Differential Scanning Calorimetry
<b>TMS</b>	Tetramethylsilane
<b>Cr</b>	Crystal
<b>LC</b>	Liquid crystal
<b>I</b>	Isotropic

## LIST OF APPENDICES

	<b>Page</b>
A1 FTIR Spectrum of 2-amino-6-methoxy benzothiazole	97
A2 FTIR Spectrum of 4-hydroxybenzaldehyde	98
A3 FTIR Spectrum of <b>BMB1</b>	99
A4 FTIR Spectrum of <b>BRLC12</b>	100
A5 FTIR Spectrum of <b>BRLC14</b>	101
A6 FTIR Spectrum of <b>BRLC18</b>	102
A7 ATR-FTIR Spectrum of <b>BRLC12</b>	103
A8 ATR-FTIR Spectrum of <b>BRLC14</b>	104
A9 ATR-FTIR Spectrum of <b>BRLC18</b>	105
A10 <sup>1</sup> H NMR spectrum of <b>BRLC14</b>	106
A11 <sup>13</sup> C NMR spectrum of <b>BRLC14</b>	107
A12 2D COSY NMR spectrum of <b>BRLC14</b>	108
A13 2D HMQC NMR spectrum of <b>BRLC14</b>	109
A14 2D HMBC NMR spectrum of <b>BRLC14</b>	110
A15 DSC thermogram of <b>BRLC12</b>	111
A16 DSC thermogram of <b>BRLC14</b>	112
A17 DSC thermogram of <b>BRLC18</b>	113
A18 Graph of absorbance against concentration of <b>BRLC12</b> at 284 and 344nm	114
A19 Graph of absorbance against concentration of <b>BRLC14</b> at 284 and 344nm	115
A20 Graph of absorbance against concentration of <b>BRLC18</b> at 284 and 344nm	116



## CHAPTER 1

### INTRODUCTION

#### 1.1 Introduction to Liquid Crystal

Liquid crystals represent an intermediate phase of matter, displaying hybrid characteristics that bridge the ordered structure of solids and the fluidity of liquids. They possess an intermediate phase where molecules can diffuse like a liquid while still retaining some structural order like a solid crystalline phase (Collings & Hird, 1998; Khoo, 2007). This mesophase is characterized by the molecular order and mobility of liquid crystal molecules at the supramolecular level, which influence their structural, optical, and mechanical properties (Kumar & Kang, 2005).

As illustrated in Figure 1.1 (a), in the crystalline solid phase, the constituent mesogens are typically anisotropic rod- or disc-shaped molecules. They adopt a perfectly ordered three-dimensional arrangement with long-range positional and orientational order. In contrast, an isotropic liquid state (Figure 1.1 (c)) has molecules that move freely without any distinct order (Kumar & Kang, 2005). Liquid crystals (Figure 1.1 (b)) exist between these two states, forming an intermediate phase where molecules maintain partial order, either in their orientation or position (Singh and Dunmur, 2002).

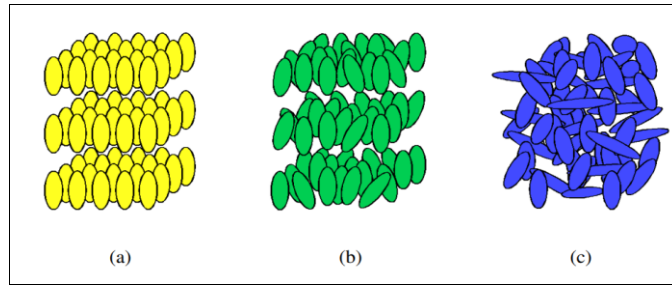


Figure 1.1 Arrangement of molecules in: (a) crystalline solid phase, (b) liquid crystal phase and (c) isotropic liquid phase

The anisotropic behaviour of liquid crystals originates from their molecular structure, which displays two fundamental characteristics:

- (i) one molecular axis is significantly different from the other two,
  - (ii) different molecular regions exhibit varied solubility properties
- (Collings & Hird, 2017).

As a result, interactions between anisotropic molecules define the degree of order in liquid crystals. These materials also undergo multiple phase transitions, experiencing various mesophases when shifting from solid to liquid (Khoo, 2022).

Liquid crystals also exhibit distinctive optical properties including refractive index, elasticity, permittivity, and viscosity that are direction dependent (anisotropy). This makes them highly responsive to external stimuli, allowing their properties to be easily modified, which is crucial for technological applications (Singh and Dunmur, 2002). Due to their distinct molecular

arrangement, liquid crystals can be found in everyday applications, ranging from soap films to laptop screens (Collings & Hird, 1998).

Liquid crystal displays (LCD) are thin, planar electronic panels that utilize the light-modulating capabilities of liquid crystals (LCs) which is its materials that manipulate light without self-emission. These LC-based technologies now dominate modern visual interfaces, enabling applications ranging from high-resolution televisions to compact smartphone screens. These technologies are based on the observation that a liquid crystal material may reorient in reaction to applied electric fields, changing its optical properties as a result (Karuna and Laxmi, 2015).

## **1.2 History of Liquid Crystal**

The study of liquid crystals dates back to 1888 when Austrian botanist Friedrich Reinitzer (Figure 1.2 (a)) observed that cholesteryl benzoate exhibited two distinct melting points. Reinitzer observed that heating a solid sample of cholesteryl benzoate first produced a cloudy liquid state at 145.5 °C, followed by transformation into a transparent liquid at 178.5 °C, which is also referring to the clearing point (DiLisi, 2019). He confirmed these phase transitions were thermally reversible. Reinitzer then send the cholesteryl benzoate (Figure 1.3 (c)) samples and his detailed observations to Lehmann (Figure 1.2 (b)), initiating one of the earliest examples of international, multi-disciplinary collaboration.

Therefore, their joint efforts led to the discovery of liquid crystallinity (Hussain, Pina and Roque, 2009).

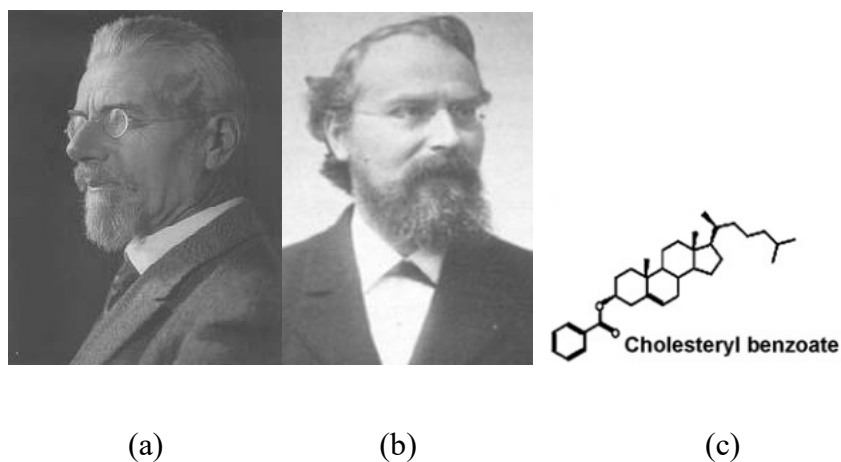


Figure 1.2: (a) Photo of Friedrich Reinitzer and (b) Otto Lehmann; (c) Structure of Cholesteryl benzoate (Hussain, Pina and Roque, 2009)

### 1.3 Categories of Liquid Crystal Phases

Liquid crystals also called as mesophase, represent an intermediate state of matter exhibiting properties between crystalline solids and isotropic liquids. Liquid crystalline mesophases display fluid-like flow properties while maintaining molecular orientation resembling crystalline solids (Chen, 2023). They change shape like a fluid but have the molecular alignment characteristics of a solid crystal. Liquid crystal materials generally have several common characteristics. Liquid crystals consist of anisotropic organic, rod-like molecule that exhibit parallel alignment. Molecules have minimal translational freedom and maintain positional order in the solid crystalline state (University of Houston, no date). The phrase "mesogenic state," which is used interchangeably with

"liquid crystal state," originates from the unique orientational order of the liquid crystal state, which lies between the conventional solid and liquid phases. The common types of liquid crystal used in electronic displays are nematic, cholesteric and smectic, which classified by molecular arrangement (PCMag, 1996). A schematic representation of molecules distribution in nematic, cholesteric, smectic phase is shown in Figure 1.3.

### **1.3.1 Nematic Phase**

Nematic liquid crystals (Figure 1.3 (a)) represents the basic form of compounds (Woliński, Ertman and Rutkowska, 2015). In this phase, rod-shaped molecules are aligned in the same direction along an average orientation called the director ( $n$ ) but are randomly positioned, lacking positional order (Bruce, 2007). This phase has low viscosity compared to other mesophases, allowing greater molecular mobility. The degree of molecular alignment influences the characteristics and behaviour of the nematic phase (Dierking, 2003).

### **1.3.2 Cholesteric Phase**

The cholesteric phase shown in Figure 1.3 (b), also known as the chiral nematic phase, is composed of nematic-like molecules containing a chiral center. This chiral property causes adjacent molecules to align at a slight angle to one another, forming a helical structure (Bruce, 2007). The director rotates gradually

from layer to layer, creating a structure similar to a stack of two-dimensional nematic layers (Shoop, Sayles and Litynski, 2002).

The helical arrangement results from weak intermolecular forces that cause molecules to shift slightly in orientation relative to the previous layer. The cholesteric phase exhibits unique optical properties, including selective light reflection, which makes it useful in liquid crystal displays (LCDs).

### 1.3.3 Smectic Phase

Smectic phases (Figure 1.3 (c)) possess both positional and orientational order, resulting in a more structured arrangement compared to the nematic phase (Soni *et al.*, 2013). In smectic phases, molecules are aligned in layers, restricting their motion within these planes. The two most common smectic phases are as shown in Figure 1.4:

- Smectic A (SmA): The director ( $n$ ) is oriented perpendicular to the layers, with molecules randomly distributed within each layer.
- Smectic C (SmC): The molecules tilt at an angle other than  $90^\circ$  relative to the layers. This modification from SmA creates a constant tilt angle within the layer plane. A variation of SmC, called *Smectic C (SmC)\**, exists when the molecules in each layer are arranged in a chiral (non-superimposable) form, leading to a continuously varying molecular direction from layer to layer (Dierking, 2003).

When observed under a polarized optical microscope (POM), SmA exhibits a fan-like texture, for SmC and SmC\* show a broken-fan pattern with colour variations as shown in Figure 1.4 (Dierking, 2003).

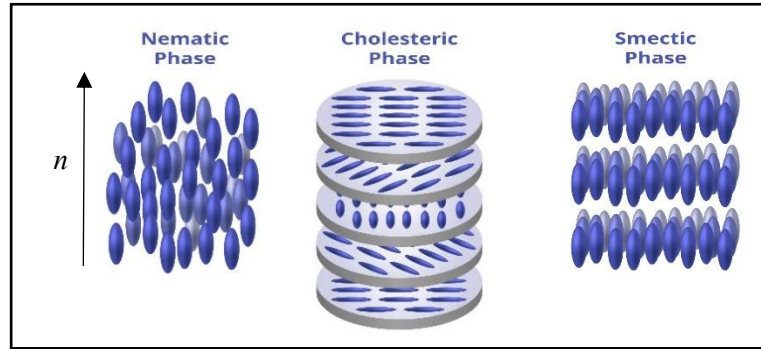


Figure 1.3: Schematic representation of molecules distribution in (a) Nematic Phase; (b) Cholesteric Phase; (c) Smectic Phase (Smartglass World, 2023)

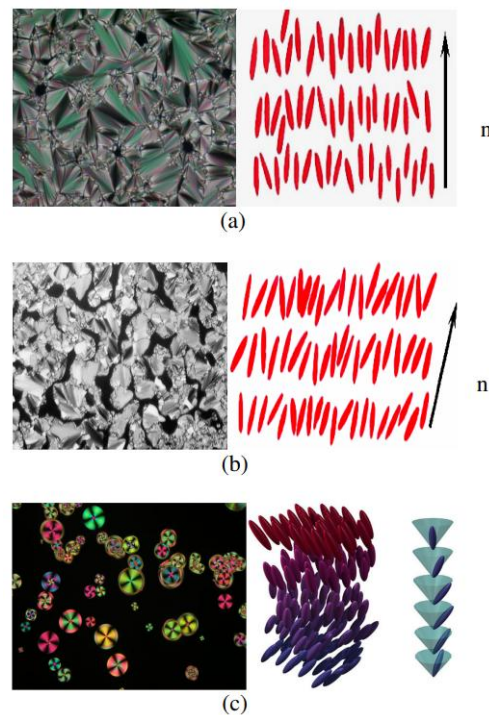


Figure 1.4: Texture and molecular arrangement (a) Smectic A; (b) Smectic C; and (c) Smectic C\* (Dierking, 2003)

## 1.4 Molecular Pattern and Chemical Framework of Liquid Crystal

According to An *et al.* (2016), they described that the fundamental structure of liquid crystal molecules as comprising two key components: (i) a rigid central core (mesogen) and (ii) flexible terminal chains (spacers). As illustrated in Figure 1.5, typical rod-like liquid crystalline molecules feature multiple aromatic rings interconnected through a central linkage group.

Due to the intense intermolecular attraction, the molecules in liquid crystals prefer to arrange parallel to one another ( $\pi$ - $\pi$  interactions) (An *et al.*, 2016). Liquid crystals typically feature a molecular structure that having: a) terminal flexible chains (R groups) at both ends, b) two or more aromatic rings c) central linkage groups connecting the rings. These linkage groups serve as connectors between aromatic cores (excluding direct bonds), it is important in determining mesomorphic behaviour. The directional orientation, and conformational flexibility of these linkage groups can influence the resulting liquid crystalline phases and their physical properties. By changing the structural parameters, characteristics of liquid crystal can be tailored for specific applications. The examples of linkage groups include Schiff base (C=N), ester, amide, azoxy (N=N), acetylene (C $\equiv$ C), tolane, and others. Meanwhile the example of side chain R and terminal group R' commonly consist of branched chains, moderately long linear hydrocarbon alkyl chains, or, in some cases, small polar substituents, particularly when a chiral center is needed. The selection of these terminal moieties plays a important role in determining the



liquid crystal phase formed. Additionally, the physical properties are significantly influenced by the choice of terminal units.

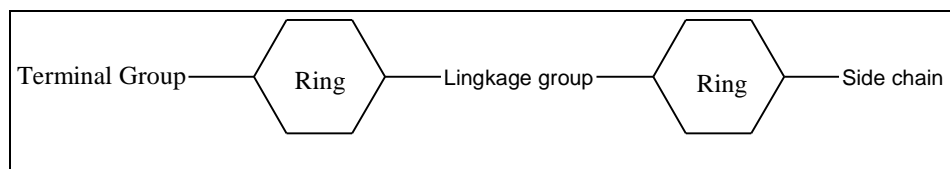


Figure 1.5: Typical rod-like shape of a liquid crystal molecule (Khoo, 2007)

All of the physical and optical properties of liquid crystals are determined by the properties of their constituent groups and their synthetic pathways. By adding the linking group into a mesogenic molecule extends its overall length and increases its polarizability anisotropy, thereby enhancing both the thermal stability and the temperature range of the mesophase. Liquid crystals with Schiff bases are typically very unstable. While ester, azo, and azoxy compounds exhibit greater stability, they are nevertheless highly vulnerable to changes in temperature, moisture, and ultraviolet radiation. Liquid crystalline compounds lacking central linkage groups exhibit exceptional thermal stability among the liquid crystals ever synthesized (Khoo, 2007).

## 1.5 Objectives

This project is aimed to achieve:

1. To synthesis a series of Schiff base liquid crystal with benzothiazole ring  
(*E*)-1-(4-(alkyloxy)phenyl)-*N*-(6-methoxybenzo[d]thiazol-2-yl)methanimine, **BRLCn** ( $n = 12, 14, 16$  and  $18$ )

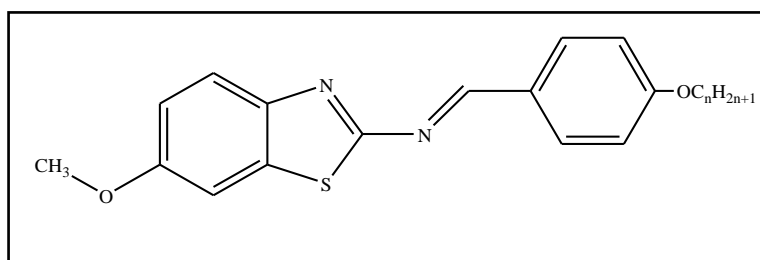


Figure 1.6: Molecular structure of series **BRLCn** compounds, where  $n = 12, 14, 16$ , and  $18$

2. To characterize the synthesized compounds using melting point apparatus, FTIR, NMR, and UV-Vis spectroscopic techniques.
3. To study the liquid crystal properties of the synthesized compounds using Differential Scanning Calorimeter (DSC)

## CHAPTER 2

### LITERATURE REVIEW

#### 2.1 Schiff Base Liquid Crystals

Schiff base liquid crystals have been extensively investigated for different terminal groups which will show nematic and smectic phases by many researchers. A Schiff base is a functional group characterized by a C=N bond, where the nitrogen atom is attached to an alkyl or aryl group (Raczuk *et al.*, 2022). In liquid crystal research, the Schiff base serves as a linking group, influencing and altering the physical properties of the compound.

Schiff bases contain a strongly polar imine (C=N) bond, which enhances intermolecular attraction forces and promotes molecular planarity (Hagar *et al.*, 2019). Imine synthesis proceeds through the condensation of an aromatic amine with a carbonyl compound, following a two-step mechanism: (1) nucleophilic addition to form a hemiaminal intermediate, and (2) subsequent dehydration to yield the imine product. The complete mechanism for the reaction pathway is illustrated in Figure 2.1. This structural characteristic of imine contributes to the formation of a highly stable mesophase, influenced by the properties of the Schiff base linkage (Jber, Shukur, and Najaf, 2017). In this project, Schiff bases were used as linkages connecting two benzene rings due to their unique

properties and varied temperature ranges when combined with different core structures, alkyl or acyl side chains, or lateral groups.

The synthesis of Schiff base liquid crystals requires starting materials containing an amine ( $-\text{NH}_2$ ) and a carbonyl ( $-\text{C}=\text{O}$ ) group. The process involves two key steps: condensation and dehydration. This reaction is reversible and occurs under heat, with either an acid catalyst or base catalysis facilitating the transformation (Hossain *et al.*, 2018). The synthesis of Schiff bases obtained from the reaction of carbonyl compounds with primary amines occurs through two key steps. First, the carbonyl group condenses with the primary amine to form a carbinolamine intermediate. In the second step, this intermediate undergoes dehydration, leading to the formation of the Schiff base (Subasi, 2022).

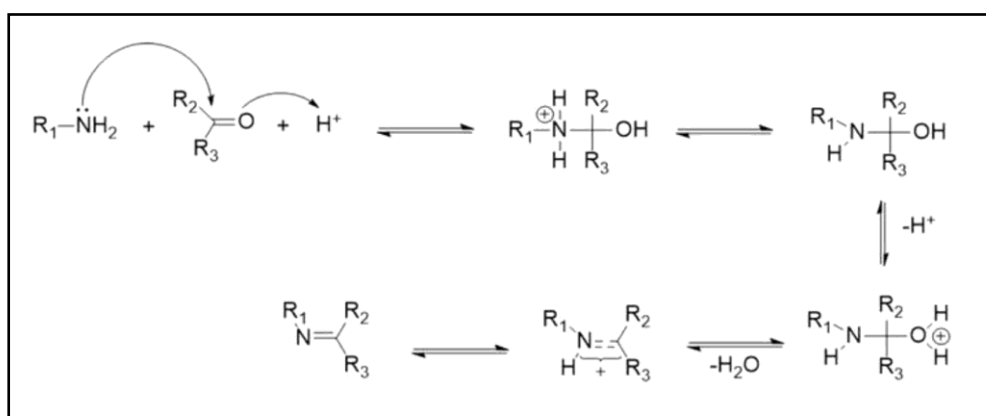


Figure 2.1: General mechanism of formation of Schiff Base (Subasi, 2022)

In imine formation, aldehydes are more reactive than ketones due to their lower steric hindrance. Additionally, in ketones, the substituent groups attached

to the carbonyl carbon donate electrons, decreasing its electrophilicity. This reduces the reactivity of the carbonyl group, slowing down the reaction. As a result, while aldehydes readily react with primary amines to form Schiff bases, the formation of Schiff bases from ketones is significantly more challenging. Therefore, 4-hydroxybenzaldehyde was used as the starting material in this project to synthesis Schiff base intermediate.

## **2.2 Relationship between Molecular Structure and Mesomorphic Behaviour**

In liquid crystal research, the structure of a compound is important in determining whether it exhibits mesomorphic properties. The specific arrangement of structural moieties influences the formation of particular morphological phases and defines the physical properties of the material. According to most scientific reports, mesophase formation can be seen in the structure that possess these three key molecular features: (1) a rigid central core, (2) elongated, flexible terminal chains, and (3) rod-like molecular that arranged in parallel alignment.

### 2.2.1 Effects of Alkyl Chain Length on Mesomorphic Properties

Research done by Ha *et al.* (2010a), which is the synthesis of 4-chlorobenzylidene-4'-alkanoyloxyaniline, **nClAB**, where  $n = 2-8, 10, 12, 14, 16, 18$  as shown in Figure 2.2. Out of the twelve compounds, the first two members (C2 and C3) did not possess mesomorphic properties. These molecules have short alkanoyloxy chains which make them excessively stiff, which raises their melting temperatures and hinders their ability to behave like liquid crystals. The compound with the shortest alkyl chain, n-butanoyloxy (C4), did not exhibit mesogenic properties. In contrast, n-hexanoyloxy (C6) displayed three exothermic peaks during the cooling cycle, indicating the presence of two mesophases. Meanwhile, the longer-chain homologs (C10 to C16) showed two endothermic transitions in their DSC thermograms, corresponding to the isotropic liquid to liquid crystal phase and liquid crystal phase to crystal phase changes. (Ha *et al.*, 2010a). An increase in terminal chain length makes the molecule more flexible and encourages a transition from non-mesogenic behaviour to monotropic and finally possess an enantiotropic property.

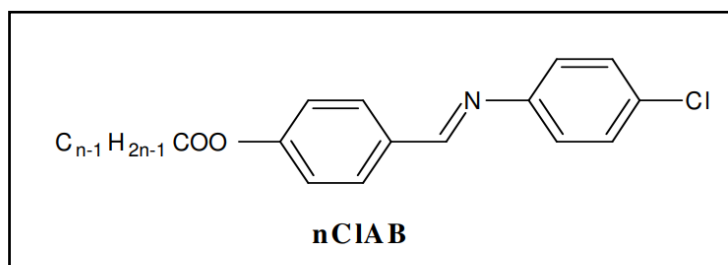


Figure 2.2: Structure of **nClAB** where  $n = 2-8, 10, 12, 14, 16, 18$

Another research conducted by Lee, Salleh, and Cheng (2021) synthesized three palm-based liquid crystals (**PB1–PB3**) using lauric acid, palmitic acid, and stearic acid to investigate the influence of length of alkyl chain on mesomorphic properties. The molecular structures of **PB1–PB3** contained three rings: two derived from a Schiff base intermediate—formed by the condensation of 4-hydroxybenzaldehyde and 4-bromoaniline—and one from a palm-based spacer. Due to the presence of an additional carboxyl group in 4-hydroxybenzoic acid, conventional Steglich esterification was ineffective, leading to the use of a palm-based spacer. This spacer was synthesized through esterification between alkanoyloxybenzoate acid ( $n = 10, 12, \text{ and } 16$ ) and 4-hydroxybenzoic acid.

All synthesized compounds exhibited Smectic A (SmA) mesophases, as confirmed by polarizing optical microscopy (POM). As shown in Figure 2.3, **PB1** displayed an SmA phase with a fan-shaped texture, while **PB2** and **PB3** exhibited SmA phases with a focal conic fan-shaped texture. Dark regions were observed within the fan-shaped structures, which is due to the combination of homeotropic molecular alignment and the SmA texture. The exclusive formation of the SmA phase in **PB1–PB3** was primarily due to the long alkyl chains, which enhanced molecular flexibility, broadened the mesogenic core, and promoted lamellar packing over parallel alignment. Additionally, the presence of ester linkages played a crucial role in SmA phase formation by inducing significant dipole changes within the compounds (Ha *et al.*, 2010b).

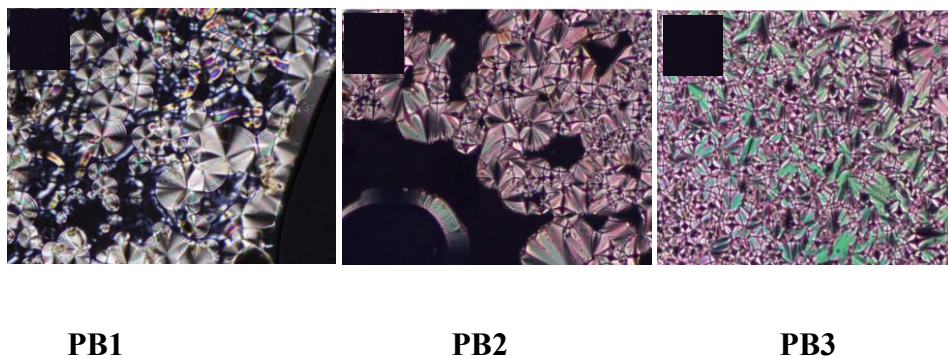


Figure 2.3: Polarizing optical microscope of **PB1** showing fan-shaped texture of SmA; **PB2** & **PB3** showing focal conic fan-shaped texture of SmA phase at 254, 201 and 203 °C respectively upon cooling (Lee, Salleh & Cheng, 2021).

Another research conducted by Ossowska-Chrusciel *et al.* (2004), he investigated the relationship between the alkyl chain length and the mesomorphic properties in a new series of chiral thiobenzoate liquid crystals. The structure of the synthesized compounds is shown in Figure 2.4. The findings show that chain length influences phase behaviour, thermal stability, and the presence of smectic and chiral nematic phases. The findings indicate that all homologous compounds exhibit a rich phase polymorphism, including a chiral nematic phase ( $N^*$ ), a ferroelectric  $SmC^*$  phase, and two highly ordered tilted smectic phases ( $SmI^*$  and  $SmG^*$ ). The presence of these phases suggests that molecular packing and intermolecular interactions are influenced by the alkyl chain length.

A key observation from the study is that compounds with shorter alkyl chains tend to exhibit higher melting points and lower thermal stability, while those with longer chains show increased flexibility, facilitating the formation of



stable mesophases. The clearing temperatures show a typical odd-even effect decreasing with elongation of alkyl chain. The SmC\* and N\* phases remain enantiotropic across all tested homologs, confirming the importance of alkyl chain length in stabilizing these mesophases. Table 2.1 shows the phase behaviour (S)-**MHOBSn** obtained during heating.

The study also highlights that when the alkyl chain length increases, the molecular interactions become favourable for the stabilization of the liquid crystalline phase. This trend suggests that optimizing chain length is important in designing materials with desired mesomorphic behaviour, particularly for applications in optoelectronics and display technologies.

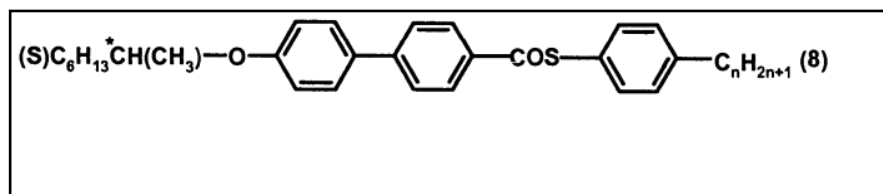


Figure 2.4: Structure of (S)- (+)-4-(1-methyloheptyloxy)biphenyl-(4'-alkylphenyl)- thiobenzoates, (S)-**MHOBSn** where n, number of carbons = 4 to 10 (Ossowska-Chrusciel et al., 2004)

Compounds	Phase transitions
(S)-MHOBS4	Cr 71.7 (3.95) SmG* 73.2 (0.12) SmC* 91.0 (0.16) N* 122 (0.12) I
(S)-MHOBS5	Cr 64.1 (5.63) SmG* 71.4 (0.07) SmI* 74.2 (0.36) SmC* 95.5 (0.24) N* 128.0 (0.19) I
(S)-MHOBS6	Cr 61.6 (3.36) SmG* 70.2 (0.02) SmI* 76.4 (0.31) SmC* 99.0 (0.36) N* 121.5 (0.10) I
(S)-MHOBS7	Cr 66.4 (2.77) SmG* 78.4 (0.24) SmC* 102.1 (0.17) N* 124.3 (0.19) I
(S)-MHOBS8	Cr 78.0 (6.27) SmG* 80.4 (0.41) SmC* 104.0 (0.30) N* 120.5 (0.31) I
(S)-MHOBS9	Cr 92.3 (4.56) SmC* 105.1 (0.11) N* 121.1(0.14) I
(S)-MHOBS10	Cr 92.4 (7.77) SmC* 106.1 (0.24) N* 118.6(0.31) I

Table 2.1: The phase behavior (S)-**MHOBSn** obtained during heating (Ossowska-Chrusciel et al., 2004)

## 2.2.2 Effects of Core group on Mesomorphic Properties

Fornasieri, Guittard, and G ribaldi (2003) investigated three series of  $\omega$ -unsaturated compounds which are **Phm**, **Bm** and **PhBm**, each featuring a linear perfluorinated alkyl chain and different number of core group. The molecular structure of the synthesized compounds are shown in Figure 2.5.

According to the conducted study, the transition temperature of a certain liquid crystal molecule can be significantly impacted by the addition of more aromatic rings to its core structures. The transition temperature also increased as the number of rings increased as shown in Figure 2.6 and Table 2.2.

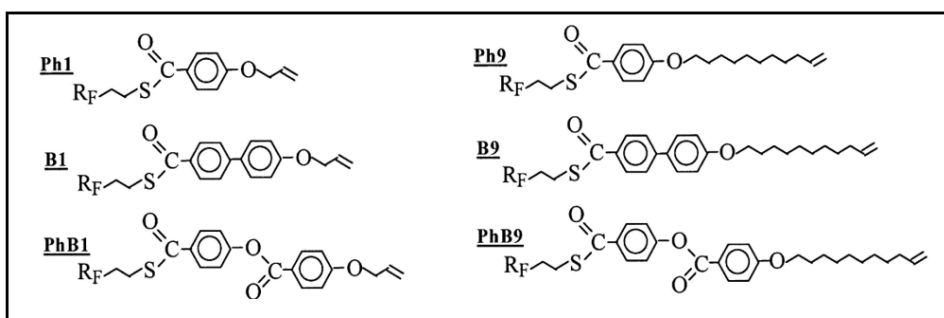


Figure 2.5: Structures of the three series of  $\omega$ -unsaturated compounds: **Phm**, **Bm** and **PhBm** ( $m = 1, 9$ ;  $R_F = C_6F_{13}$ )

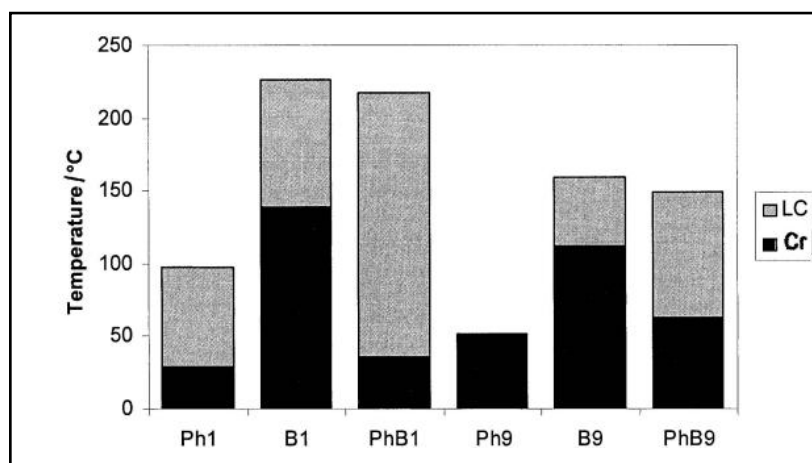


Figure 2.6: Comparison of the temperature ranges of the mesophases for the compounds **Phm**, **Bm**, **PhBm**

Transition Temperature, °C						
Compound	Cr	SmX		SmA		I
<b>Ph1</b>	•	29.3		•	97.8	•
<b>Ph9</b>	•	50.3		•	51.7	•
<b>B1</b>	•	138.5		•	226.6	•
<b>B9</b>	•	111.7	• 152.8	•	158.8	•
<b>PhB1</b>	•	36.3		•	217.6	•
<b>PhB9</b>	•	62.8	• 138.0	•	148.8	•

Table 2.2: Overall transition temperatures observed during heating for the of  $\omega$ -unsaturated derivative (Fornasieri, Guittard, and G ribaldi, 2003).

Within the allyloxy series (**Ph1**, **B1**, **PhB1**), the compounds with monophenyl substituent shows liquid crystal transitions at lower temperatures compared to its biphenyl-substituted compound. The study reports that these compounds display enantiotropic rather than monotropic mesophases. Further analysis of the DSC data (Figure 2.7) shows that **Ph1** stabilizes a mesophase across a thermal range of ~68  C (heating) and over 100  C (cooling), showing its broader mesomorphic stability during cooling. This showed that the compound stays in the mesophase at ambient temperature for at least twelve hours and that it needs substantial supercooling to crystallize.

The main reason that contributes to this physical behaviour is primarily due to the existence of the thioester group. Incorporation of the biphenyl core (**B1**) shifts the mesophase to higher temperatures, but with the temperature range unchanged; meanwhile, the phenyl benzoate unit broadens and stabilizes the mesophase range up to 181 °C. Both **B1** and **PhB1** exhibit high clearing temperatures, which are accompanied by structural changes, making the process irreversible. Polarized optical microscopy (POM) observations suggest gradual degradation at these elevated temperatures, a finding corroborated by thermogravimetric analysis.

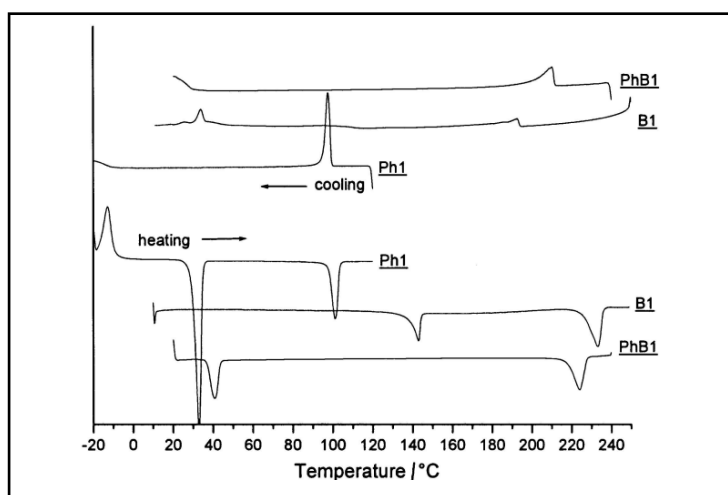


Figure 2.7: DSC curves for allyloxy compound **B1** (heating and cooling rate: 10 °C min<sup>-1</sup>) and **PhB1** first heating

### 2.2.3 Effects of Terminal Group on Mesomorphic Properties

Ha *et al.* (2010c) stated that differing *para*-position substituents ( $X = \text{H}$ ,  $\text{OCH}_3$ ,  $\text{CH}_3$ ,  $\text{C}_2\text{H}_5$ ,  $\text{F}$ ,  $\text{Cl}$ ,  $\text{Br}$ ) on the aniline fragment significantly influence mesomorphic behaviour. The molecular structures of these derivatives are presented in Figure 2.8.

Compound with less polar substituent,  $X = \text{CH}_3$ ,  $\text{C}_2\text{H}_5$ , it appeared as non-mesomorphic derivatives, meanwhile compound with methoxy and halogen substituents,  $X = \text{OCH}_3$ ,  $\text{Cl}$ ,  $\text{Br}$ ,  $\text{F}$  exhibited liquid crystal phase.

This phenomenon can be due to the methoxy group ( $\text{OCH}_3$ ) being in conjugation with the aromatic core, which effectively extends the length of the rigid molecular segment and consequently enhances its polarizability. While  $\text{CH}_3$  is shorter in chain length as compared to  $\text{OCH}_3$ . Thus, it does not possess mesomorphic structure. For the compound with **SB-ME** ( $-\text{CH}_3$ ) and **SB-ET** ( $-\text{C}_2\text{H}_5$ ), the compound **SB-ME** possess a higher clearing temperature as compared with compound **SB-ET**. This observation is because of the *ortho*-position hydroxyl group enhances mesophase stability more effectively in compounds with shorter terminal chains. Consequently, in shorter-chain derivatives, its molecular order was higher degree, which is favoured by the increased polarizability (Ha *et al.*, 2010c).

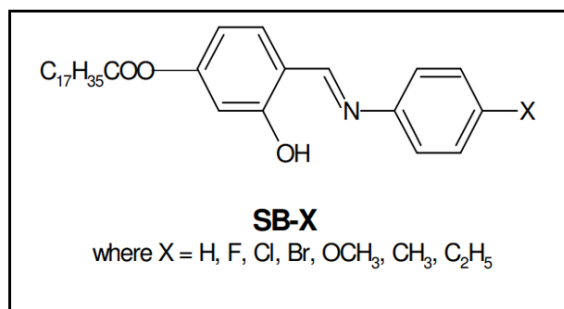


Figure 2.8: Structure of 3-hydroxy-4-[(4-X-substitutedphenyl)limino]methyl}phenyl octadecanoates (Ha *et al.*, 2010c)

The terminal group will influence the stability of mesophase, which affects the transition temperature from the liquid crystal phase to the isotropic liquid phase. Among the **SB-X** compounds (X = Cl, Br and F), showing halogen-substituted aniline fragments, **SB-F** (-F) exhibits a markedly lower clearing temperature than both **SB-CL** (-Cl) and **SB-BR** (-Br). This thermal behaviour can be due to fluorine atom's strong electronegativity, which appears to destabilize molecular packing despite the structural influence of the *ortho*-hydroxyl group. The thermal data further indicate that **SB-F** (-F) experiences minimal steric constraints due to its asymmetric core geometry, while the bulkier chlorine and bromine **SB-CL** (-Cl) and **SB-BR** (-Br) maintain higher clearing temperatures. The presence of chlorine as terminal group with long carbon at alkoxy chain caused an overall increased in polarizability (Sardon *et al.*, 2021).

## 2.2.4 Effects of Linkage Group on Mesomorphic Properties

The linking group in liquid crystals used to connect two aromatic units significantly influences the physical properties of liquid crystals, including structural and dielectric anisotropy, phase transition temperatures, and mesophase stability. To positively affect liquid crystal behaviour, the linking group must preserve the linearity of the core and be compatible with peripheral structure of molecule.

In the research done by Ong and Ha (2013), they change the direction of ester linkage on the existing system (Schiff base 4-chlorobenzylidene-4'-alkanoyloxyanilines) bases (Ha *et al.* 2010a), then study the influence of reversed ester linkage on mesomorphism of Schiff bases. Although the structure are similar, but the smectic nature of the series is quite different. Their structures are shown in Figure 2.9 and 2.10.

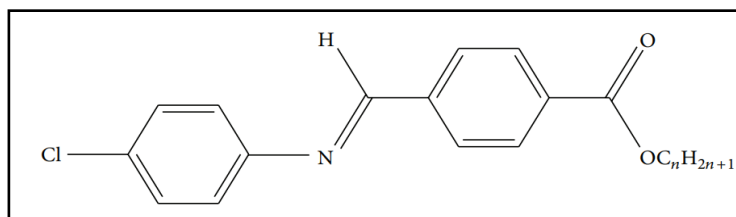


Figure 2.9: Structure of 4-chlorobenzylidene- 4'-alkanoyloxyaniline, **nCIAB** ( $n = 2-8, 10, 12, 14, 16, 18$ ) (Ong and Ha, 2013)

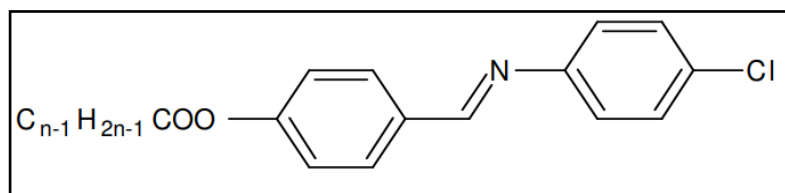


Figure 2.10: Structure of alkyl 4-[[4-chlorophenyl]imino]methyl}benzoates, **nClCBA** ( $n = 2-16$ ) (Ha *et al.*, 2010a)

The mesomorphic properties of the two aromatic ring compounds, 4-chlorobenzylidene-4'-alkanoyloxyanilines (**nCIAB**) and alkyl 4-[[4-chlorophenyl]imino]methyl}benzoates (**nClCBA**), are highly influenced by the orientation of the ester linkage.

**nCIAB** series having molecular arrangement of alkyl COO-phenyl exhibited smectic A and B phases as shown in Figure 2.11. However, **nClCBA** with the reversed ester linkage exhibit non-mesomorphic compounds as shown in Figure 2.12. The orientation of the ester linking group determines the direction of the carbonyl group. Variations in the direction of the carboxyl groups between the phenyl and alkyl segments lead to significant changes in the molecular dipole moment. This, in turn, reduces both the polarizability anisotropy and the geometric anisotropy of the molecule.

Furthermore, the **nCIAB** series exhibited higher melting points compared to the **nClCBA** series with the same number of carbon atoms ( $n$ ) in the alkyl chain. This suggests that the orientation of the ester linkage can affect the thermal



stability of a compound. In **nCIAB**, the interaction between the ester and phenyl groups appears to result in molecules with increased polarity, which likely enhances lateral interactions of a polar nature and may consequently lead to a higher clearing temperature.

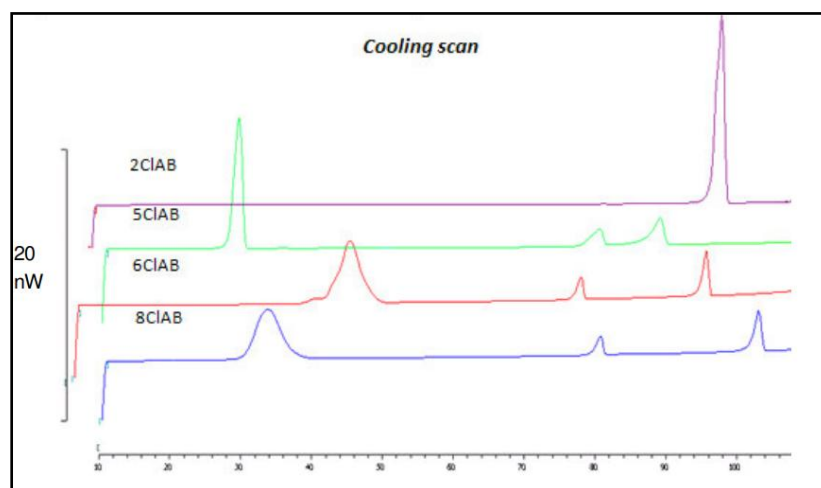


Figure 2.11: DSC thermograms of **nCIAB** ( $n = 2, 5, 6, 8$ ) during cooling cycles (Ong and Ha, 2013)

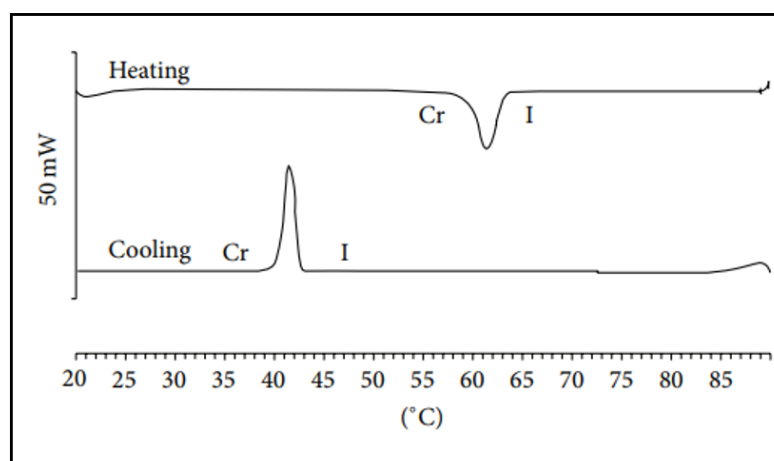


Figure 2.12: DSC thermogram of undecyl 4-[(4-chlorophenyl)imino]methyl}benzoate, **nCICBA** ( $n = 11$ ) during heating and cooling cycles (Ha *et al.*, 2010a)

Another research done by Pfletscher, Mezger and Giese (2018), show the impact of the linking group in hydrogen-bonded liquid crystals. The structure of the liquid crystal and linking group used are shown in Figure 2.13.

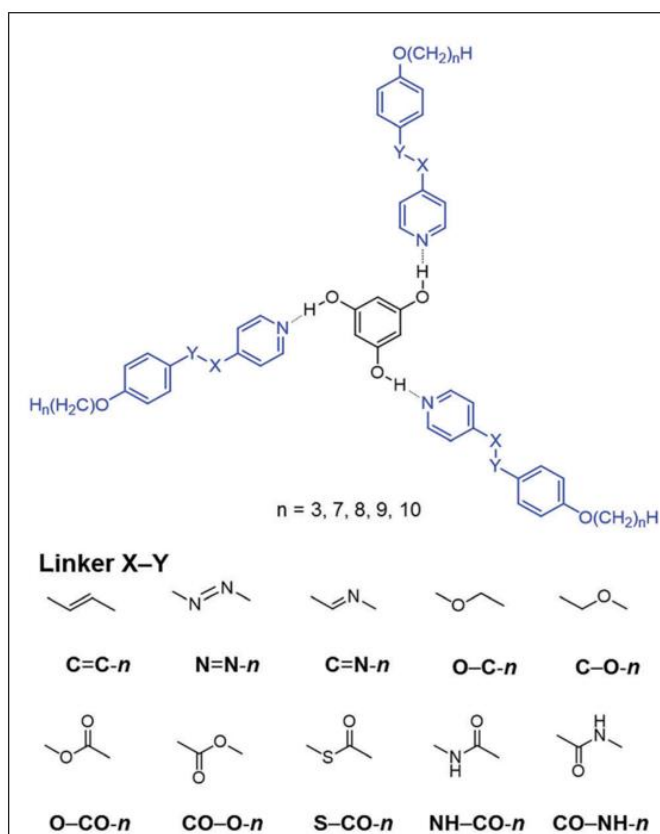


Figure 2.13: Schematic illustration of prepared hydrogen-bonded starshaped assemblies for the systematic investigation of the impact of the linking group on the liquid crystalline behaviour (Pfletscher, Mezger and Giese, 2018)

The rigidity imparted by the type of linking group is particularly important for stabilizing the mesophase. Pfletscher, Mezger, and Giese (2018) conducted a comparative analysis of different linking groups, evaluating their effects on molecular rigidity. While both secondary amide and imine bridges were found to maintain side-chain rigidity, these structural features unexpectedly

suppressed the liquid crystalline properties in the studied hydrogen-bonded assemblies (HBAs). In the case of amide-linked systems (NH–CO–n, CO–NH–n), the absence of a mesophase (as shown in Figure 2.14) may be due to the formation of strong intermolecular hydrogen bonds with neighbouring molecules. This is further supported by the elevated phase transition temperatures observed for these hydrogen-bonded assemblies.

By comparing S–CO–n and O–CO–n linking group, both HBAs exhibit the liquid crystallinity. However, their mesomorphic behaviour differs due to structural variations and distinct rigidity characteristics between the thioester (S–CO–n) and ester (O–CO–n) linking units. The presence of the larger sulphur atom in S–CO–n based disrupts the conjugation between the benzene and pyridyl units, resulting in increased molecular flexibility and alterations in both bond angles and lengths (specifically the C–S–C bond angle and C–S bond length) between the aromatic rings. As a result, the nematic phase stability in S–CO–n-based assemblies decrease relative to their O–CO–n counterparts, especially with elongation of the peripheral aliphatic chains (Pfletscher, Mezger and Giese, 2018).

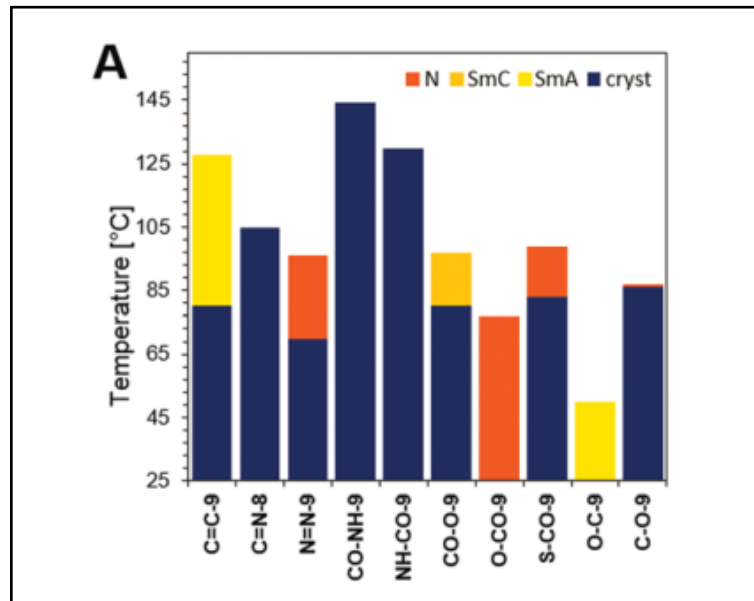


Figure 2.14: Overview of the phase transition (A) of nonyl-based HBA representatives obtained via POM upon cooling. A comparison of the observing findings with different linkage parts indicates the structural differences among each other (Pfletscher, Mezger and Giese, 2018)

## CHAPTER 3

### METHODOLOGY

#### 3.1 Chemicals

The list of chemicals used for synthesis were recorded in Table 3.1 as well as the origin of chemicals. The chemicals used directly without further purification actions.

Table 3.1: Chemical reagents used and their origin

Chemical used	Origin
2-Amino-6-methoxybenzothiazole 4-Hydroxybenzaldehyde	Acros Organics, Belgium
Absolute ethanol ( $\geq 99.5\%$ )	VWR International, United State
Glacial acetic acid ( $\geq 99.8\%$ )	RCI Labscan, Thailand
Potassium carbonate (analytical grade)	R&M Chemical, Malaysia
N,N-Dimethylformamide, DMF ( $\geq 99.8\%$ )	Fisher Scientific, United Kingdom
Acetone (analytical grade, $\geq 99.5\%$ ) n-Hexane (analytical grade, $\geq 95\%$ ) 1-Bromododecane ( $\geq 98\%$ ) 1-Bromotetradecane ( $\geq 97\%$ ) 1-Bromohexadecane ( $\geq 97\%$ ) 1-Bromooctadecane ( $\geq 97\%$ )	Merck, Germany

### 3.2 Instrumentations

During this research project, various analytical instruments were used to characterize the synthesized compounds. The instrument models and their respective functions are listed in Table 3.2.

Table 3.2: Instruments used and their corresponding applications

Instrument models	Application
Perkin Elmer 2000-FTIR Spectrometer (Spectrum RX1)	To identify the useful structural information for the general characterization of functional group frequencies.
Perkin Elmer Spectrum TWO ATR-FTIR Spectrophotometer	To identify the useful structural information for the general characterization of functional group frequencies.
Mettler Toledo DSC823 Differential Scanning Calorimeter	To determine the mesophase existences of compounds and the enthalpy changes and
NMR Spectrometer JEOL JNM-ECX400	To determine molecular structure in term of $^1\text{H}$ , $^{13}\text{C}$ , COSY, HMBC, and HMQC
Thermo Scientific GENESYS 50 UV-Vis	To determine the molar absorptivity and photophysical properties of compounds.
Stuart SMP10 Melting Point Apparatus	To determine compounds' melting points and melting range.

### 3.3 Experimental Synthesis

The overall synthesis pathway for the formation of **BRLCn** is shown in the Figure 3.1

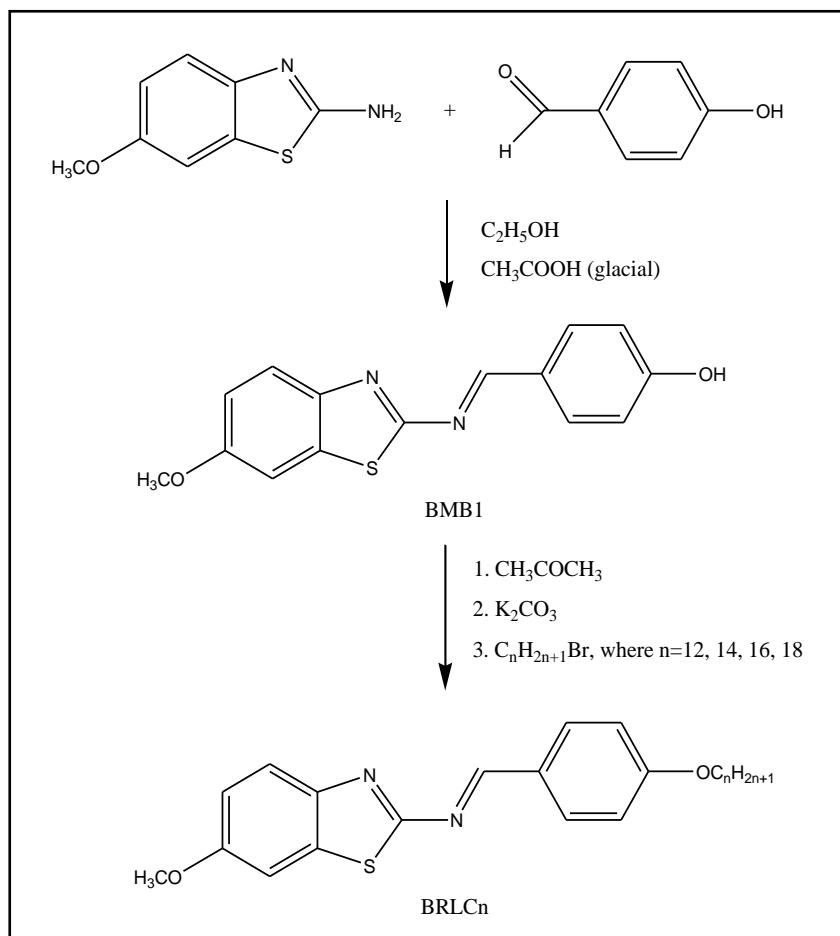


Figure 3.1: Overall synthesis route for **BRLCn** formations

### 3.3.1 Preparation of (*E*)-4-(((6-methoxybenzo[d]thiazol-2-yl)imino)methyl)phenol, **BMB1**

An equimolar of 2-amino-6-methoxy benzothiazole (3.604 g, 20 mmol) and 4-hydroxybenzaldehyde (2.442 g, 20 mmol) were weighed into two separated beakers. Ethanol (20 mL each) was added into each of these beakers. Next, both dissolved materials were mixed into a 100 mL round-bottomed flask, three drops of glacial acetic acid were added and refluxed at 80 °C for five hours. Yellow precipitate in crystalline form was observed, the crystals was filtered using vacuum filtration and recrystallized at 80 °C with 20 mL hot ethanol. After all the crude product dissolved, it was cooling down slowly to room temperature. Upon cooling, product formed. Product obtained was air dried in fume hood. Percentage yield: 63.55%, actual mass: 6.2160 g (12.72 mmol), melting point: 225-227 °C.

### 3.3.2 Preparation of (*E*)-1-(4-(alkyloxy)phenyl)-*N*-(6-methoxybenzo[d]thiazol-2-yl)methanimine, **BRLC<sub>n</sub>** (n = 12, 14, 16 and 18)

#### 3.3.2.1 Preparation of (*E*)-1-(4-(dodecyloxy)phenyl)-*N*-(6-methoxybenzo[d]thiazol-2-yl)methanimine, **BRLC12**

**BMB1** (1.4203 g, 5 mmol) was dissolved in 10 mL of DMF. The dissolved form of **BMB1** solution was poured into a round bottom flask. Then,



35 mL of acetone was added into the round bottom flask, followed by potassium carbonate (0.69 g, 5 mmol). Next, 1-bromododecane (1.25 mL, 5 mmol) dissolved in 5 mL of acetone was poured into the round bottom flask. The mixture was refluxed at 60 °C for five hours. After five hours, cold distilled water was added into the resulting yellowish solution in order to dissolve the potassium carbonate. After the addition of cold distilled water, yellow precipitate in crystalline form was observed. The crystal was filtered using vacuum filtration and then, it was recrystallized at 80 °C with 10 mL hot ethanol. Product obtained was air dried in fume hood. Percentage yield: 55.15%, actual mass: 1.2481g (2.76 mmol) melting point: 75-78 °C.

#### **3.3.2.2 Preparation of (*E*)-1-(4-(tetradecyloxy)phenyl)-*N*-(6-methoxybenzo[d]thiazol-2-yl)methanimine, BRLC14**

Similar procedure as the preparation for **BRLC12** was applied for the preparation of **BRLC14** by replacing 1-bromododecane with 1-bromotetradecane (1.40 mL, 5 mmol). Percentage yield: 52.70%, actual mass: 1.2662 g (2.64 mmol)melting point: 82-84 °C.

### 3.3.2.3 Preparation of (*E*)-1-(4-(hexadecyloxy)phenyl)-*N*-(6-methoxybenzo[d]thiazol-2-yl)methanimine, BRLC16

Similar procedure as the preparation for **BRLC12** was applied for the preparation of **BRLC16** by replacing 1-bromododecane with 1-hexadecane (1.50 mL, 5 mmol). Percentage yield: 46.30 %, actual mass: 1.1781 g (2.32 mmol), melting point: 85-87 °C.

### 3.3.2.4 Preparation of (*E*)-1-(4-(octadecyloxy)phenyl)-*N*-(6-methoxybenzo[d]thiazol-2-yl)methanimine, BRLC18

Similar procedure as the preparation for **BRLC12** was applied for the preparation of **BRLC18** by replacing 1-bromododecane with 1-octadecane (1.65 mL, 5 mmol). Percentage yield: 71.40%, actual mass: 1.9173 g (3.570 mmol), melting point: 93-95 °C.

## 3.4 Characterizations

### 3.4.1 Thin Layer Chromatography (TLC) Analysis

The starting materials (2A6MB and 4HB) and synthesized compounds **BMB1**, and **BRLCn** were analysed using the silica-gel TLC plates (aluminium-

backed). Visualization was performed under short-wave UV light, with a 1:1 chloroform/ethyl acetate mobile phase.

### 3.4.2 Fourier Transform (FTIR)

The synthesized compounds were analysed using a Perkin Elmer 2000 FTIR (Spectrum RX1) spectrometer and Perkin Elmer Spectrum TWO ATR Spectrophotometer, within a frequency range of 4000–400  $\text{cm}^{-1}$ . The samples were prepared in KBr pellet form for Perkin Elmer 2000 FTIR (Spectrum RX1) spectrometer. Besides, **BRLCn** samples were placed on the diamond cell and subjected to Attenuated Total Reflectance Fourier-Transform infrared (ATR-FTIR) analysis using Perkin Elmer Spectrum TWO ATR-FTIR Spectrophotometer. Through the infrared spectral characterizations, the functional groups presence in compounds can be identified.

### 3.4.3 Nuclear Magnetic Resonance (NMR)

To confirm the molecular structure of the final products,  $^1\text{H}$ ,  $^{13}\text{C}$ , COSY, HMQC, HMBC NMR analysis were carried out on the final product using NMR JEOL JNM-ECX400. The sample prepared using the deuterated chloroform solution ( $\text{CDCl}_3$ ) at room temperature (25  $^\circ\text{C}$ ), and the tetramethylsilane (TMS) served as the internal standard. The  $^1\text{H}$  NMR analysis was performed at 400 MHz frequency while the  $^{13}\text{C}$  NMR was analyzed at 100 MHz frequency using same unit of NMR JEOL JNM-ECX400.

#### 3.4.4 Differential Scanning Calorimetry (DSC)

A series of **BRLC<sub>n</sub>**, where  $n = 12, 14, 16,$  and  $18$  was analysed using Mettler Toledo DSC823 Differential Scanning Calorimeter. Samples (5-10 mg) were sealed in 45  $\mu\text{L}$  aluminium crucibles, with a pinhole to release pressure, then analysed for enthalpy changes.

Next, the sample was positioned in the DSC instrument's sample compartment. The heating and cooling rates, along with the temperature settings, were adjusted accordingly for different samples. The thermal analysis was conducted under a nitrogen flow of 1 mL/min during both heating and cooling cycles. The heating rate of the DSC instrument was set to 5  $^{\circ}\text{C}/\text{min}$ , in order to obtain a better resolution thermogram. Slower heating gives sharper, more defined peaks, making it easier to distinguish closely spaced transitions. Once the scanning process was done, the crucible that containing the sample was removed.

#### 3.4.5 Photophysical Properties Analysis

A homologous series of **BRLC<sub>n</sub>**, where  $n = 12, 14, 16,$  and  $18$  was analysed using Thermo Scientific GENESYS 50 UV-Vis Spectrophotometer. The UV-Vis analysis is used to determine the molar absorptivity and photophysical properties of compounds.

In the sample preparation, the concentration of each product was carefully controlled to obtain a consistence result. 2.5 mg of solid sample was weighed and dissolved in chloroform in a 25 ml volumetric flask and labelled as stock solution. The stock solution was used to create a set of standard solutions with different concentration to calculate the molar absorptivity. The molar absorptivity of each compound was determined with a series of standard solution of each compound. The scanning wavelength for the UV-Vis analysis is 250 – 800 nm.

#### **3.4.6 Melting Point Analysis**

The homologous series of **BRLCn**'s melting points and melting point ranges were recorded using Stuart SMP10. Initially, a tiny amount of the **BRLCn** series was put into a small capillary tube. The plateau temperature of 25 °C was selected and locked in. The sample was then monitored until the melt occurred in the capillary tube. The melting point was recorded from the appearance of the first drop of sample melt until the sample was completely melted.

## CHAPTER 4

### RESULTS AND DISCUSSION

#### 4.1 Mechanism involved

##### 4.1.1 Synthesis of (*E*)-4-(((6-methoxybenzo[d]thiazol-2-yl)imino)methyl)phenol, **BMB1**

The starting materials, 2-amino-6-methoxybenzothiazole and 4-hydroxybenzaldehyde, undergo condensation with concentrated acetic acid as catalyst to form a Schiff base intermediate, **BMB1**. In this reaction, the nitrogen atom of 2-amino-6-methoxybenzothiazole, which possesses a lone pair of electrons, acted as a nucleophile and attacked the electrophilic carbonyl carbon of 4-hydroxybenzaldehyde, leading to the formation of a carbinolamine intermediate. Subsequently, acid-catalysed dehydration took place in the presence of concentrated acetic acid, eliminating a water molecule and resulting in the formation of **BMB1**. Mechanism for Schiff base condensation is shown in Figure 4.1 (Sani, Na'ibi and Dailami, 2018).

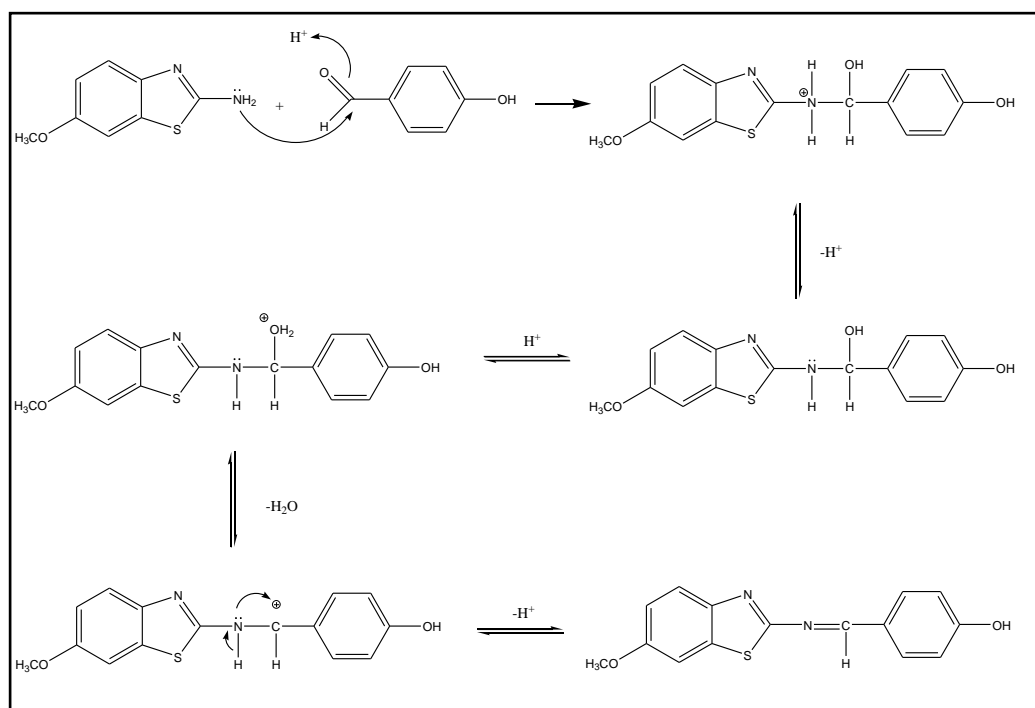


Figure 4.1: Mechanism for Schiff base condensation between 2A6MB and 4HB (Sani, Na'ibi and Dailami, 2018)

#### 4.1.2 Synthesis of (*E*)-1-(4-(alkyloxy)phenyl)-*N*-(6-methoxybenzo[d]thiazol-2-yl)methanimine, BRLC<sub>n</sub> (n = 12, 14, 16 and 18)

In the synthesis of **BRLC<sub>n</sub>**, the reaction involve is the Williamson etherification between **BMB1** and alkyl bromide. The Williamson Ether Synthesis is an S<sub>N</sub>2 reaction in which an alkoxide ion act as a nucleophile, attacking an alkyl halide and displacing its halide ion to form an ether. This reaction proceeds with inversion of configuration at any chiral carbon involved and may be affected by competing elimination reactions under certain conditions (Ouellette and Rawn, 2015).

In the first step, potassium carbonate acts as a weak base and deprotonates the hydroxyl group of the phenol. This results in the formation of a phenoxide anion, act as the nucleophile. Besides, the deprotonation produces potassium bicarbonate ( $\text{KHCO}_3$ ) as a byproduct. In the second step, the nucleophile attacks the primary alkyl bromide ( $\text{R-Br}$ ), where R represents long alkyl chains such as  $\text{C}_{12}\text{H}_{25}$ ,  $\text{C}_{14}\text{H}_{29}$ ,  $\text{C}_{16}\text{H}_{33}$ , or  $\text{C}_{18}\text{H}_{37}$ . This response takes place in a single step, which is both cleavage and bond formation, which also known as an  $\text{S}_{\text{N}}2$  reaction. The final product is an aryl ether, with the oxygen connecting the aromatic ring to the long-chain alkyl group. A potassium bromide ( $\text{KBr}$ ) salt is also formed as a byproduct. In Figure 4.2, the detailed mechanism for Williamson etherification is shown.

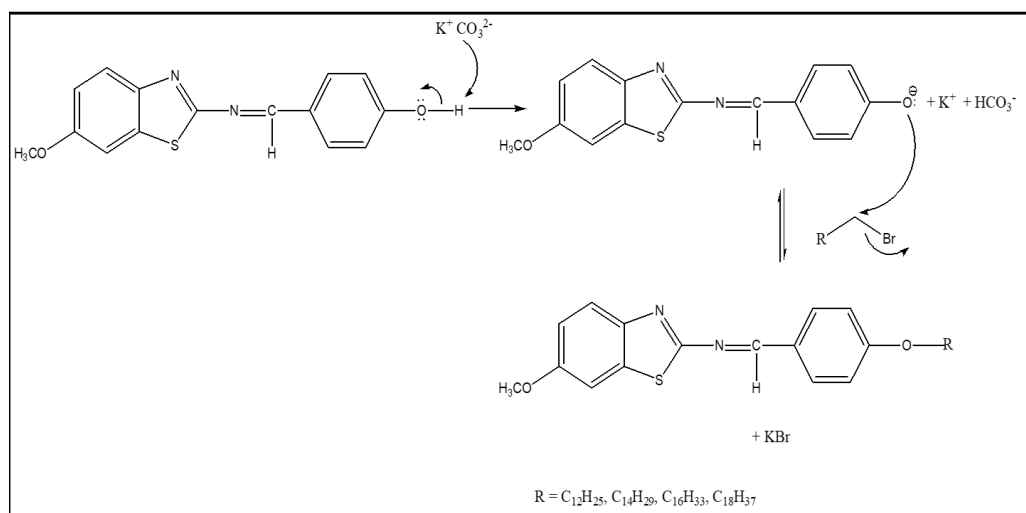


Figure 4.2: Williamson etherification for the formation of **BRLCn** (Ashenhurst, 2025)



## 4.2 Thin Layer Chromatography (TLC) Analysis

Thin layer chromatography (TLC) analysis was done to determine the purity of the compound synthesized. An aluminium plate coated with silica gel was used as the stationary phase, while mobile phase is the solvent system with mixture of 1:1 ethyl acetate and chloroform. Figure 4.3 displays the TLC plates of **BRLC16**, use as a representative example for the compounds.

In plate I, the pale-yellow crude final product showed three spots at  $R_f = 0.49$  (10%),  $0.74$  (10%), and  $0.90$  (80%), with the most intense spot at  $R_f = 0.90$  indicating the desired product, when observed under shortwave UV light. After recrystallization at  $80\text{ }^{\circ}\text{C}$  in 10 mL of ethanol, produced a homogeneous TLC profile (plate II; single spot, with the  $R_f$  value of  $0.90$ ). The one spot had confirmed that the final product reaching its purity. The two extra spots observed on TLC Plate I, represent the two unreacted starting materials in crude **BRLC16** sample. The comparative  $R_f$  values for series of **BRLC16** compound are shown in Table 4.1.

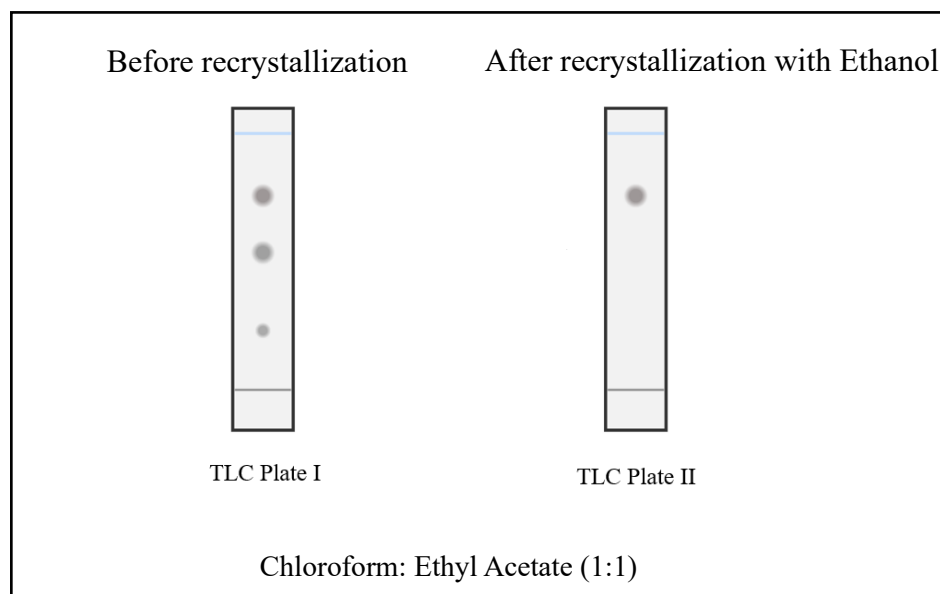


Figure 4.3: TLC Plate for **BRLC16**

Table 4.1:  $R_f$  values for the series of **BRLCn** compounds

Compound	$R_f$ value
<b>BRLC12</b>	0.87
<b>BRLC14</b>	0.87
<b>BRLC16</b>	0.90
<b>BRLC18</b>	0.85

### 4.3 Fourier Transform (FTIR)

#### 4.3.1 Fourier Transform Infrared Spectroscopy (FTIR) Analysis of 2A6MB, 4HB and BMB1

The FTIR spectra for compounds **BMB1**, 2A6MB, 4HB in comparison, and compound **BRLC16** are shown in Figures 4.4 and 4.5 respectively. The important FTIR spectral data are compared and summarized in Table 4.2 and Table 4.3.

In 2A6MB, it shows two sharp absorption peaks at 3399 and 3369  $\text{cm}^{-1}$  that represented primary amines NH stretching group. The formation of the first NH stretching peak at the higher frequency is because of the asymmetric stretch and the second NH stretching is caused by symmetric stretch. This splitting occurs because the two N–H bonds vibrate out-of-phase (asymmetric) and in-phase (symmetric). Distinct C-H stretching vibrations were observed, with the aromatic ( $\text{sp}^2$ ) C-H stretching appearing at 3111  $\text{cm}^{-1}$  and aliphatic ( $\text{sp}^3$ ) C-H stretches at 2838  $\text{cm}^{-1}$  and 2744  $\text{cm}^{-1}$ . The aromatic ring was confirmed by C=C stretching vibrations at 1544  $\text{cm}^{-1}$  and 1434  $\text{cm}^{-1}$ . A strong absorption peak at 1636  $\text{cm}^{-1}$  was assigned to the C=N stretching vibration, characteristic of the imine functional group. Additional diagnostic peaks included the C-N stretching at 1337  $\text{cm}^{-1}$  and the C-O stretching at 1259  $\text{cm}^{-1}$ , completing the functional group identification.

In 4HB, the OH stretching appeared as a broad peak at  $3175\text{ cm}^{-1}$ , confirming the presence of hydroxyl group. The infrared spectrum also shows the characteristic C–H stretching vibrations, with a band at  $3009\text{ cm}^{-1}$  corresponding to  $\text{sp}^2$  C–H stretching, while the peaks at  $2878\text{ cm}^{-1}$  and  $2696\text{ cm}^{-1}$  were attributed to aliphatic  $\text{sp}^3$  C–H stretching, consistent with the aldehyde functional group. Other than that, a prominent C=O stretching vibration appeared at  $1673\text{ cm}^{-1}$ , due to  $\pi$ -conjugation between the carbonyl group and the adjacent phenyl ring. Additionally, the spectrum shows strong and medium intensity absorptions at  $1590\text{ cm}^{-1}$  and  $1450\text{ cm}^{-1}$ , respectively, characteristic of aromatic C=C stretching vibrations in the phenyl ring.

The formation of Schiff base intermediate, **BMb1** compound is formed through the Schiff base condensation between 2A6MB and 4HB. The IR spectrum of **BMb1** exhibits characteristic absorption bands corresponding to O–H and C=N functional groups, confirming their presence in the molecular structure. These peaks show the formation of a Schiff base, which involves the reaction between the N–H group of 2A6MB and the CHO, aldehyde functional group of 4HB, resulting in a new C=N linkage. As a consequence of Schiff base formation, the N–H stretching due to 2A6MB disappears in the spectrum, indicating that imination has occurred. In **BMb1**, the O–H stretching appears as a weak band at  $3431\text{ cm}^{-1}$ , a strong and sharp absorption peak at  $1602\text{ cm}^{-1}$  was clearly attributed to the C=N stretching vibration of the Schiff base (azomethine) linkage. The aromatic C=C stretching peak was overlapped with the C=N stretching peak at that wavenumber. Other than that, there are also C=N stretching for benzothiazole observed at  $1577\text{ cm}^{-1}$  (Seou *et al.*, 2014). Besides these two distinct peaks, a peak was observed at  $2810\text{ cm}^{-1}$  which represents the

sp<sup>3</sup> C-H stretching. A sharp absorption band appeared at 1250 cm<sup>-1</sup> is attributed to C-O stretching bond. The FTIR results of **BMB1** was compared with the research done by Seou *et al.* (2014).

#### 4.3.2 Fourier Transform Infrared spectroscopy (FTIR) Analysis of **BRLCn**

The data of FTIR spectrum of **BRLCn** series were recorded in Table 4.3. The FTIR spectrum of Schiff base ether, **BRLC16** was shown in Figure 4.5. It is formed by the Williamson etherification of **BMB1** and 1-bromohexadecane. The successful synthesis of **BRLC16** was confirmed by characteristic C-H stretching vibrations in the IR spectrum, with the aliphatic (sp<sup>3</sup>) C-H stretch observed at 2918 and 2849 cm<sup>-1</sup>. The Schiff base C=N linkage exhibited a characteristic IR absorption band at 1603 cm<sup>-1</sup>, while another peak at 1253 cm<sup>-1</sup> corresponded to the C-O stretching vibration of the aromatic ether (Ar-O-R), confirming the successful Williamson etherification. In Figure 4.5, a broad absorption band is observed around 3430 cm<sup>-1</sup>, which could be due to the presence of an -OH functional group. However, this observation is possible due to the absorption of moisture during the preparation of the KBr pellet. The presence of hydroxy functional group is further verified using ATR technique and the result are presented in the next section 4.3.3.

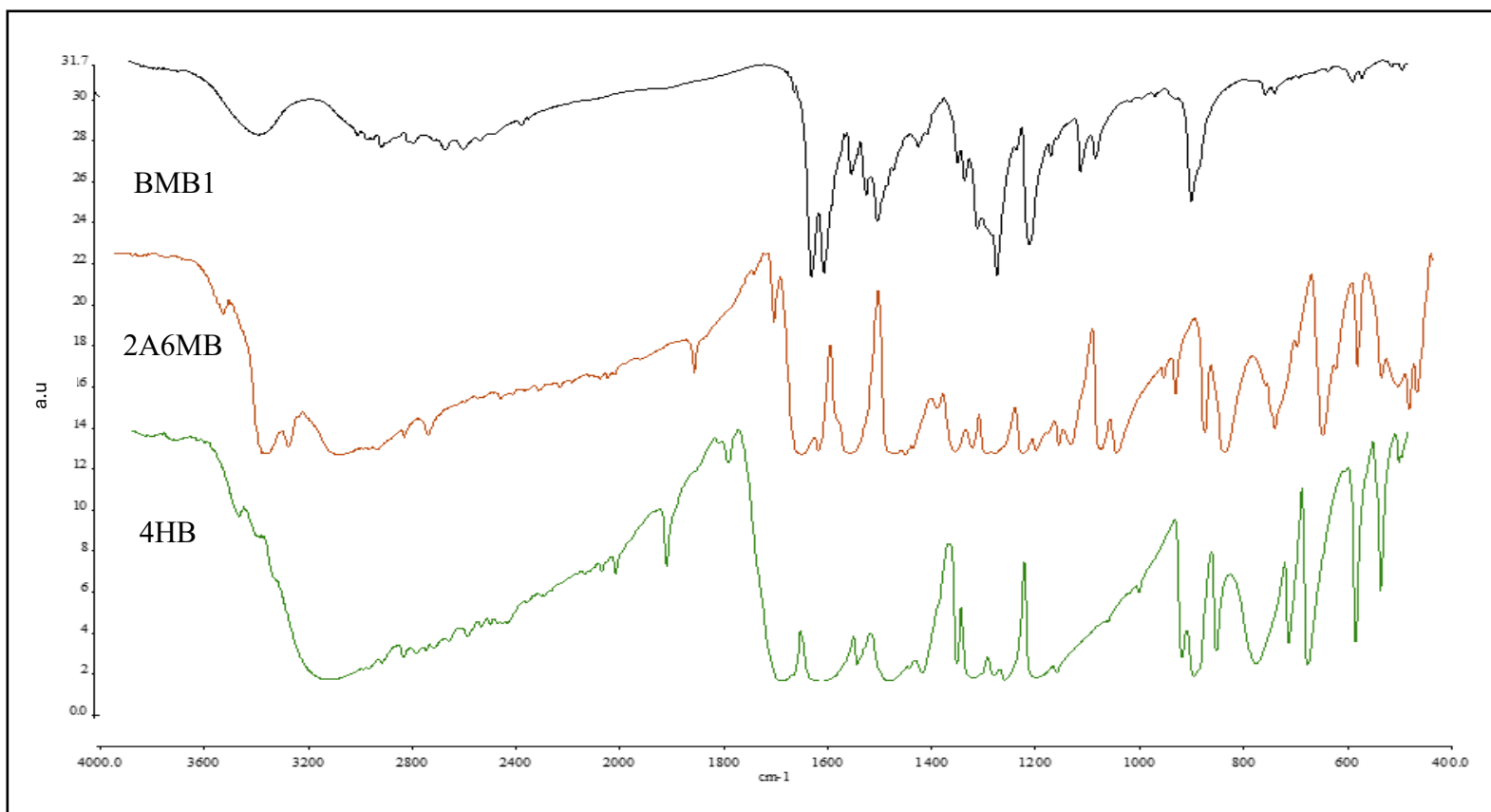


Figure 4.4: FTIR spectra of **BMB1**, 2A6MB, 4HB

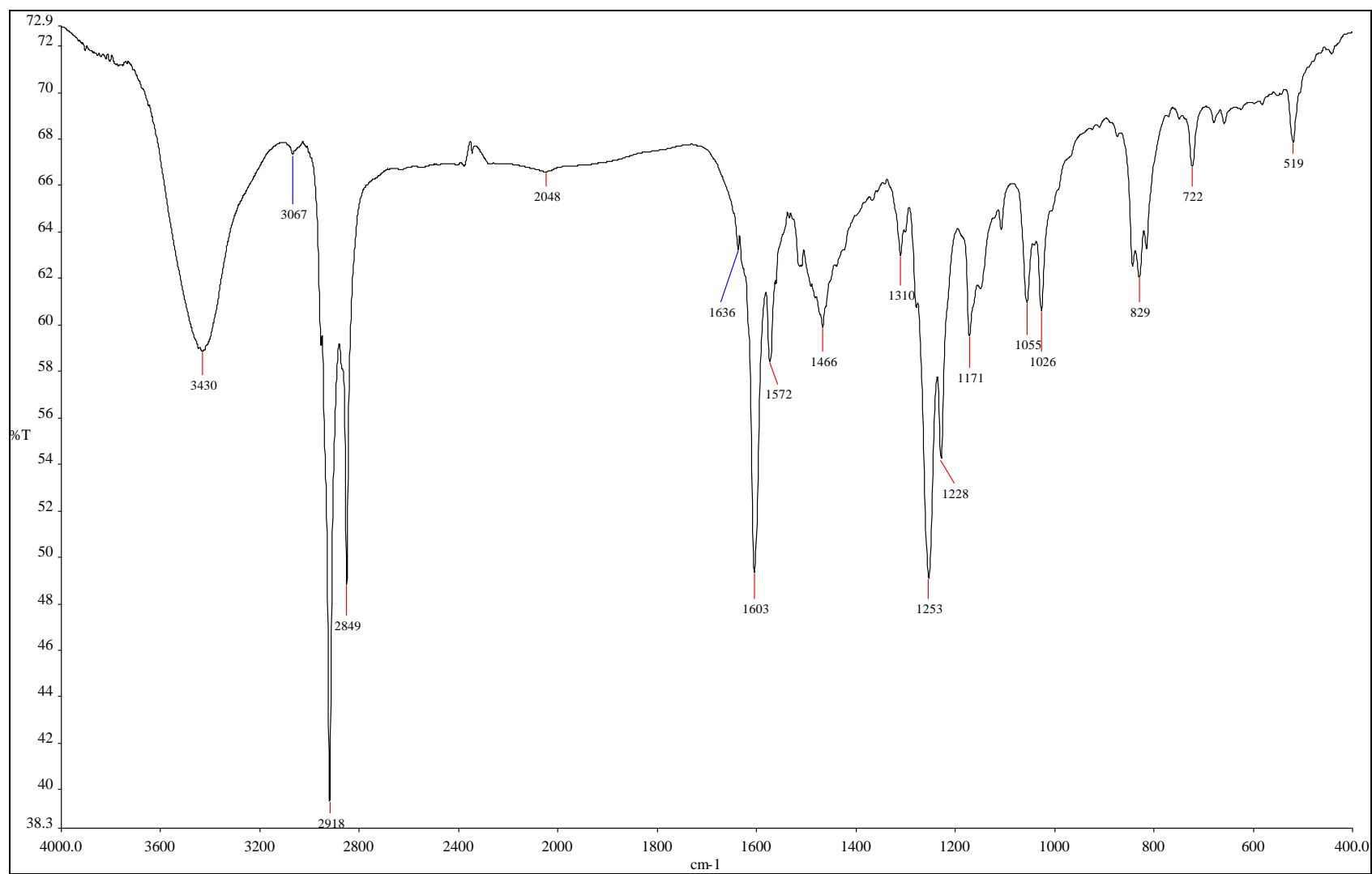


Figure 4.5: FTIR spectrum of **BRLC16**

Table 4.2: FTIR spectral data of 2A6MB, 4HB and **BMB1**

Com- pound	IR $\nu$ (cm <sup>-1</sup> )									
	OH stretching	N-H stretching	sp <sup>2</sup> C-H stretching (aromatic)	sp <sup>3</sup> C-H stretching (aliphatic)	C=O stretching	C=N stretching (benzo- thiazole)	C=N stretching (Schiff Base)	C=C stretching	C-N stretching	C-O stretching
<b>2A6MB</b>	-	3399, 3369 (s)	3111 (s)	2838, 2744 (s)	-	1636 (w)		1544, 1434 (s)	1337 (s)	1259 (s)
<b>4HB</b>	3175 (m)	-	3009 (s)	2878, 2696 (s)	1673 (s)	-	-	1590, 1450 (s)	-	-
<b>BMB1</b>	3431 (m)		-	2810 (m)	-	1577 (s)	1602 (s)	Overlap with C=N (s)	-	1250 (s)

s = strong, m = medium, w = weak

Table 4.3: FTIR spectral data of **BRLCn** compounds

Compound	IR $\nu$ (cm <sup>-1</sup> )				
	OH stretching (free OH)	sp <sup>3</sup> C-H stretching (aliphatic)	C=N stretching (Schiff base)	C=N stretching (benzothiazole)	Ar-O-R (ether)
<b>BRLC12</b>	3431 (m)	2920, 2849 (s)	1598 (m)	1568 (w)	1253 (m)
<b>BRLC14</b>	3446 (m)	2917, 2847 (s)	1596 (m)	1568 (w)	1252 (m)
<b>BRLC16</b>	3430 (m)	2918, 2849 (s)	1603 (m)	1572 (w)	1253 (m)
<b>BRLC18</b>	3430 (m)	2918, 2849 (s)	1603 (m)	1572 (w)	1253 (m)



#### 4.3.2 Attenuated Total Reflection (ATR-FTIR) Analysis of BRLCn

Another FTIR technique, ATR-FTIR is used to confirm the presence of hydroxy group. ATR is used here because it does not involve the preparation of KBr pellet, therefore, absorption of moisture from the atmosphere can be avoided. **BRLC16** spectrum in Figure 4.6 was used as the representative compound to discuss for the functional groups present in **BRLCn**. The ATR-FTIR spectra did not show the OH peak at  $\sim 3400\text{ cm}^{-1}$ . This indicate that the OH group present is free OH group which caused by the moisture from atmosphere. Other than that, ATR-FTIR spectral showing the similar peak as FTIR spectra KBr pellet for **BRLC16**. The ATR-FTIR spectrum shows an  $\text{sp}^3$  C-H stretching absorption band at  $2917$  and  $2849\text{ cm}^{-1}$ . The Schiff base  $\text{C}=\text{N}$  linkage exhibited a characteristic IR absorption band at  $1600\text{ cm}^{-1}$ , while another peak at  $1248\text{ cm}^{-1}$  corresponded to the C-O stretching vibration of the aromatic ether ( $\text{Ar-O-R}$ ), confirming the successful Williamson etherification. The detail data of ATR spectra for final compound (**BRLC12**, **BRLC14**, **BRLC16**, **BRLC18**) was presented in Table 4.4, the spectra were compared in Figure 4.7.

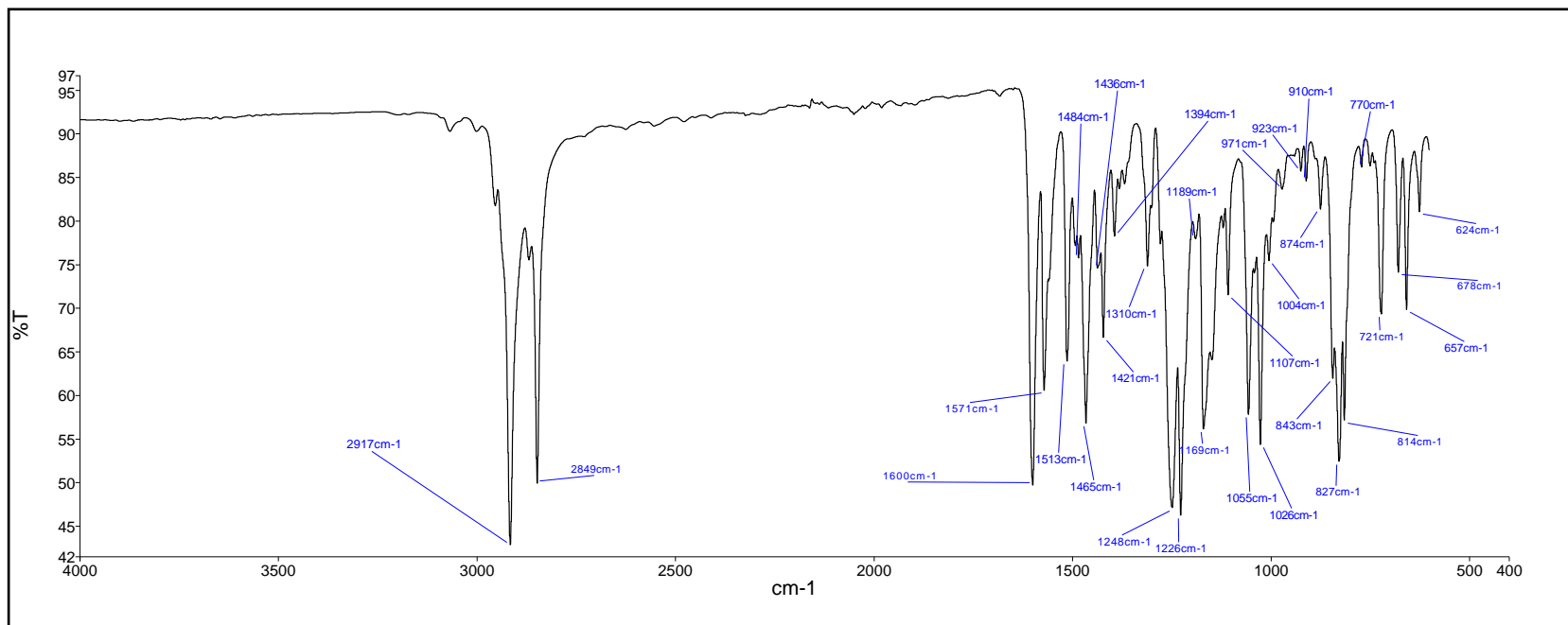


Figure 4.6: ATR-FTIR spectrum of **BRLC16**

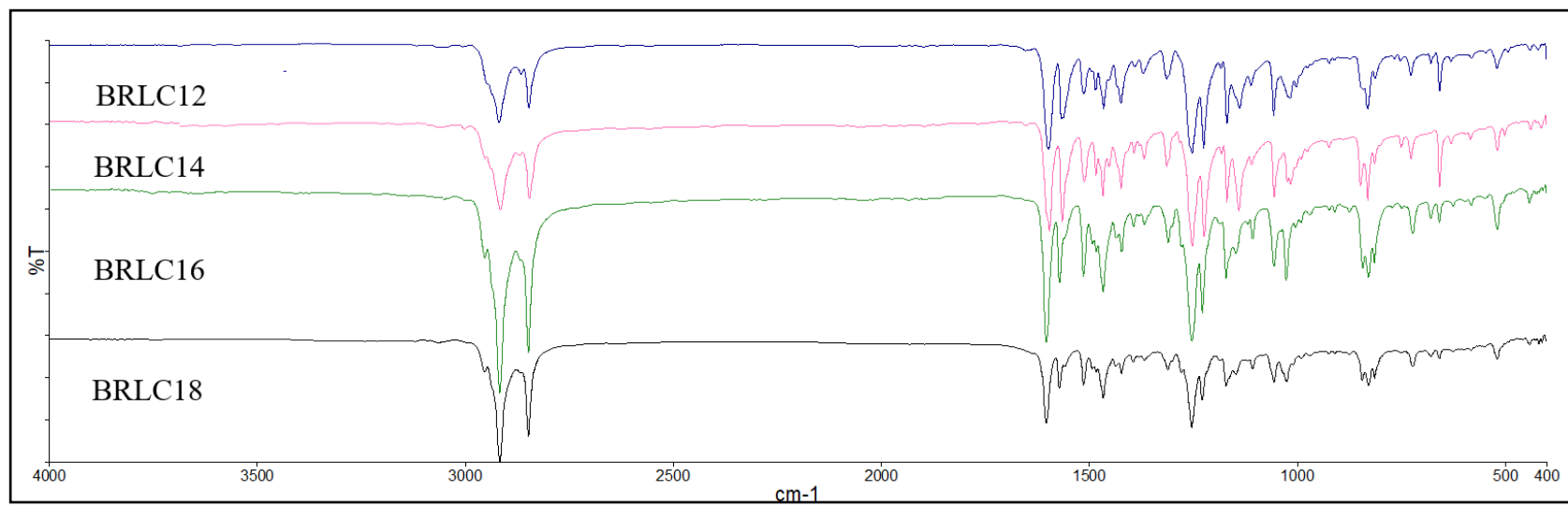


Figure 4.7: Comparison of ATR-FTIR spectra for **BRLC<sub>n</sub>**

Table 4.4: ATR spectral data of **BRLCn** compounds

Compound	IR $\nu$ (cm <sup>-1</sup> )			
	sp <sup>3</sup> C-H stretching (aliphatic)	C=N stretching (Schiff base)	C=N stretching (benzothiazole)	Ar-O-R (ether)
<b>BRLC12</b>	2920, 2848 (s)	1593 (m)	1560 (w)	1252 (m)
<b>BRLC14</b>	2916, 2847 (s)	1595 (m)	1563 (w)	1250 (m)
<b>BRLC16</b>	2917, 2849 (s)	1600 (m)	1571 (w)	1248 (m)
<b>BRLC18</b>	2917, 2849 (s)	1601 (m)	1572 (w)	1252 (m)

s = strong, m = medium, w = weak

## 4.4 Nuclear Magnetic Resonance (NMR)

### 4.4.1 $^1\text{H}$ NMR Spectral Analysis

NMR spectroscopic analysis was conducted on **BRLC16** as a representative compound from the series. The spectrum is shown in Figure 4.8 and the detailed peak assignment is tabulated in Table 4.5.

The  $^1\text{H}$  NMR spectrum of **BRLC16** displayed a characteristic signal at  $\delta$  8.88, which was assigned to the azomethine proton (H11,  $-\text{CH}=\text{N}-$ ), similar to the previous reports (Ha *et al.*, 2010a). This proved the presence of Schiff base in **BRLC16**. In compound **BRLC16**, a triplet signal was observed at  $\delta$  0.86. This signal is located at the most upfield region which belongs to the  $\text{CH}_3$  group of the long alkyl chain, labelled as H34. A signal was observed at  $\delta$  1.24 – 1.36, this is the only multiplet signal correspond to the  $\text{CH}_2$  proton in the long alkyl chain represented by H22-33. At  $\delta$  1.70, a pentet signal was observed, it represents H20 that having four neighbour proton from two adjacent methylene groups. Similarly, a pentet signal was observed at  $\delta$  1.45, it represents H21 that also having four neighbour protons from two adjacent methylene groups. The terminal methoxy proton (H17,  $-\text{OCH}_3$ ) in **BRLC16** appeared as a singlet at  $\delta$  3.86. This proton appeared downfield relative to other aliphatic protons because of its closer position to the electron-withdrawing oxygen atom. Another signal for triplet at  $\delta$  4.01 represented by the methylene proton who bonded to a carbonyl group (C-O) assigned as H19.

From  $\delta$  6.95 – 7.94, show the region for aromatic proton. There is a total seven aromatic protons shown by the five obvious signals at downfield region  $^1\text{H}$  spectrum of **BRLC16**. For H13 and H13' they have a doublet signal at  $\delta$  7.94,  $J = 8.8$  Hz. The protons are *ortho* to the electro-withdrawing imine ( $-\text{CH}=\text{N}-$ ) group. Protons *ortho* to substituents tend to experience a greater anisotropic effect, especially near planar  $\pi$ -systems like  $\text{C}=\text{N}$  or aromatic heterocycles. Therefore, H13 and H13' experience the stronger deshielding effects. For H9, it is having the signal for doublet at  $\delta$  7.83. It located on the benzothiazole ring and *ortho* to nitrogen, which is strongly electron-withdrawing. The electron deficiency due to heteroatoms leads to a strong deshielding effect. As a result, it is significantly deshielded, but slightly less than H13 and H13'. There is also one singlet signal which indicates by H6 at the  $\delta$  7.26. It located on the benzothiazole ring, and *ortho* to sulphur. It shows less withdrawing property than nitrogen. It slightly more shielded than H9 due to lower electronegativity of sulphur compared to nitrogen. For H8, it is a doublet signal show at  $\delta$  7.03. It located at a *meta*-position to nitrogen in the benzothiazole ring, and hence less directly influenced by heteroatoms. Therefore, it appears at upfield as compared to H6 and H9. Last but not least, H14 and H14' is the least deshielded protons in the aromatic region. As both protons are *meta* to the  $\text{C}=\text{N}$  imine, therefore no strong anisotropic or are directly acting on them. Thus, it appears in upfield as compared to other protons.

Table 4.5: Details data of  $^1\text{H}$  NMR for **BRLC16** in  $\text{CDCl}_3$

Proton number	Chemical shift, $\delta$ ppm	Coupling constant, $J$ (Hz)	Integrals	Multiplicity*
11	8.88	-	1	s
13,13'	7.94	8.8	2	d
9	7.83	9.2	1	d
6	7.26	-	1	s
8	7.03	8.8	1	d
14,14'	6.98	8.8	2	d
19	4.01	6.8	2	t
17	3.86	-	3	s
20	1.79	8.0	2	p
21	1.45	7.6	2	p
22-33	1.24 – 1.36	-	24	m
34	0.86	6.8	3	t

TMS was served as internal standard

$\text{CDCl}_3$  was used as solvent

\*s = singlet

t = triplet

p = pentet

m = multiplet

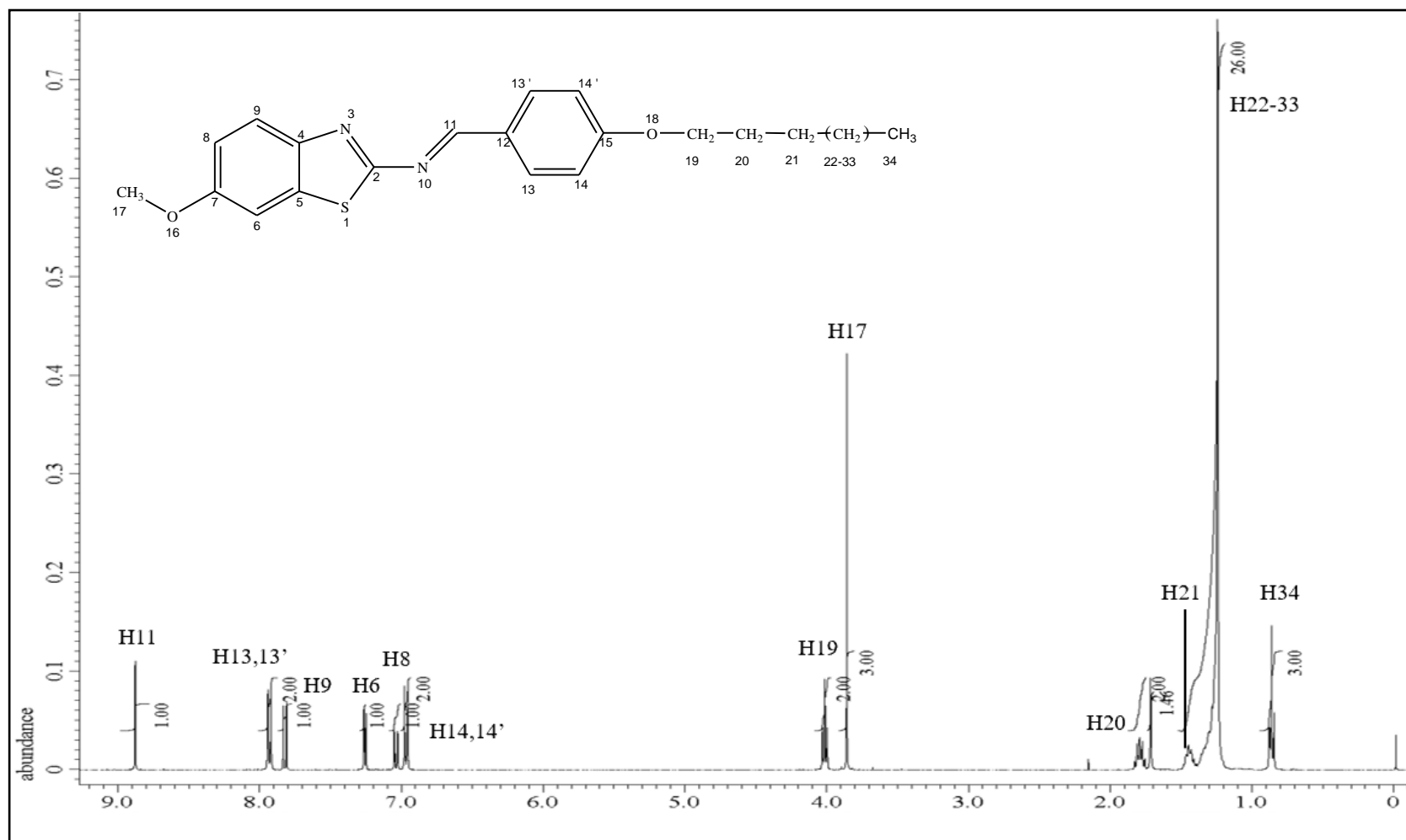


Figure 4.8: <sup>1</sup>H NMR spectrum for **BRLC16**



#### 4.4.2 $^{13}\text{C}$ NMR Spectral Analysis

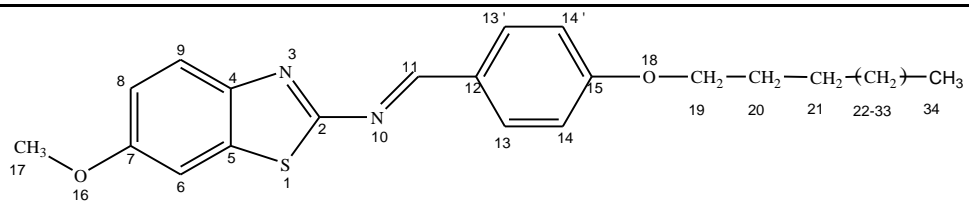
In  $^{13}\text{C}$  NMR analysis, **BRLC16** (Figure 4.9) is chosen as the representative to be discussed from a series of **BRLCn** compounds. The  $^{13}\text{C}$  NMR spectrum show characteristic signals corresponding to methane (CH), methylene ( $\text{CH}_2$ ), methyl ( $\text{CH}_3$ ), and quaternary carbons. the detailed peak assignment was tabulated in Table 4.6.

In the  $^{13}\text{C}$  NMR spectrum of **BRLC16**, a significant peak observed at  $\delta$  68.45 is assigned to C19 in the alkyloxy chain. The carbon resonance appeared most deshielded in the aliphatic region because of its direct attachment to the electron-withdrawing oxygen atom within the ether functional group ( $-\text{O}-\text{CH}_2-$ ). Peak with  $\delta$  32.02 ppm was assigned to C20. This is because, C20 far away from oxygen atom as compared to C19, therefore, it caused a small upfield shift. Peak with the signal  $\delta$  26.07 and  $\delta$  22.79 belongs to  $\text{sp}_2$  carbon ( $\text{CH}_2$ ) assigned as C21 and C33 respectively. C21 is more upfield than C20 because C21 is three bonds away from the ether oxygen, it's at the gamma position. The gamma effect ( $\gamma$ -effect) arises, which refers to the shielding influence of a substituent group (like an ether,  $-\text{O}-$ ) on a carbon atom that is three bonds away in NMR spectroscopy. A strong peak at  $\delta$  29.79 – 29.46, appearing as a multiplet, corresponds to the long aliphatic methylene ( $\text{CH}_2$ ) chain and is assigned to carbons C22 – C32. The methyl carbon ( $-\text{CH}_3$ ) of compound **BRLC16**, C34 appeared at  $\delta$  14.23, showing an upfield shift due to its distance from electronegative atoms. In the aliphatic photon shifting region, there are also a significant peak observed at  $\delta$  55.87. It is

assigned as C17. The proton resonated further downfield compared to other aliphatic protons because of electron-withdrawing characteristic of oxygen atom. Other than that, an intense peak with multiplet signal,  $\delta$  77.45 – 76.81 refers to the CDCl<sub>3</sub> solvent peak (Babij *et al.*, 2016).

At the downfield region, the signals appeared at the range of  $\delta$  163.50 – 104.56 show the presence of twelve carbons in aromatic ring from C4 –C9 and C12 – C15. The most deshielded carbon, C2 appeared at  $\delta$  169.99, reflecting its position between two electronegative atoms (nitrogen and sulphur) in the -N=C-S- segment. The subsequent signal at  $\delta$  164.54 was assigned to C11 of the Schiff base linkage (C=N). The following signal of  $\delta$  163.50 belongs to the carbon of carbonyl group (C=O), C15. This is due to the sp<sup>2</sup> hybridization of the carbon, which is directly bonded to electronegative oxygen atoms, causing an enhanced deshielding effect. For benzothiazole ring C4, C5, C7, there are directly bonded to different electronegative atoms which are nitrogen sulphur and oxygen, respectively. The oxygen atom is most electronegative compared to nitrogen and sulphur. Therefore, C7 ( $\delta$  157.59) is most deshielded among C4 ( $\delta$  146.21) and C5 ( $\delta$  135.62). There are six distinct intense peaks observed within  $\delta$  132.24 – 104.56 indicated eight aromatic carbons, which are C13 and C13' ( $\delta$  132.24), C12 ( $\delta$  127.62), C9 ( $\delta$  123.56), C8 ( $\delta$  115.49), and C14 and C14' ( $\delta$  115.04), C6 ( $\delta$  104.56).

Table 4.6: Details data of  $^{13}\text{C}$  NMR for **BRLC16** in  $\text{CDCl}_3$

	
Chemical Shift, $\delta$ (ppm)	Carbon number
169.99	2
164.54	11
163.50	15
157.59	7
146.21	5
135.62	4
132.24	13,13'
127.62	12
123.56	9
115.49	8
115.04	14,14'
104.56	6
68.45	19
55.87	17
32.02	20
29.79	22-32 <sup>a</sup>
29.76	
29.69	
29.66	
29.46	
29.19	
26.07	21
22.79	33
14.23	34

TMS was served as internal standard

$\text{CDCl}_3$  was used as solvent

<sup>a</sup> Some of the signals attributed to the C22-32 atoms appear in the same column resulting in less than 11 signals in the spectrum.

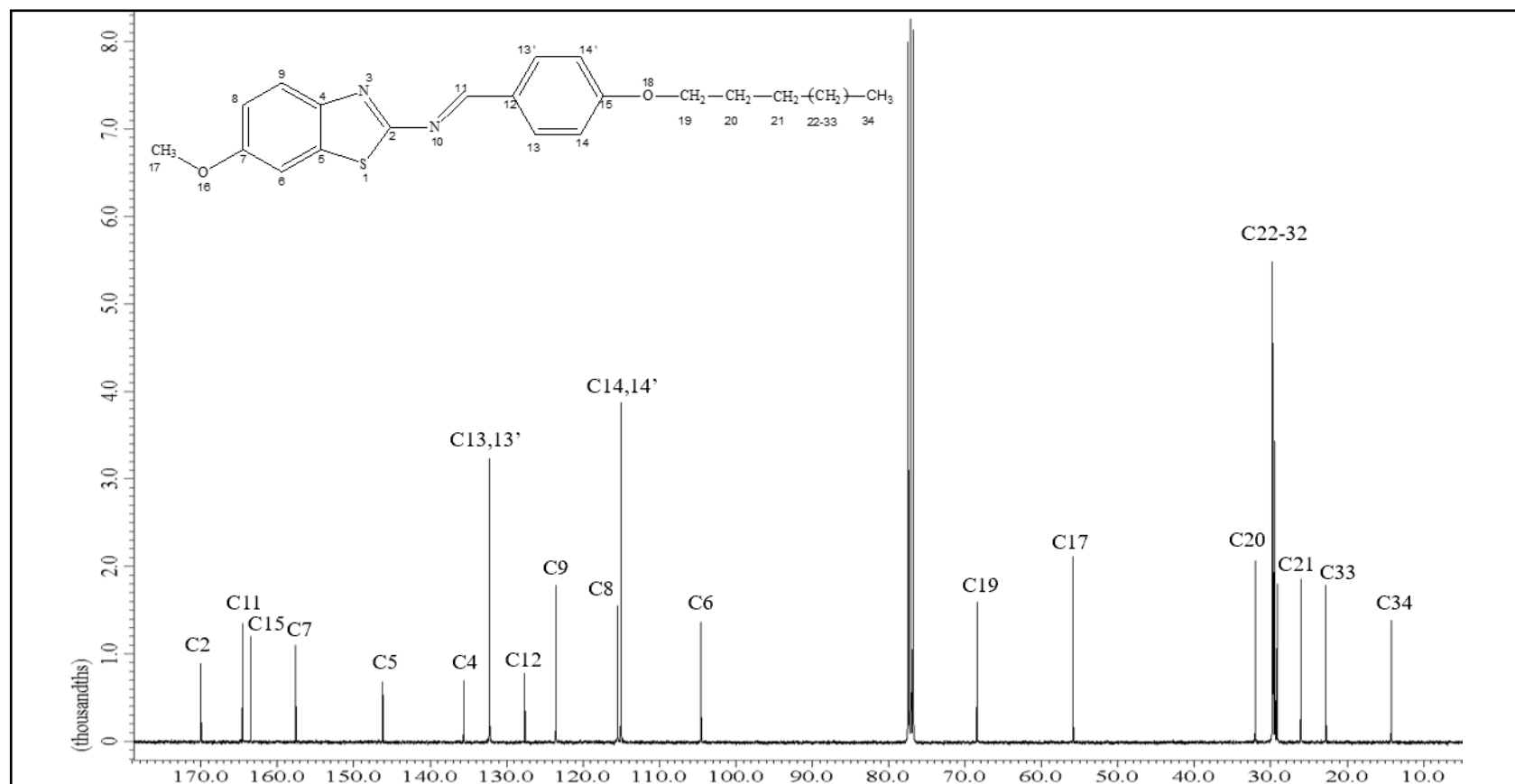


Figure 4.9:  $^{13}\text{C}$  NMR spectrum for **BRLC16**

#### 4.4.3 2D COSY NMR Spectral Analysis

**BRLC16** is used as the representative compound of the **BRLCn** series in the homonuclear correlation spectroscopy (COSY) analysis. The COSY spectrum of **BRLC16** is illustrated in Figure 4.10. The detailed peak assignment was tabulated in Table 4.7. COSY reveals coupling between homonuclear nuclei which is in this case, proton-proton couplings. The diagonal signals in the COSY spectrum represent individual protons within the molecule, while the off-diagonal, symmetrical cross-peaks indicate coupling interactions between different protons.

A distinct correlation is observed between H34 ( $\delta$  0.86) and the methylene protons H22 to H33 ( $\delta$  1.24 – 1.36). Another distinct cross-peak is seen between H19 ( $\delta$  4.01) and H20 ( $\delta$  1.79), confirming their spin-spin coupling. In the downfield region, signals corresponding to aromatic protons of benzene rings are detected. Two doublet peaks are observed, indicating the presence of symmetry benzene rings in the **BRLC16** structure. Specifically, H13 and H13' ( $\delta$  7.94) show correlation with H14 and H14' ( $\delta$  6.98). Other than that, H9 ( $\delta$  7.83) is correlated with H8 at  $\delta$  7.03. H11 ( $\delta$  8.88) does not exhibit any coupling with other protons, which is consistent with its assignment as part of the Schiff base ( $\text{-HC=N}$ ) group.

Table 4.7:  $^1\text{H}$ - $^1\text{H}$  correlations from the 2D COSY NMR for **BRLC16**

Numbering of H	$^1\text{H}$ - $^1\text{H}$ COSY correlations
H11	--
H13,13'	H14,14'
H9	H8
H6	--
H8	H9
H14,14'	H13,13'
H17	--
H19	H20
H20	H19, H21
H21 <sup>b</sup>	H20, H22-33
H34 <sup>c</sup>	H22-33

TMS was served as internal standard

<sup>b</sup> The H21 atom correlates with the methylene protons (H22-33) but their real position could not be determined because the  $^1\text{H}$  chemical shifts of the H22-33 were indistinguishable

<sup>c</sup> The H34 atom correlates with the methylene protons (H22-33) but their real position could not be determined because the  $^1\text{H}$  chemical shifts of the H22-33 were indistinguishable

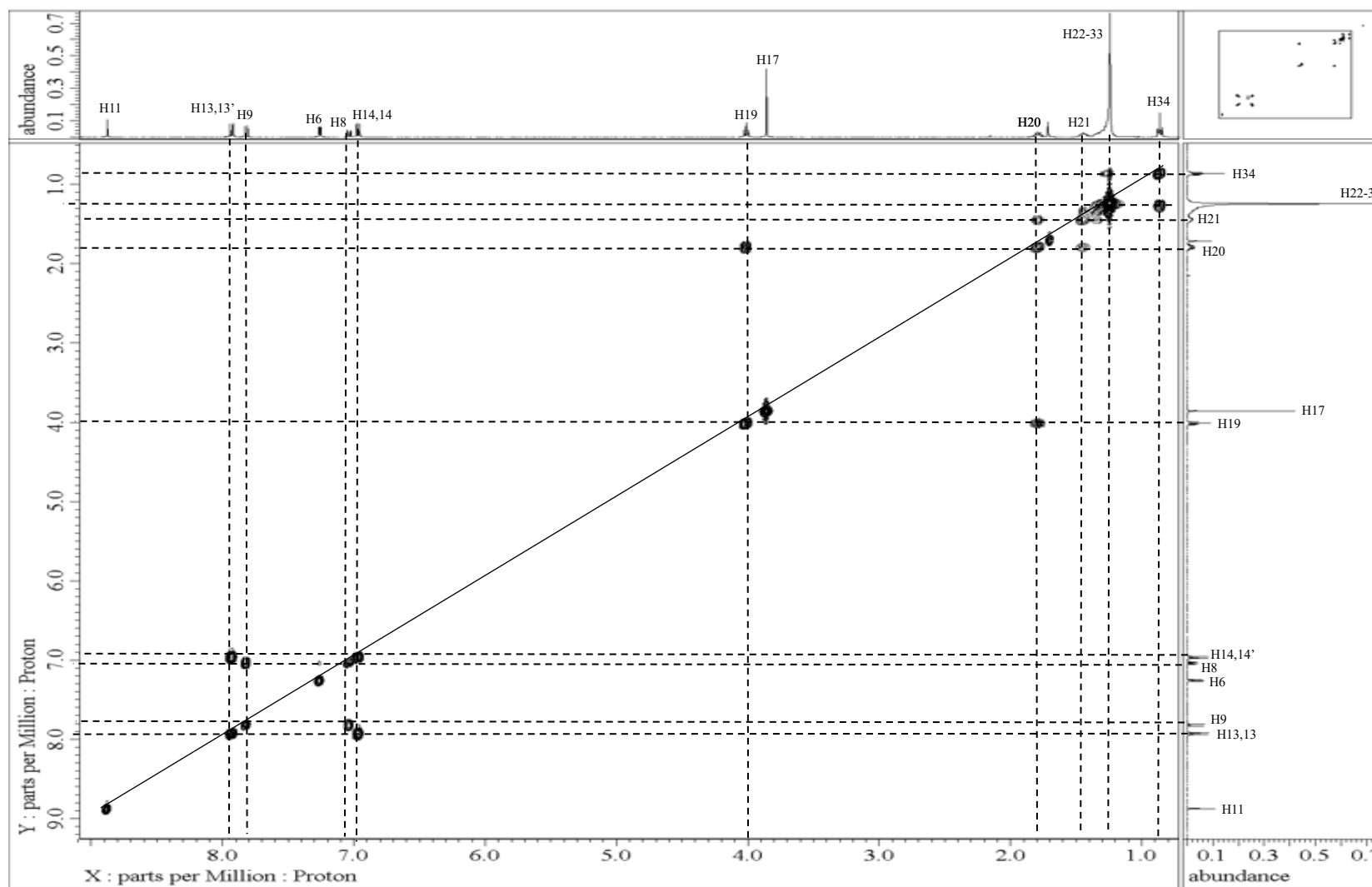


Figure 4.10: 2D COSY NMR spectrum for **BRLC16**

#### 4.4.4 2D HMQC NMR Spectral Analysis

Figure 4.11 shows the 2D Heteronuclear Multiple Quantum Coherence (HMQC) between one bond proton and carbons for compound **BRLC16**. The detailed peak assignment was tabulated in Table 4.8.

In the spectrum for **BRLC16**, H34 ( $\delta$  0.86, CH<sub>3</sub>) correlated with C34 ( $\delta$  14.23, CH<sub>3</sub>) showing the end of the alkyl chain in **BRLC16**. Similar type of the correlation was observed for long alkyl chain, H22 – H33 ( $\delta$  1.24 – 1.36, CH<sub>2</sub>) with C20 ( $\delta$  32.02, CH<sub>2</sub>), C22 – C32 ( $\delta$  29.66, CH<sub>2</sub>), C21 ( $\delta$  26.07, CH<sub>2</sub>) and C33 ( $\delta$  22.79, CH<sub>2</sub>). The H21 ( $\delta$  1.45, CH<sub>2</sub>) correlated with C21 ( $\delta$  26.07, CH<sub>3</sub>), while H20 ( $\delta$  1.79, CH<sub>2</sub>) correlated with C20 ( $\delta$  32.02, CH<sub>2</sub>). In **BRLC16**, carbon in the terminal methoxy group (-OCH<sub>3</sub>-), C17, appeared at  $\delta$  55.87 correlate with H17 ( $\delta$  3.86). The downfield chemical shifts resulted from deshielding effects induced by the electron-withdrawing oxygen atom. The H19 ( $\delta$  4.01, CH<sub>2</sub>) correlated with C19 ( $\delta$  68.45, CH<sub>2</sub>). The signals H19 and C19 is higher than at H21-33 and C21-31 due to their positions that near to the ether linkage. The upfield region (highly shielded) shows the signals for alkyl chain, the down field region which also referring to those less shielded signal belongs to aromatic and quaternary carbons.

H14 and H14' ( $\delta$  6.98) correlated with C14 and C14' ( $\delta$  115.04) as well as the correlation between H13 and H13' ( $\delta$  7.94) with C13 and C13' ( $\delta$  132.24) show the benzene ring at the lateral part of the structure. For the benzene ring of



benzothiazole ring, the structure represents by C4 – C9. With that, H8 ( $\delta$  7.03) correlated with C8 ( $\delta$  115.49) while H6 ( $\delta$  7.26) correlated with C6 ( $\delta$  104.56) and H9 ( $\delta$  7.83) correlated with C9 ( $\delta$  123.56). The HMQC spectrum of compound **BRLC16** revealed a direct heteronuclear correlation between the azomethine carbon, C11 ( $\delta$  164.54) and its corresponding proton H11 ( $\delta$  8.88), thereby confirming the presence of the C=N linkage. For C2, C4, C5, C7, C12, and C15 does not show HMQC signals as they did not bond with H.

Table 4.8:  $^1\text{H}$ - $^{13}\text{C}$  correlations from the 2D HMQC NMR for **BRLC16**

Position	$^1\text{H}$ (ppm)	Position of $^{13}\text{C}$ (ppm) (One bond coupling)
11	8.88	C11 (164.54)
13,13'	7.94	C13,13' (132.24)
9	7.83	C9 (123.56)
6	7.26	C6 (104.58)
8	7.03	C8 (115.49)
14,14'	6.98	C14,14' (115.04)
19	4.01	C19 (68.45)
17	3.86	C17 (55.87)
20	1.79	C20 (32.02)
21	1.45	C21 (26.07)
22-33	1.24 – 1.36	C20 (32.02), C22-32 (29.79, 29.76, 29.69, 29.66, 29.46, 29.13), C21 (26.07) C33 (22.79)
34	0.86	C34 (14.23)

TMS was used as internal standard

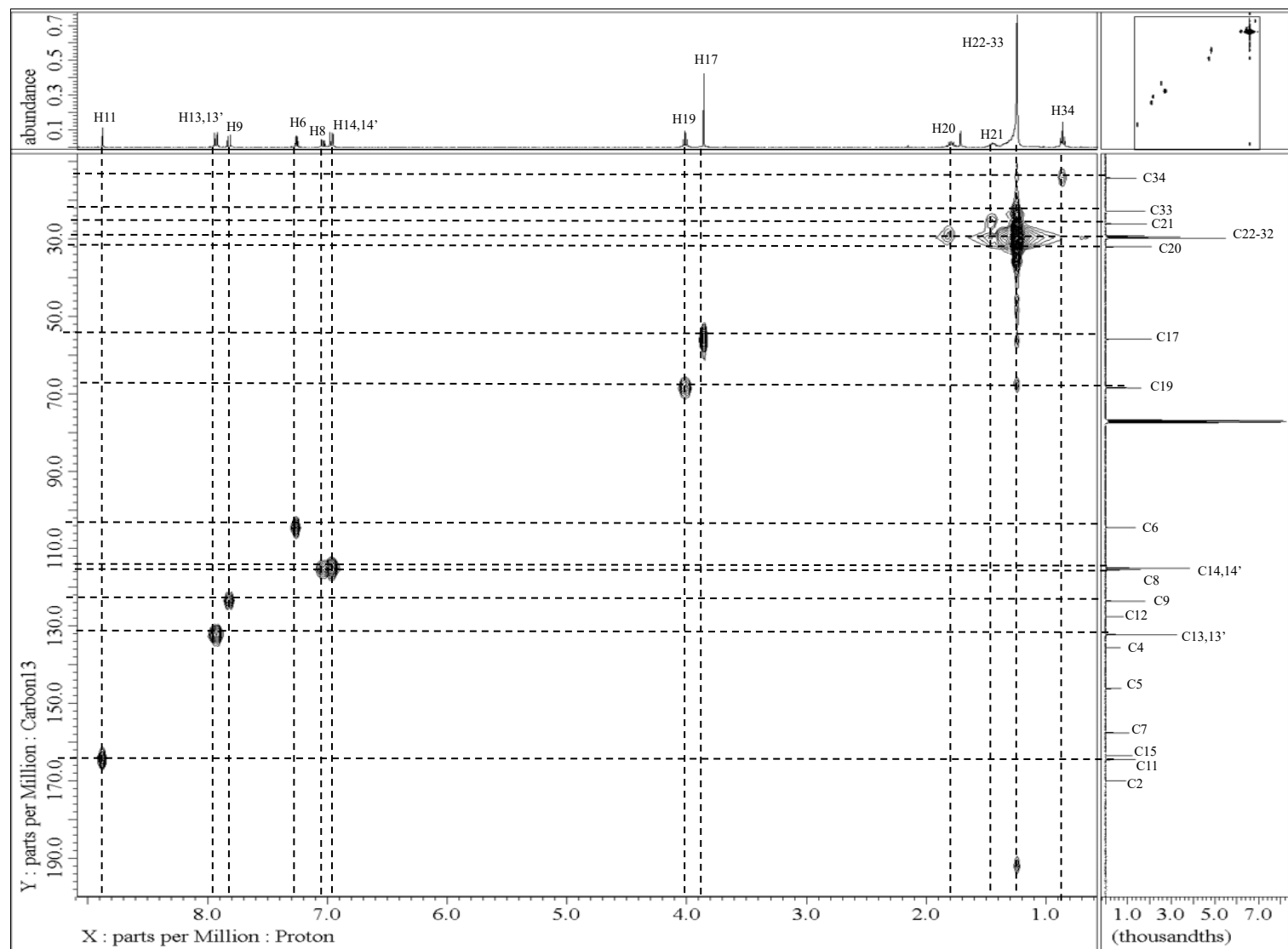


Figure 4.11: 2D HMQC NMR spectrum for **BRLC16**

#### 4.4.5 2D HMBC NMR Spectrum

In heteronuclear multiple bond correlation (HMBC), **BRLC16** is used as the representative compound for this discussion. The HMBC spectrum of **BRLC16**, along with its corresponding details, is presented in Figure 4.12 and summarized in Table 4.9.

HMBC gives correlations between carbons and protons that are separated by two, three, and, sometimes in conjugated systems, four bonds. Direct one-bond correlations are not observed. The quaternary carbons can be assigned using HMBC experiment. From the HMBC spectrum of **BRLC16**, there is correlation between H34 ( $\delta$  0.86) with C33 ( $\delta$  22.79), C21 ( $\delta$  26.07), and with long alkyl chain C22 – C32 ( $\delta$  29.79 – 29.13). H21 ( $\delta$  1.45) correlated with long alkyl chain C22 – C32 ( $\delta$  29.79 – 29.13). For H19 ( $\delta$  4.01) shows correlation with C15 ( $\delta$  163.50), C21 ( $\delta$  26.07), long alkyl chain C22 – C32. For H17 ( $\delta$  3.86), it shows correlation with C7 ( $\delta$  157.59). The HMBC spectrum shows key long-range correlations that is, H13,13' showed cross-peaks with C11 at  $\delta$  164.54, C12 at  $\delta$  127.62 and, C15 at  $\delta$  163.50. Similarly, C11 at  $\delta$  164.54 is assigned through its correlations with the adjacent H13,13'. Meanwhile, H14,14' correlated with C12 ( $\delta$  127.62) and C15 ( $\delta$  163.50). These observations strongly support the proposed atomic connectivity.

The quaternary carbons—C15, C12, C7, C5, C4 and C2 also exhibit correlations with nearby protons. C15 ( $\delta$  163.50), which corresponds to the ether

carbon, shows correlations with H19 ( $\delta$  4.01), as well as H14,14' ( $\delta$  6.98), also H13,13' ( $\delta$  7.94). Second quaternary carbon, C12 ( $\delta$  127.62) correlates with H14,14', as well as H13,13', also H11 ( $\delta$  8.88). Third quaternary carbon, C7 ( $\delta$  157.59), correlate with H17 ( $\delta$  3.86), H9 ( $\delta$  7.83), H8 ( $\delta$  7.03) and H6 ( $\delta$  7.26). For the fourth quaternary carbon, C5 ( $\delta$  146.21) correlate with H6 ( $\delta$  7.26) and H8 ( $\delta$  7.03). Next, C2 ( $\delta$  169.99) shows correlations with H11. Similarly, C4 ( $\delta$  135.62) correlate with H9 ( $\delta$  7.83) and H6 ( $\delta$  7.26).

Table 4.9:  $^1\text{H}$ - $^{13}\text{C}$  correlations from the 2D HMBC NMR for **BRLC16**

Position	$^1\text{H}$ (ppm)	Position of $^{13}\text{C}$ (ppm) (Long range coupling)
11	8.88	C2 (169.99), C12 (127.62), C13,13' (132.24)
13,13'	7.94	C11 (164.54), C12 (127.62), C15 (163.50)
9	7.83	C4 (135.62), C7 (157.59)
6	7.26	C4 (135.62), C5 (146.21), C7 (157.59), C8 (115.49)
8	7.03	C6 (104.56), C5 (146.21), C7 (157.59)
14,14'	6.98	C12 (127.62), C15 (163.50)
19	4.01	C15 (163.50), C21 (26.07), C22-32 (29.79, 29.76, 29.69, 29.66, 29.46, 29.13)
17	3.86	C7 (157.59)
20	1.79	C19 (68.45), C21 (26.07)
21	1.45	C22-32 (29.79, 29.76, 29.69, 29.66, 29.46, 29.13)
34	0.86	C22-32 (29.79, 29.76, 29.69, 29.66, 29.46, 29.13), C21 (26.07), C33 (22.79)

TMS was used as internal standard

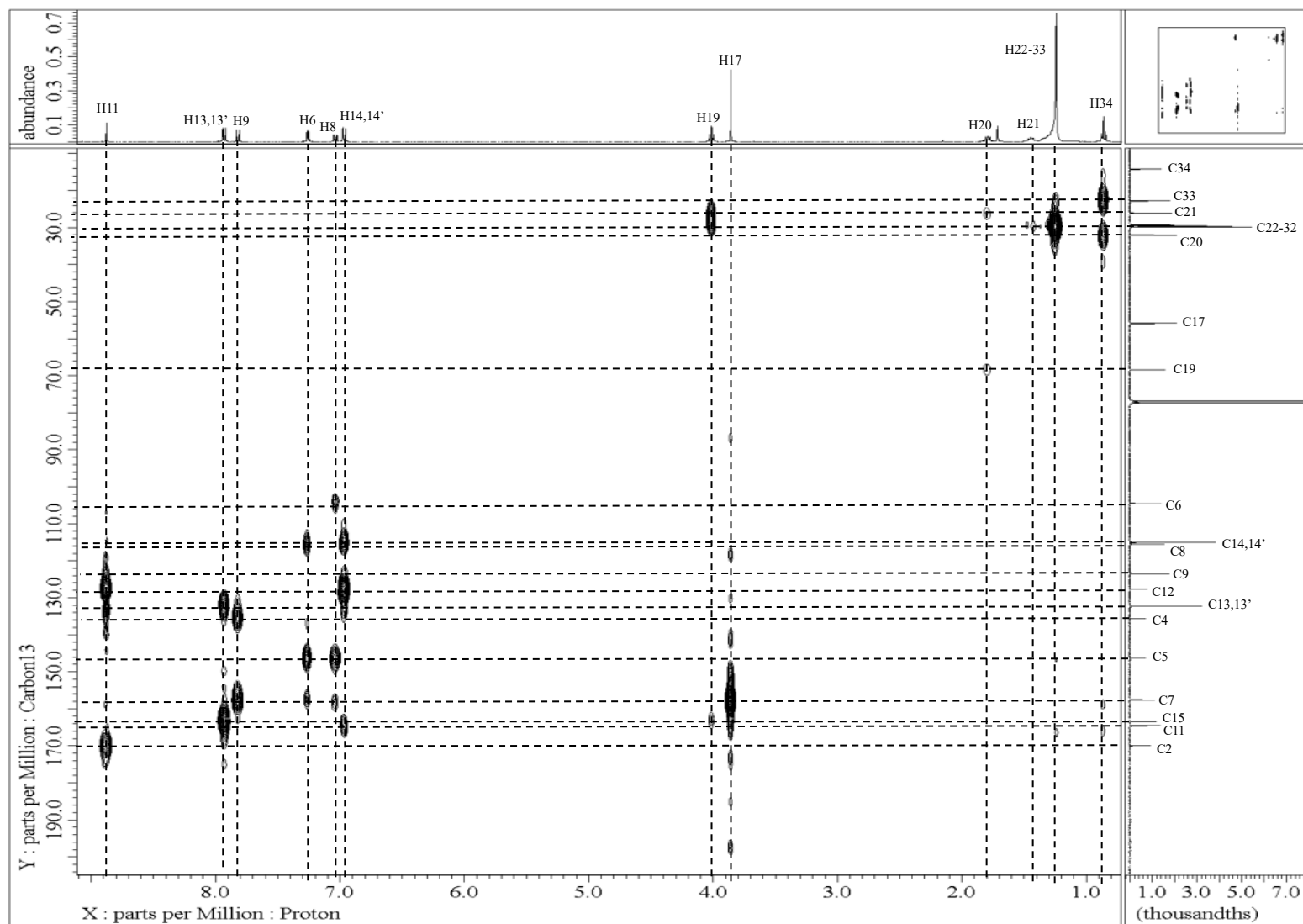


Figure 4.12: 2D HMBC NMR spectrum for **BRLC16**

## 4.5 Liquid Crystalline Properties

### 4.5.1 Differential Scanning Calorimetry Analysis

Differential Scanning Calorimetry (DSC) analysis was used to characterize phase transitions in the **BRLCn** series, quantifying the enthalpy changes corresponding to each thermal transition. **BRLC16**, was used as the representative compound and its DSC thermogram is presented in Figure 4.13. The detailed data for the **BRLCn** series, where  $n = 12, 14, 16$ , and  $18$ , along with their corresponding enthalpy changes, are presented in Table 4.10.

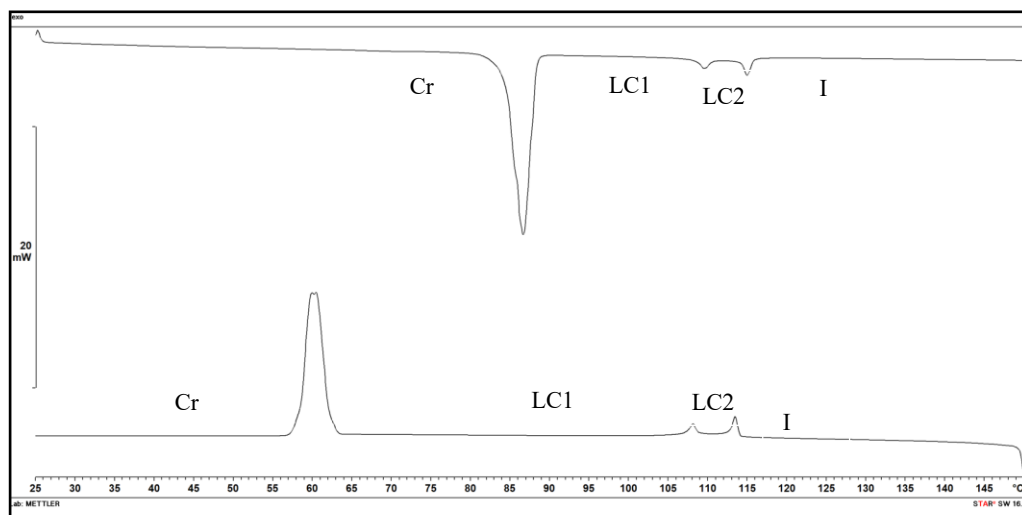


Figure 4.13: DSC thermogram for **BRLC16**

During the heating cycle, three peaks were observed. The first peak at  $86.06\text{ }^{\circ}\text{C}$  ( $\Delta H = 48.02\text{ kJ}\cdot\text{mol}^{-1}$ ) corresponds to the transition from a crystalline (Cr) phase to a liquid crystal 1 (LC1) phase in **BRLC16**. Upon further heating, a second peak that is small appears at  $109.47^{\circ}\text{C}$  ( $\Delta H = 0.50\text{ kJ}\cdot\text{mol}^{-1}$ ), indicating



the transition from the liquid crystal 1 (LC1) phase to a liquid crystal 2 (LC2) phase. Finally, at 114.86 °C ( $\Delta H = 1.18 \text{ kJ}\cdot\text{mol}^{-1}$ ), the LC2 phase transitions into the isotropic (I) liquid phase. It is observed that the enthalpy change for the LC1 to LC2 phase transition is lower than that of the LC2 to I phase transition. Moreover, the LC2 to I transition required the significantly smaller of enthalpy changes than that of the Cr to LC1 transition. This trend arises because liquid crystalline phases exhibit greater structural similarity to isotropic liquids than to crystalline solids (Agamanolis, 2018). During the transition from the Cr to LC1 phase, a sharp endothermic peak is observed, indicating that a significant amount of energy is absorbed to break the intermolecular Van der Waals forces present in the crystalline structure of **BRLC16**. This is due to the molecular packing. In the crystalline state, the molecules are tightly packed and arranged in an ordered three-dimensional lattice. The system can change into a less ordered liquid crystal phase when a highly ordered and well-oriented molecular arrangement is disrupted, which takes a significant amount of energy (Concept Group LLC, 2011). In contrast, the transition from the LC2 to I phase produces a smaller endothermic peak, as this transformation involves less disruption of molecular order.

The cooling cycle exhibits three distinct peaks. Upon cooling, the isotropic phase (I) changed to the LC2 phase at 113.53°C ( $\Delta H = 1.03 \text{ kJ}\cdot\text{mol}^{-1}$ ), followed by the LC2 to LC1 phase transition at 108.17°C ( $\Delta H = 0.85 \text{ kJ}\cdot\text{mol}^{-1}$ ). As the cooling process continues LC1 to Cr occurred at 60.48 °C ( $40.23 \text{ kJ}\cdot\text{mol}^{-1}$ ). All three peaks observed during the cooling cycle correspond to exothermic transitions, where energy is released as intermolecular bonds are reformed.

Among them, the LC1 to Cr phase transition exhibits the largest enthalpy change, as an excess of energy must be released to recover back the highly ordered crystalline structure with strong intermolecular interactions. In contrast, the LC2 to LC1 transition involves the release of a smaller amount of energy, since the transformation occurs between two liquid crystalline phases that are both relatively disordered. A significant amount of energy is released during the recrystallization of the liquid crystal into a crystalline phase, as the molecules rearrange into a well-oriented, organized, and highly ordered structure stabilized by strong intermolecular forces. The supercooling behaviour observed in this series before the recrystallization allows LC1 to remain metastable below the melting temperature, resulting in a wider observable temperature range compared to LC2. As demonstrated by **BRLC16**'s DSC thermogram, the compound exhibits the following molecular orientation:

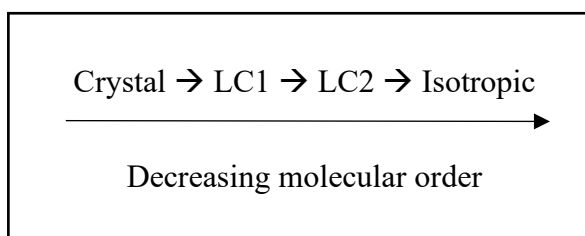


Table 4.10: Transition temperature for heating and cooling of the compound **BRLC<sub>n</sub>**, where n = 12, 14, 16, and 18

Compound	Molar mass, g/mol	Cycle	Phase transition	Temperature, °C	\Delta H  (kJ·mol <sup>-1</sup> )
<b>BRLC12</b>	452.65	Heating	Cr → LC1	72.13	39.30
			LC1 → LC2	101.07	0.41
			LC2 → I	120.94	0.71
		<i>Cooling</i>	<i>I → LC2</i>	<i>119.11</i>	<i>0.49</i>
			<i>LC2 → LC1</i>	<i>101.25</i>	<i>0.63</i>
			<i>LC1 → Cr</i>	<i>45.26</i>	<i>18.04</i>
<b>BRLC14</b>	480.71	Heating	Cr → LC1	80.41	47.53
			LC1 → LC2	106.94	0.52
			LC2 → I	118.16	0.83
		<i>Cooling</i>	<i>I → LC2</i>	<i>117.99</i>	<i>1.15</i>
			<i>LC2 → LC1</i>	<i>107.02</i>	<i>0.60</i>
			<i>LC1 → Cr</i>	<i>64.10</i>	<i>31.36</i>
<b>BRLC16</b>	508.76	Heating	Cr → LC1	84.19	48.02
			LC1 → LC2	108.69	0.50
			LC2 → I	114.18	1.18
		<i>Cooling</i>	<i>I → LC2</i>	<i>114.03</i>	<i>1.03</i>
			<i>LC2 → LC1</i>	<i>108.83</i>	<i>0.85</i>
			<i>LC1 → Cr</i>	<i>62.26</i>	<i>40.23</i>
<b>BRLC18</b>	536.81	Heating	Cr → LC1	88.91	56.94
			LC1 → LC2	111.02	0.71
			LC2 → I	112.63	0.64
		<i>Cooling</i>	<i>I → LC2</i>	<i>112.44</i>	<i>1.03</i>
			<i>LC2 → LC1</i>	<i>111.00</i>	<i>0.57</i>
			<i>LC1 → Cr</i>	<i>91.11</i>	<i>48.91</i>

Note: Cr = Crystal; LC1 = Liquid crystal 1; LC2 = Liquid crystal 2; I = Isotropic

#### 4.5.2 Effects of Number of Carbons at the Alkyloxy Chain on the Transition Temperature

Figure 4.14 presents the phase transition behaviour of the **BRLC<sub>n</sub>** series, showing the dependence of both melting (Cr→LC1) and clearing (LC2→I) temperatures on the alkyloxy chain length (n). The plotted curve shows three distinct regions.

1. Crystalline phase (Cr): Observed below the melting temperature
2. Liquid crystalline phases (LC): Stable between melting and clearing temperature
3. Isotropic liquid phase (I): Present above the clearing temperature

The melting point is observed to increase with increasing alkyloxy chain length. This is due to stronger intermolecular Van der Waals forces within the molecular packing resulting from the extended alkyl chains (Ha *et al.*, 2009). In contrast, the clearing point shows a decreasing trend with increasing chain length, mainly because of the dilution effect on the core mesogenic group caused by the longer alkyloxy chains.

When the alkyloxy chain length increases, melting point of **BRLC<sub>n</sub>** increase while the clearing point decreases, resulting in a narrower temperature range for the mesogen phase. Among all the members, **BRLC12** possesses the widest liquid crystal temperature range. The wide liquid crystal region in

**BRLC12** is due to the ability of the dodecyloxy alkyl chain to balance the rigidity of the two aromatic cores within the molecule. The dodecyloxy alkyl chain improves molecular flexibility, which is effectively stabilized by the rigid aromatic core, making **BRLC12** the member with the widest liquid crystal temperature range at the alkyloxy chain. However, as the number of carbons increase from C14 (**BRLC14**) to C18 (**BRLC18**), the liquid crystal temperature range reduced due to the dilution effect on the mesogenic core system.

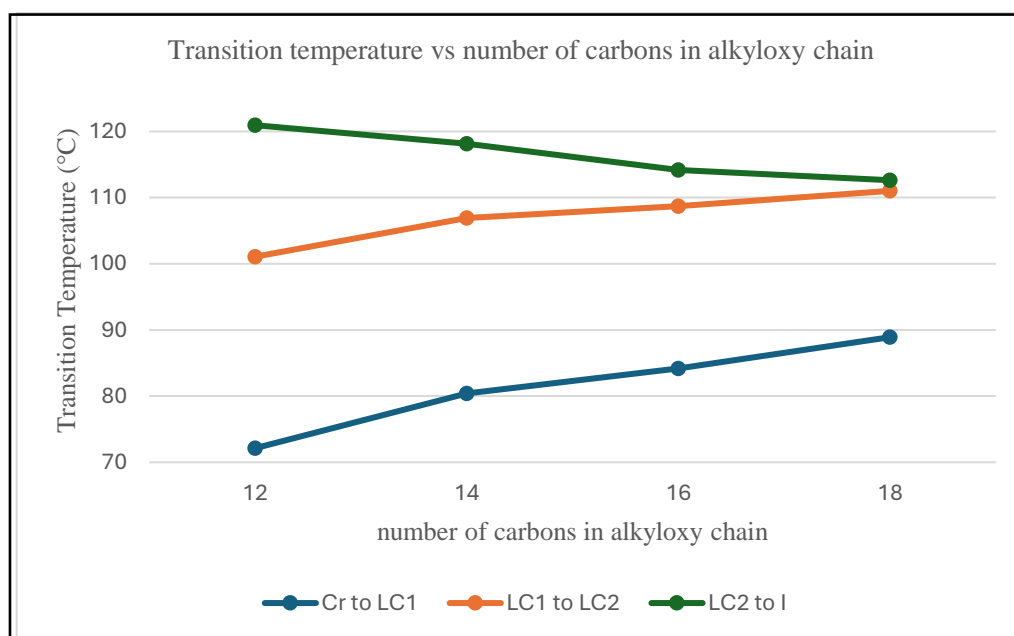


Figure 4.14: Plot of transition temperature against number of carbons in alkyloxy chain

#### 4.6 Photophysical Properties Analysis

The photophysical properties of **BMB1** and **BRLCn** compounds (where  $n = 12, 14, 16$ , and  $18$ ) were investigated using UV–Vis spectroscopy. For detailed discussion, **BRLC16** was selected as the representative compound. The spectral data obtained were compared with, and supported by, the findings of Alnoman *et al.* (2019). As shown in Figure 4.15, **BMB1** exhibited two absorption bands at 268 nm and 350 nm, while **BRLC16** showed peaks at 284 nm and 344 nm. A similar absorption pattern was observed across all **BRLCn** compounds.

When exposed to a light source within the wavelength range of 250–800 nm, electrons in the molecules absorb specific wavelengths of light, resulting in excitation. This absorption appears in the UV–Vis spectrum as peaks at  $\lambda_{\text{max}}$ . For excitation to occur, the energy absorbed must be equal to or greater than the energy gap ( $\Delta E$ ) between the highest occupied molecular orbital (HOMO) and the lowest unoccupied molecular orbital (LUMO). The wavelength at which absorption occurs is directly related to the energy by the Planck-Einstein equation:  $E = hc/\lambda$ .

As mentioned earlier, the UV–Vis absorbance spectrum of **BMB1** and **BRLC16** shows two main absorption peaks for each compound. The first peak, observed at 268 nm for **BMB1**, shifts to 284 nm for **BRLC16**, indicating a bathochromic shift (red shift). The shift is due to the presence of the alkyloxy

chain in **BRLC16**, which is bonded via an ether linkage. The electronegative oxygen atom in the ether enhances electron delocalization between the benzene ring and the ether group, resulting in increased resonance stabilization. This extended delocalization lowers the  $\Delta E$  (HOMO and LUMO energy gap), thus **BMB1** has shift to a longer wavelength in **BRLC16** (The Editors of Encyclopedia Britannica, 2018). The  $\lambda_{\text{max}}$  values at 268 nm for **BMB1** and 284 nm for **BRLC16**, both with higher intensities, are due to  $\pi \rightarrow \pi^*$  transitions between the benzene rings, facilitated by effective charge transfer (CT) properties in each compound of **BMB1** and **BRLCn** (Kara, Sidir, and Horoz, 2023). In benzene rings,  $\pi$  bonding molecular orbitals serve as the highest occupied molecular orbitals (HOMO), while  $\pi^*$  antibonding orbitals act as the lowest unoccupied molecular orbitals (LUMO). When energy is absorbed, electrons are excited from the HOMO to the LUMO which is also known as a  $\pi \rightarrow \pi^*$  transition. **BMB1** has the  $\pi \rightarrow \pi^*$  transitions at 268 nm while **BRLC16** at 284 nm.

The absorption maximum ( $\lambda_{\text{max}}$ ) was observed at 350 nm for **BMB1** and 344 nm for **BRLC16**, both appearing at lower intensities and due to  $n \rightarrow \pi^*$  transitions (Alnoman *et al.*, 2019). These transitions involve excitation from a non-bonding orbital (n), typically found on lone pairs of electrons (HOMO), to an antibonding  $\pi^*$  orbital (LUMO). In this case, the methoxy group  $-\text{OCH}_3$  which contains highly electronegative oxygen atoms had facilitates electron delocalization between the benzene ring and the methoxy group, enabling the  $n \rightarrow \pi$  transition. This group is also electron-donating, which can stabilize the system via resonance with the aromatic ring. The  $\lambda_{\text{max}}$  for **BMB1** is at 350 nm,

which is blue shifted (hypsochromic shift) to **BRLC16** at 344 nm, which is also referring to shifting to a shorter wavelength. This shift is due to the presence of the ether group in **BRLC16**. The lone pair electrons from the oxygen atom of the ether interact with the system, reducing the electron density in the non-bonding orbitals. As a result, the energy gap ( $\Delta E$ ) between the n and  $\pi^*$  orbitals increase, requiring higher energy (shorter wavelength) for the transition, hence the hypsochromic shift occurred.

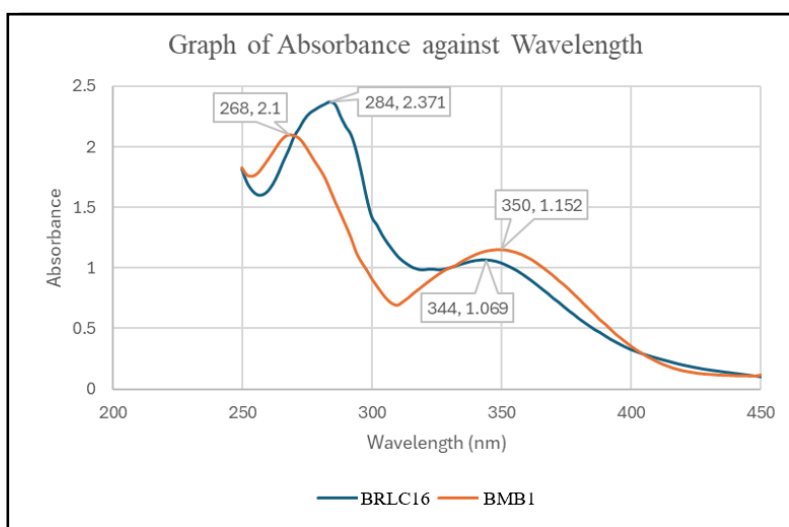


Figure 4.15: Graph of absorbance against wavelength between **BMB1** and **BRLC16**

In addition, the molar absorptivity values of the **BRLCn** series compounds were determined based on their measured absorbance. Molar absorptivity shows the ability of a compound to absorb light and undergo electronic transitions. Compounds with higher molar absorptivity are more likely to undergo such transitions compared to those with lower values. A compound with a high molar absorptivity is also effective at absorbing light at the stated



wavelength. The calculation of molar absorptivity was performed using the Beer–Lambert Law.

$$A = \varepsilon b c$$

where A = absorbance;  $\varepsilon$  = molar absorptivity ( $\text{mol L}^{-1} \text{ cm}^{-1}$ ); b = path length (cm); c = concentration ( $\text{mol L}^{-1}$ )

Standard calibration curves were drawn for each compound in the **BRLCn** series at 284 and 344 nm, with corresponding linear equations established as shown in Figure 4.16 and 4.17 (**BRLC16** as representative compound). All calibration plots exhibited an  $R^2$  value greater than 0.99, indicating a strong positive linear correlation between absorbance and concentration, this had further verified the reliability of the calibration curves. Assuming the linear relationship obeys the Beer–Lambert Law, the slope of each calibration curve represents the molar absorptivity ( $\varepsilon$ ) of the compound. The calculated molar absorptivity values for the **BRLCn** compounds at 284 nm and 344 nm are presented in Table 4.11.

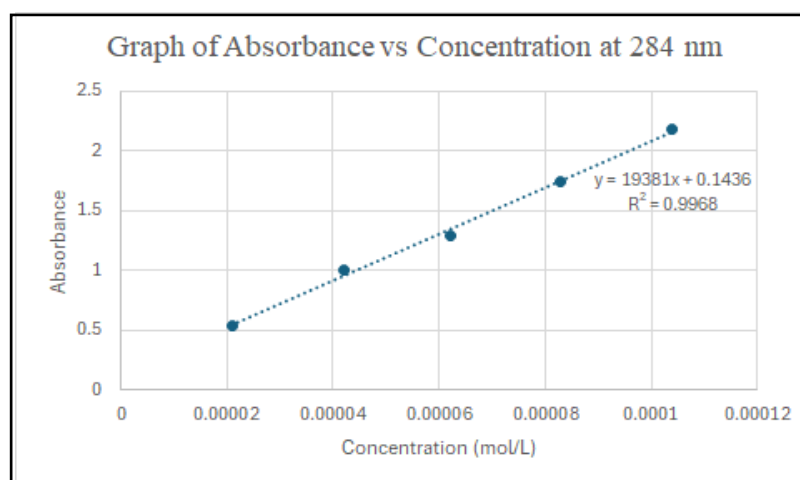


Figure 4.16: Graph of absorbance against concentration for **BRLC16** at 284 nm

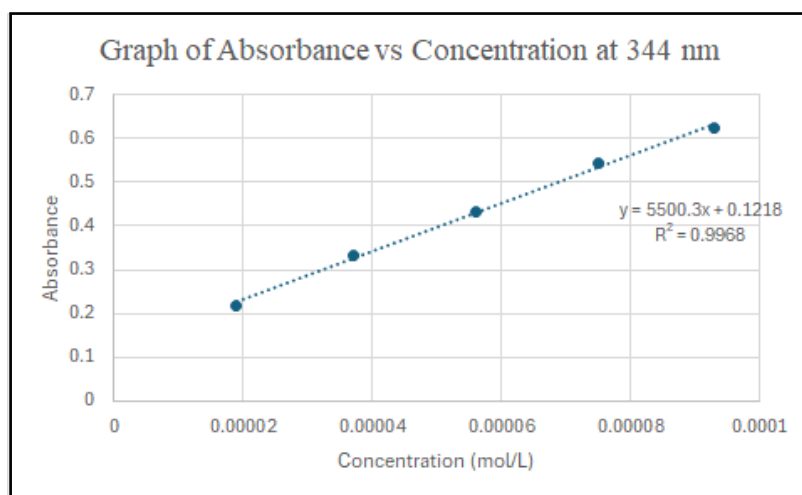


Figure 4.17: Graph of absorbance against concentration for **BRLC16** at 344nm

Table 4.11: Molar absorptivity values for the **BRLCn** compounds at 284 nm and 344 nm

Molar absorptivity (mol L <sup>-1</sup> cm <sup>-1</sup> )		
Sample	284 nm	344 nm
<b>BRLC12</b>	23632.0	5970.6
<b>BRLC14</b>	23247.0	5790.9
<b>BRLC16</b>	19381.0	5500.3
<b>BRLC18</b>	15811.0	4912.3

The presence of alkyloxy chains in conjugated organic compounds can influence their photophysical properties, especially the molar absorptivity. As the alkyloxy chain length increases, molar absorptivity tends to decrease. Longer alkyloxy chains are non-conjugated moieties, meaning they lack delocalized  $\pi$ -electrons and thus do not contribute to the chromophore of a molecule. When the length of these alkyloxy chains increases, they introduce greater steric

hindrance, which can distort the planarity of the conjugated system. Since planarity is important for effective  $\pi$ -electron delocalization and light absorption, any disruption reduces the efficiency of the electronic transitions involved. As a result, the molecule absorbs less light at a given concentration, leading to a lower molar absorptivity. Therefore, the increase in non-conjugated alkyloxy chain length reduce the ability of molecule to absorb light effectively, without contributing to its chromophoric properties. This phenomenon has been supported by Chapman, Henary and Patonay (2011), who reported that increasing the length of short-chain alkyl substituents results in a decrease in molar absorptivity in dye molecules.

## CHAPTER 5

### CONCLUSION

A series of benzothiazole ring with Schiff base linkage liquid crystals, specifically *(E)*-1-(4-(alkyloxy)phenyl)-*N*-(6-methoxybenzo[d]thiazol-2-yl)methanimine (denoted as **BRLC<sub>n</sub>**, where *n* refers to the number of carbon atoms in the alkyloxy chain, C<sub>n</sub>H<sub>2n+1</sub>O-, with *n* = 12, 14, 16, and 18), were successfully synthesized. The molecular structures of these synthesized compounds were fully characterized through comprehensive spectroscopic analysis including Fourier Transform (FTIR), one-dimensional NMR spectroscopy (<sup>1</sup>H and <sup>13</sup>C), and two-dimensional NMR techniques including COSY, HMBC, and HMQC. The synthesized compounds are as follows:

*(E)*-1-(4-(dodecyloxy)phenyl)-*N*-(6-methoxybenzo[d]thiazol-2-yl)methanimine, **BRLC12**

*(E)*-1-(4-(tetradecyloxy)phenyl)-*N*-(6-methoxybenzo[d]thiazol-2-yl)methanimine, **BRLC14**

*(E)*-1-(4-(hexadecyloxy)phenyl)-*N*-(6-methoxybenzo[d]thiazol-2-yl)methanimine, **BRLC16**

*(E)*-1-(4-(octadecyloxy)phenyl)-*N*-(6-methoxybenzo[d]thiazol-2-yl)methanimine, **BRLC18**

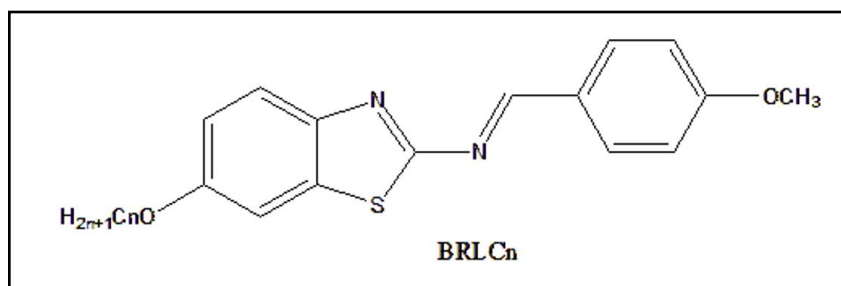
Infrared spectral analysis of the **BRLCn** compounds confirmed the presence of key functional groups, including the Schiff base linkage (HC=N), ether (C-O) and aliphatic chain. Additionally, using **BRLC16** as a representative compound, the predicted structures of the **BRLCn** series were successfully elucidated through NMR spectroscopy. In  $^1\text{H}$  NMR, the signal appeared at  $\delta$  8.88, indicated the Schiff base condensation was accomplished. In  $^{13}\text{C}$  NMR, the carbon signals for Schiff base ( $\delta$  164.5, HC=N), ether ( $\delta$  68.5, C-O), aliphatic chain ( $\delta$  14.2 – 55.9, CH), aromatic ( $\delta$  104.6 – 163.5, C=C), as well as the carbon signal for quaternary carbon bonded with benzothiazole ring ( $\delta$  169.9) were successfully assigned.

In addition, all synthesized compounds were found to exhibit liquid crystal phase based on the DSC results. The DSC thermogram for **BRLC16** shows three peaks in both heating and cooling cycle indicated the phase transition. In heating cycle, large peak for the phase transition Cr  $\rightarrow$  LC1 at the transition temperature 86.06  $^{\circ}\text{C}$  (48.02 kJ mol $^{-1}$ ) and first small peak for transition of LC1  $\rightarrow$  LC2 at transition temperature 109.47  $^{\circ}\text{C}$  (0.50 kJ mol $^{-1}$ ). Second small peak indicates LC2  $\rightarrow$  I which occur at 114.86  $^{\circ}\text{C}$  (1.18 kJ mol $^{-1}$ ). In cooling cycle, small peak for phase transition I  $\rightarrow$  LC1 at 113.53  $^{\circ}\text{C}$  (1.03 kJ mol $^{-1}$ ) and second small peak LC2  $\rightarrow$  LC1 at 108.17  $^{\circ}\text{C}$  (0.85 kJ mol $^{-1}$ ). Finally, the peak for LC1  $\rightarrow$  Cr at 60.48  $^{\circ}\text{C}$  (40.23 kJ mol $^{-1}$ ). During the heating cycle, an endothermic process occurred as energy was absorbed to overcome the intermolecular attractive forces within the molecules. In contrast, during the cooling cycle, an exothermic process took place as the molecules released energy to facilitate molecular packing.

The photophysical properties of the **BRLCn** series were analysed using UV–Vis spectroscopy. All compounds exhibited two absorption maxima—one at 284 nm and another at 350 nm—within the scanning range of 200–800 nm. The 284 nm peak corresponds to  $\pi \rightarrow \pi^*$  transitions between the two benzene rings, while the 350 nm peak is attributed to  $n \rightarrow \pi^*$  transitions. Additionally, the molar absorptivity of the **BRLCn** compounds was determined, and it was found that as the alkyloxy chain length increased, the molar absorptivity decreased, indicating that compounds with longer alkyloxy chains have a lower light absorption capability.

### Further study

In future studies, the mesophase types exhibited by the **BRLCn** series can be identified using polarized optical microscopy (POM), along with an investigation of their photoluminescent properties. Furthermore, orientation of the ether linking group can be swapped with methoxy group, then further examine the impact of this inversion on their mesomorphic behaviour.



## REFERENCES

### Journal

Alnoman, R., Al-Nazawi, F.K., Ahmed, H.A. and Hagar, M. (2019) ‘Synthesis, Optical, and Geometrical Approaches of New Natural Fatty Acids’ Esters/Schiff Base Liquid Crystals’, *Molecules*, 24(3), pp. 4293–4315.

An, J.-G., Hina, S., Yang, Y., Xue, M. and Liu, Y. (2016) ‘Characterization of Liquid Crystals: A Literature Review’, *Review of Advanced Materials Science*, [online] pp. 398–399. Available at: [https://www.ipme.ru/e-journals/RAMS/no\\_44416/06\\_44416\\_an.pdf](https://www.ipme.ru/e-journals/RAMS/no_44416/06_44416_an.pdf) (Accessed: 30 June 2024).

Babij, N.R., McCusker, E.O., Whiteker, G.T., Canturk, B., Choy, N., Creemer, L.C., De Amicis, C., Hewlett, N.M., Johnson, P.L., Knobelsdorf, J.A., Li, F., Lorsbach, B.A., Nugent, B.M., Ryan, S.J., Smith, M.R. and Yang, Q. (2016) ‘NMR Chemical Shifts of Trace Impurities: Industrially Preferred Solvents Used in Process and Green Chemistry’, *Organic Process Research & Development*, 20(3), pp. 661–667.

Chapman, G., Henary, M. and Patonay, G. (2011) 'The effect of varying short-chain alkyl substitution on the molar absorptivity and quantum yield of cyanine dyes', *Analytical Chemistry Insights*, 6, pp. 29–36. Available at: <https://doi.org/10.4137/aci.s6568>.

Chen, J. (2023) 'Current advances in anisotropic structures for enhanced osteogenesis', *Colloids and Surfaces B: Biointerfaces*, 231, pp.113566–113566. Available at: <https://doi.org/10.1016/j.colsurfb.2023.113566>.

Fornasieri, G., Guittard, F. and G ribaldi, S. (2003) 'Influence of the structure of the mesogenic core on the thermotropic properties of  $\omega$ -unsaturated fluorinated liquid crystals', *Liquid Crystals*, 30(2), pp. 251–257. Available at: <https://doi.org/10.1080/0267829031000065155>.

Ha, S.T., Koh, T.M., Yeap, G.Y., Lin, H.C., Boey, P.L., Win, Y.F., Ong, S.T. and Ong, L.K. (2009) 'Synthesis and Mesomorphic Properties of 2-(4-Alkyloxyphenyl)benzothiazoles', *Molecular Crystals and Liquid Crystals*, 506(1), pp. 56–70.

Ha, S.T., Ong, L.K., Sivasothy, Y. and Yeap, G.Y. (2010a) 'Mesogenic Schiff base esters with terminal chloro group: Synthesis, thermotropic properties and X-ray', *International Journal of the Physical Sciences*, 5(5), pp. 570–572.



Ha, S.T., Koh, T.M., Yeap, G.Y., Lin, H.C., Lee, S.L., Win, Y.F. and Ong, S.T. (2010b) 'Synthesis and Mesomorphic Properties of 6-Methoxy- and 6-Ethoxy-2-(2-Hydroxy-4-Alkanoyloxybenzylidenamino)Benzothiazoles', *Molecular Crystals and Liquid Crystals*, 528(1), pp. 10–22. Available at: <https://doi.org/10.1080/15421406.2010.504510>.

Ha, S.T., Ng, M.Y., Subramaniam, R.T. and Ito, M.M. (2010c) 'Mesogenic azomethine esters with different end groups: Synthesis and thermotropic properties', *International Journal of the Physical Sciences*, 5(8), pp. 1257–1260.

Hagar, M., Ahmed, H.A., Nafee, S.S., El-Shishtawy, R.M. and Raffah, B.M. (2019) 'The Synthesis of New Thermal Stable Schiff Base/Ester Liquid Crystals: A Computational, Mesomorphic, and Optical Study', *Molecules*, 24(17), pp.3032–3032. Available at: <https://doi.org/10.3390/molecules24173032>.

Hossain, M.S., Pijush, K.R., Zakaria, C. and Zahan, M.K.E. (2018) 'Selected Schiff base coordination complexes and their microbial application: A review', *International Journal of Chemical Studies*, 6(1), pp. 19–31.

Hussain, A., Pina, A.S. and Roque, A.C.A. (2009) 'Bio-recognition and detection using liquid crystals', *Biosensors and Bioelectronics*, 25(1), pp. 1–8. Available at: <https://doi.org/10.1016/j.bios.2009.04.038>.

Jber, N.R., Shukur, M.M. and Najaf, A.A. (2017) 'Schiff Base Liquid Crystals with Terminal Alkoxy Group Synthesis and Thermotropic Properties', *Journal of AlNahrain University Science*, 17(2), pp. 64–72.

Kara, Y.E., Sidir, Y.G. and Horoz, S. (2023) 'The Solvent Effect on Nanomaterials Composed of Liquid Crystals and Nanoparticles: UV-Vis Absorbance and Fluorescence Spectra', *Turkish Journal of Science and Technology*, 18(2), pp. 477–486. Available at: <https://doi.org/10.55525/tjst.1320988>.

Karuna, S.A. and Laxmi, S.A. (2015) 'Applications of Liquid Crystals: Special Emphasis on Liquid Crystal Displays (LCDs)', *Journal of Emerging Technologies and Innovative Research*, 2(4), pp. 1985–1986. Available at: <https://www.jetir.org/papers/JETIR1701696.pdf> (Accessed: 30 April 2025).

Lee, W.N., Salleh, N.M. and Cheng, S.F. (2021) 'Synthesis and characterization of new Schiff base ester liquid crystals with fatty acids from palm oil as flexible alkyl chain', *Industrial Crops and Products*, 170, pp. 2–5. Available at: <https://doi.org/10.1016/j.indcrop.2021.113808>.

Ossowska-Chrusciel, M.D., Chrusciel, J., Zalewski, S., Rudzki, A., Filiks, A. and Przedmojski, J. (2004) 'Influence of Length of Alkyl Terminal Chain on Mesomorphic Properties of New Chiral Liquid Crystalline Homologous Series of Thiobenzoates', *SPIE Proceedings*, 5565, pp. 94–97. Available at: <https://doi.org/10.1117/12.581074>.

Ong, L.K. and Ha, S.T. (2013) 'Influence of Linking Group Orientation on Mesomorphism of Two Aromatic Ring Mesogens', *Journal of Chemistry*, 2013(1), pp. 1–4. Available at: <https://doi.org/10.1155/2013/864819>.

Pfletscher, M., Mezger, M. and Giese, M. (2018) 'On the impact of linking groups in hydrogen-bonded liquid crystals – a case study', *Soft Matter*, 14(30), pp. 6214–6221. Available at: <https://doi.org/10.1039/c8sm00802g>.

Raczuk, E., Dmochowska, B., Samaszko-Fiertek, J. and Madaj, J. (2022) 'Different Schiff bases—structure, importance and classification', *Molecules*, 27(3), p. 787. Available at: <https://doi.org/10.3390/molecules27030787>.

Sani, U., Na'ibi, H.U. and Dailami, S.A. (2018) 'In vitro antimicrobial and antioxidant studies on N-(2-hydroxybenzylidene) pyridine-2-amine and its M(II) complexes', *Nigerian Journal of Basic and Applied Sciences*, 25(1), p. 81. Available at: <https://doi.org/10.4314/njbas.v25i1.11>.

Sardon, S.N.F., Rahman, N.M.M.A., Karim, M.R., Zahid, N.I. and Salleh, N.M. (2021) 'Effects of lateral methyl and terminal substituents on thermal, mesomorphic and optical properties of azo-ester mesogens', *Journal of Molecular Structure*, 1225, p.129112. Available at: <https://doi.org/10.1016/j.molstruc.2020.129112>.

Seou, C.K., Ha, S.T., Win, Y.F., Lee, S.L. and Yeap, G.Y. (2014) 'Synthesis and phase transition behaviours of new non-symmetric liquid crystal dimers', *Liquid Crystals*, 41(11), pp. 1627–1634. Available at: <https://doi.org/10.1080/02678292.2014.938373>.

Soni, S., Bishnoi, D.D., Soni, S. and Ramswroop (2013) 'Liquid Crystals and Applications of Cholesteric Liquid Crystal in Laser', *International Journal of Modern Physics: Conference Series*, 22, pp. 736–740. Available at: <https://doi.org/10.1142/s2010194513010957>.

Shoop, B.L., Sayles, A.H. and Litynski, D.M. (2002) 'New Devices for Optoelectronics: Smart Pixels', *Elsevier eBooks*, pp. 352–354. Available at: <https://doi.org/10.1016/b978-012207892-7/50011-4>.

Subasi, T.N. (2022) 'Overview of Schiff Bases', *Schiff Base in Organic, Inorganic and Physical Chemistry*. Available at: <https://doi.org/10.5772/intechopen.108178>.

Woliński, T.R., Ertman, S. and Rutkowska, K.A. (2015) 'Liquid crystals infiltrated photonic crystal fibers (PCFs) for electromagnetic field sensing', *Elsevier eBooks*, pp. 182. Available at: <https://doi.org/10.1016/b978-1-78242-329-4.00007-2>.

### **Book**

Bruce, D.W. (2007) *Comprehensive Organometallic Chemistry III*. Available at: <https://download.e-bookshelf.de/download/0000/6032/21/L-G-0000603221-0002288724.pdf> (Accessed: 9 May 2024).

Collings, P.J. and Hird, M. (1998) *Introduction to Liquid Crystals: Chemistry and Physics*. London: Taylor and Francis.

Collings, PJ & Hird, M. (2017). *Introduction to Liquid Crystals Chemistry and Physics*, CRC Press, Taylor & Francis e-Library, pp. 1–15.

DiLisi, G.A. (2019) *An Introduction to Liquid Crystals*. San Rafael [California]: Morgan & Claypool Publishers.

Dierking, I. (2003) *Texture of Liquid Crystals*. United Kingdom: Wiley-Vch Verlag.

Khoo, I.-C. (2007) *Liquid Crystals*. 2nd ed. Chichester: John Wiley & Sons.

Khoo, I.-C. (2022) *Liquid Crystals*, 3rd ed. Hoboken: John Wiley & Sons

Kumar, S. and Kang, S-W. (2005) *Encyclopedia of Condensed Matter Physics*, 2nd ed. Amsterdam: Elsevier

Ouellette, R.J. and Rawn, J.D. (2015) *Organic Chemistry Study Guide*. Available at: <https://doi.org/10.1016/b978-0-12-801889-7.00016-9> (Accessed: 9 May 2025).

Singh, S. and Dunmur, D.A. (2002) *Liquid Crystals: Fundamentals*. Danvers: World Scientific Publishing Co. Pte. Ltd.

## Website

Ashenhurst, J. (2025) *The Williamson Ether Synthesis*. Available at: <https://www.masterorganicchemistry.com/2014/10/24/the-williamson-ether-synthesis/> (Accessed: 11 May 2025).

Agamanolis, S. (2018) *Liquid Crystal*. Available at: <https://web.media.mit.edu/~stefan/liquid-crystals/node2.html> (Accessed: 19 April 2025).

Concept Group LLC (2011) *What is phase change? | Explained by Thermal Engineers*. Available at: <https://conceptgroupllc.com/glossary/what-is-phase-change/> (Accessed: 19 April 2025).

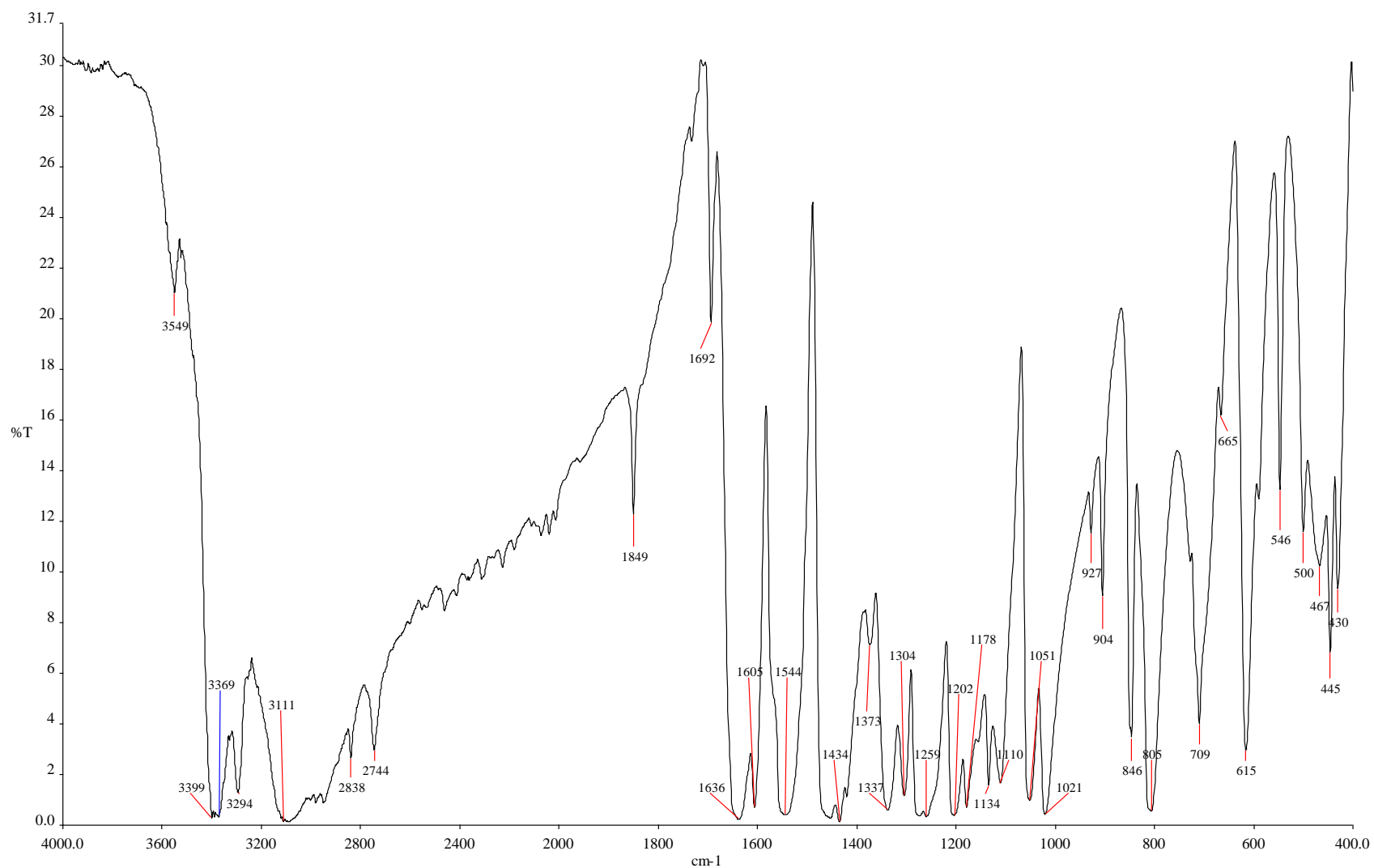
PCMag (1996) *Definition of liquid crystal*. Available at: <https://www.pcmag.com/encyclopedia/term/liquid-crystal> (Accessed: 26 June 2024).

Smartglass World (2023) *Liquid Crystal Thermometers*. Available at: <https://www.smartglassworld.net/liquid-crystal-thermometers> (Accessed: 30 June 2024).

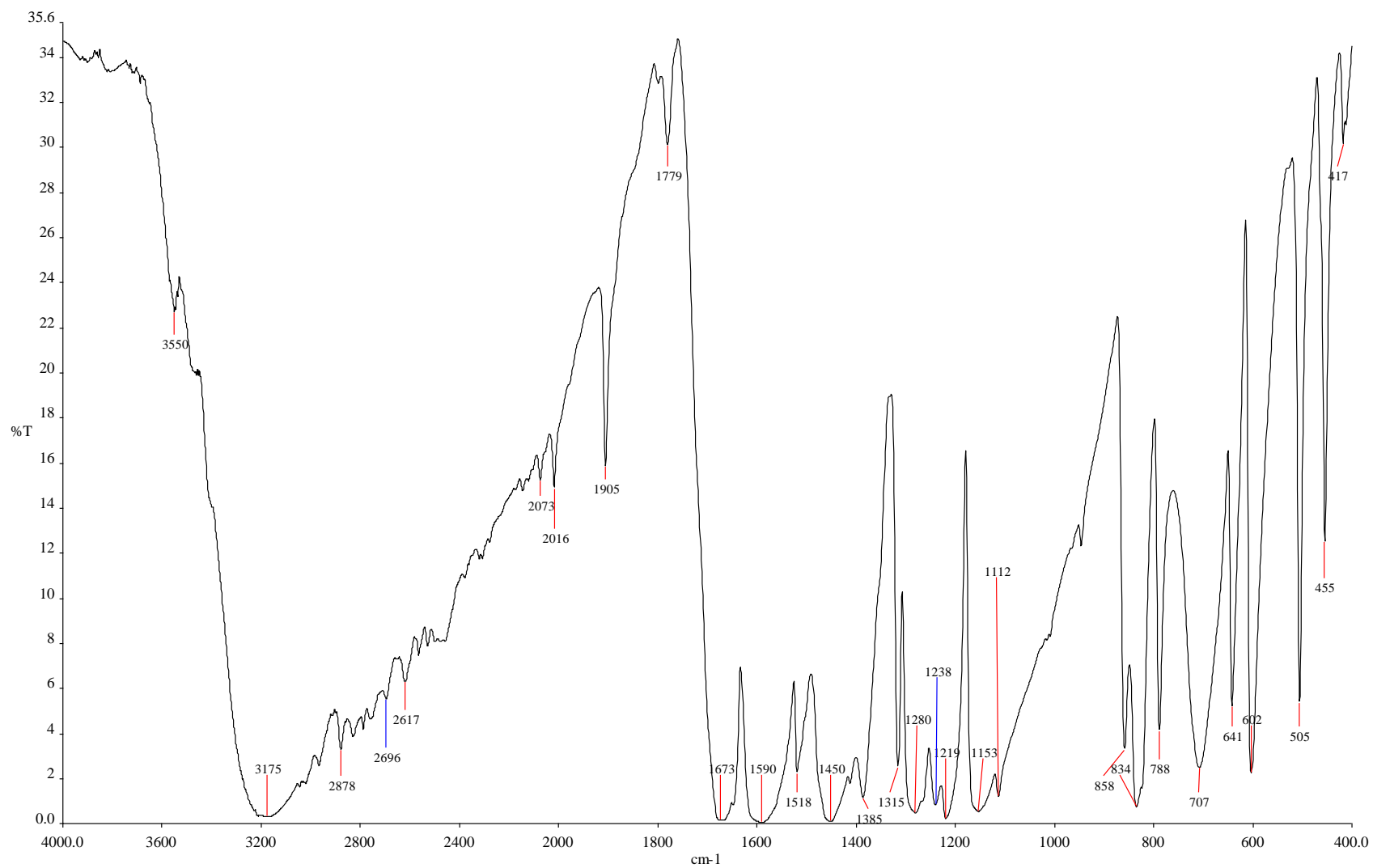
The Editors of Encyclopædia Britannica (2018) *Redshift* | *astronomy*.  
*Encyclopædia Britannica*. Available at:  
<https://www.britannica.com/science/redshift> (Accessed: 13 April 2025).

University of Houston (no date) *Introduction to Liquid Crystals*. Available at:  
<https://uh.edu/~chembi/liquidcrystals.pdf> (Accessed: 26 June 2024).

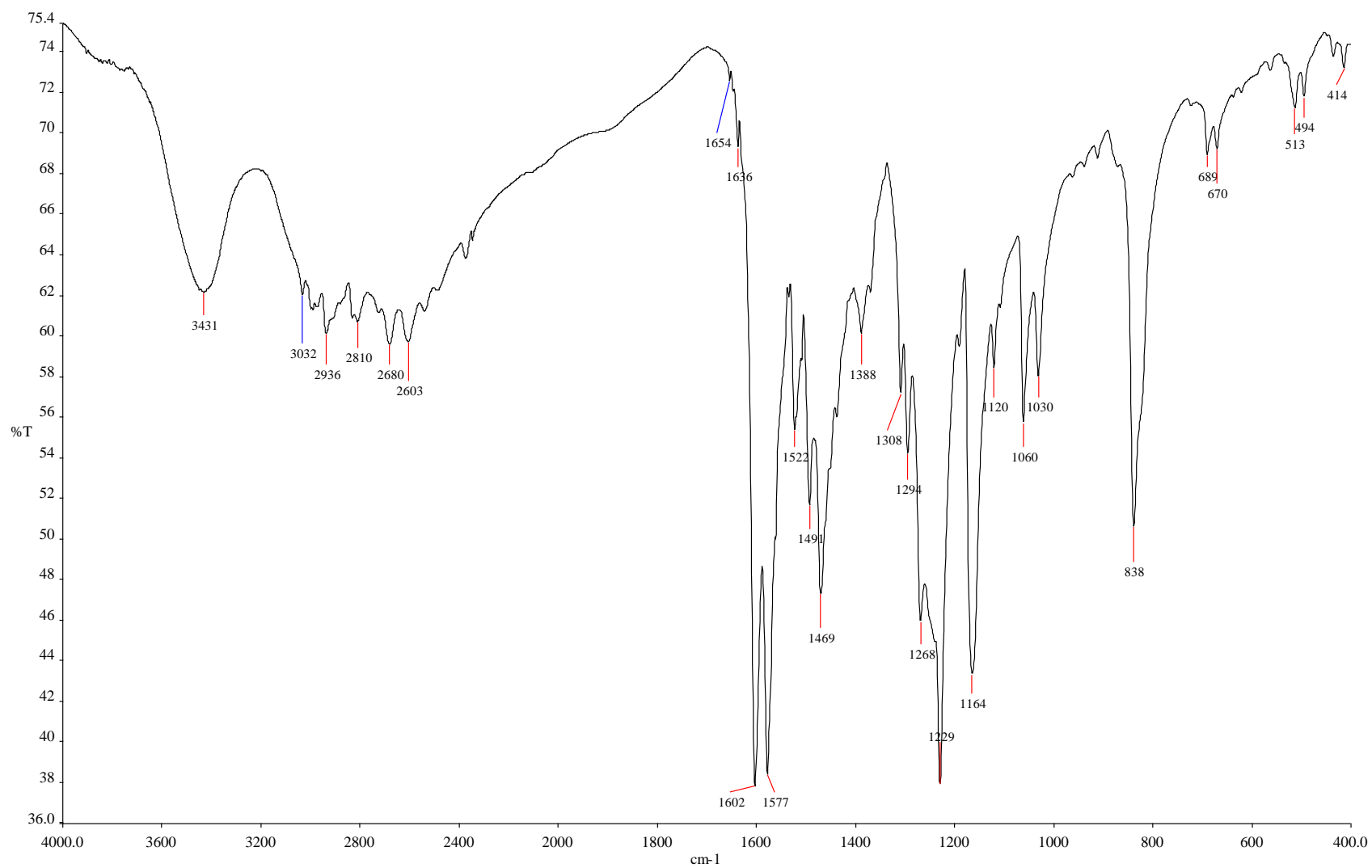




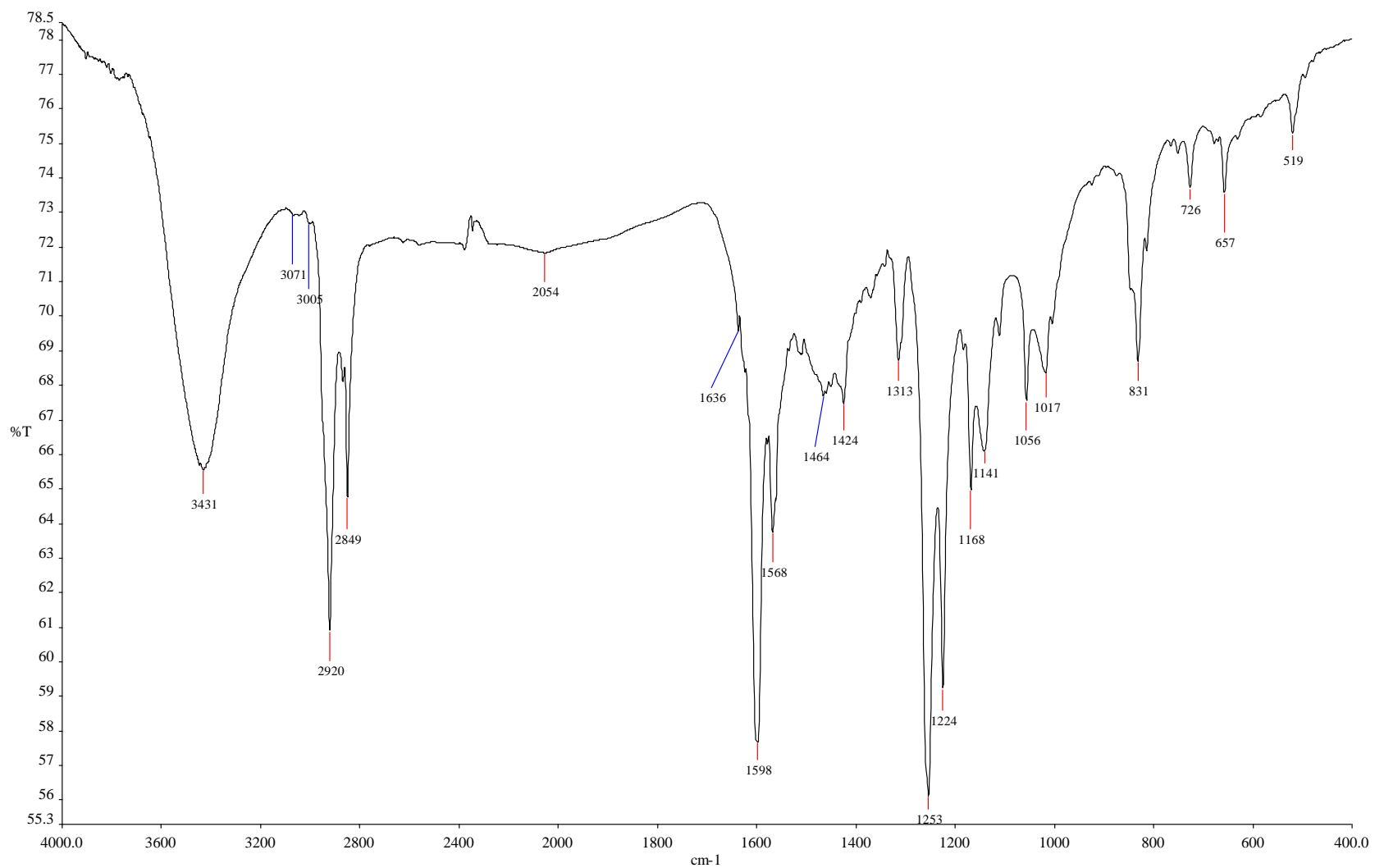
A1 FTIR Spectrum of 2-amino-6-methoxybenzothiazole



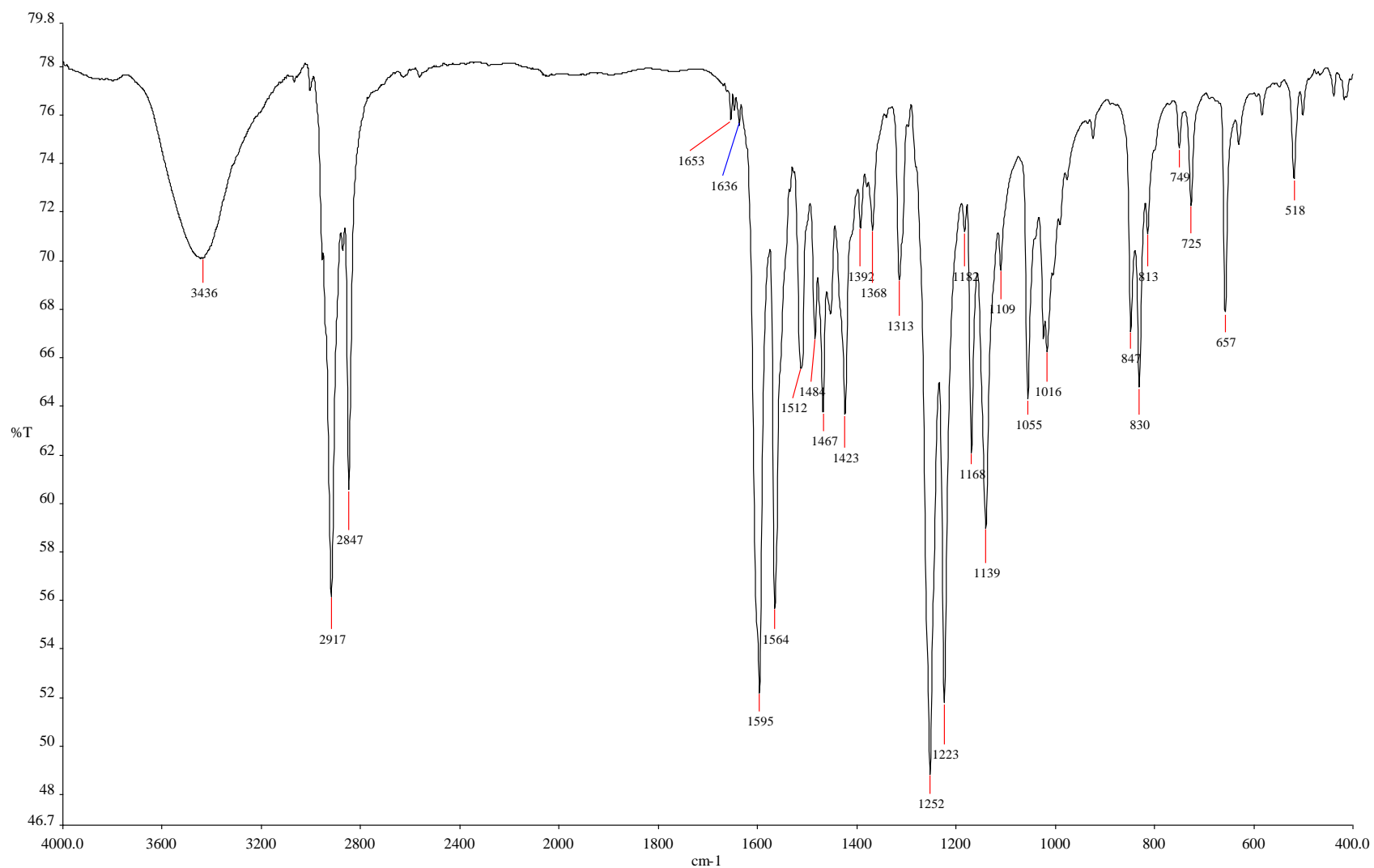
A2 FTIR Spectrum of 4-hydroxybenzaldehyde



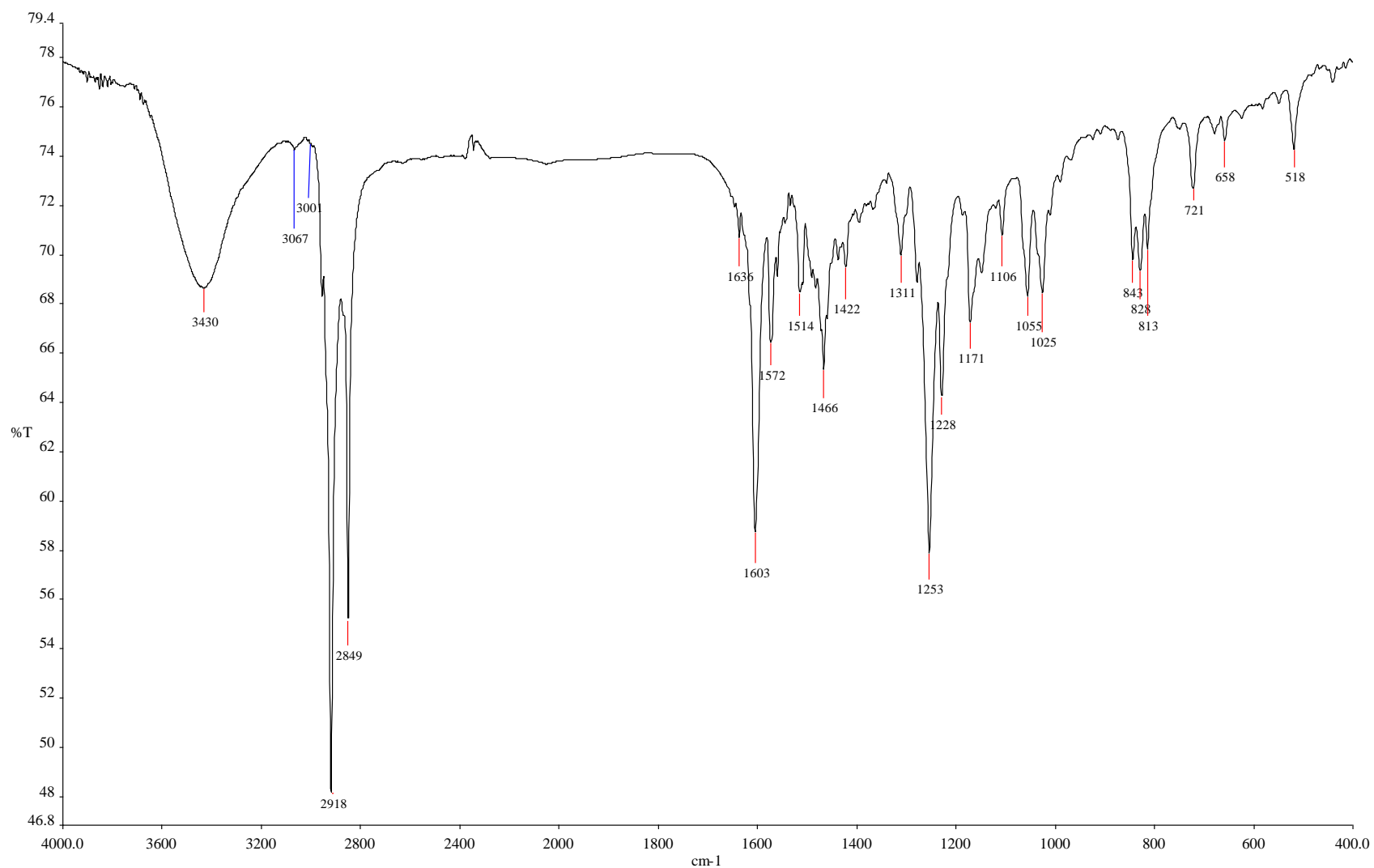
A3 FTIR Spectrum of **BMB1**



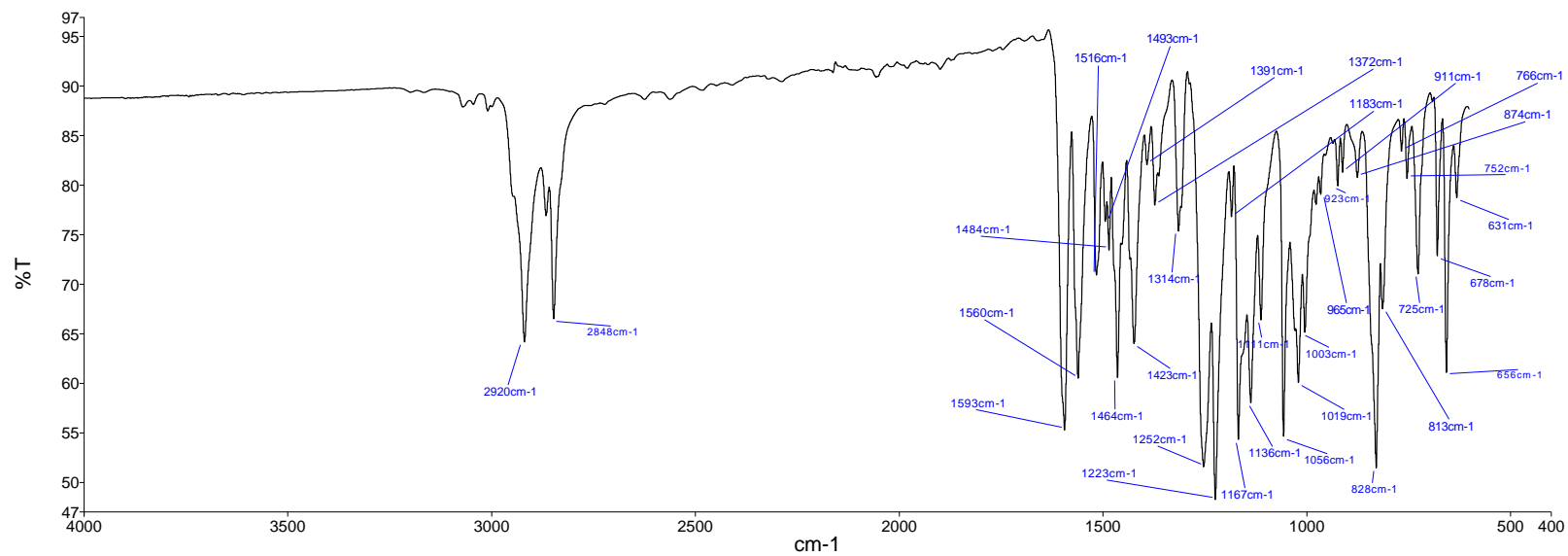
A4 FTIR Spectrum of **BRLC12**



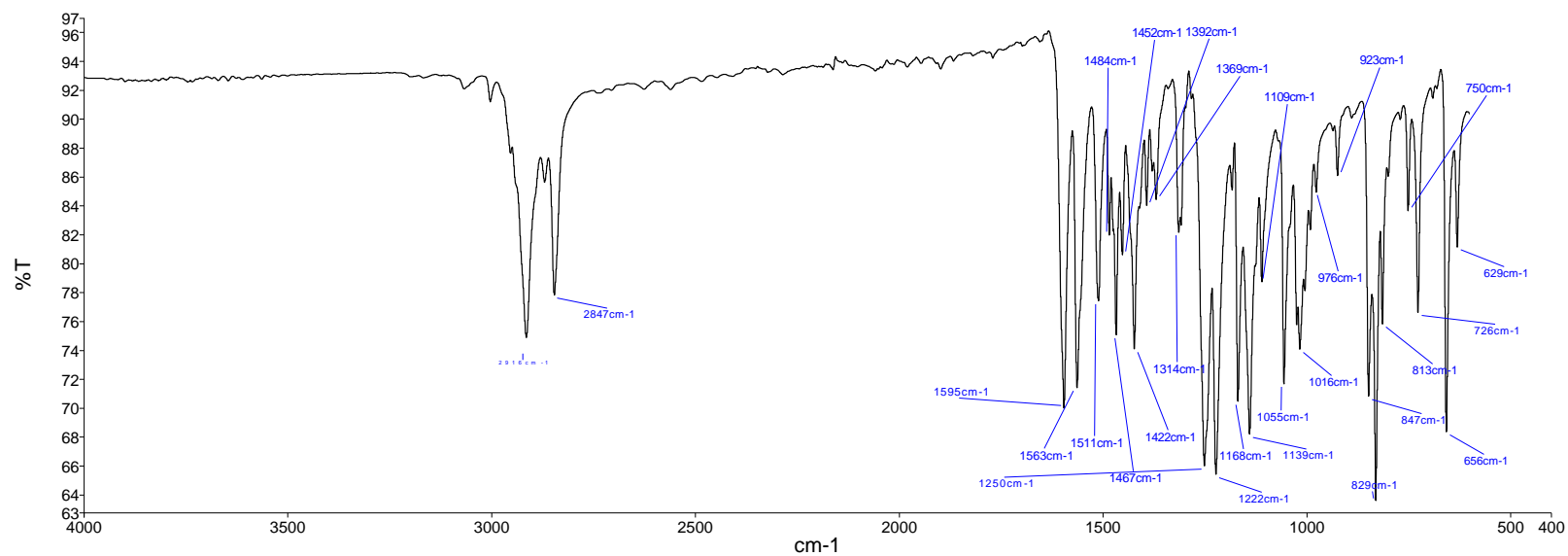
A5 FTIR Spectrum of **BRLC14**



A6 FTIR Spectrum of **BRLC18**

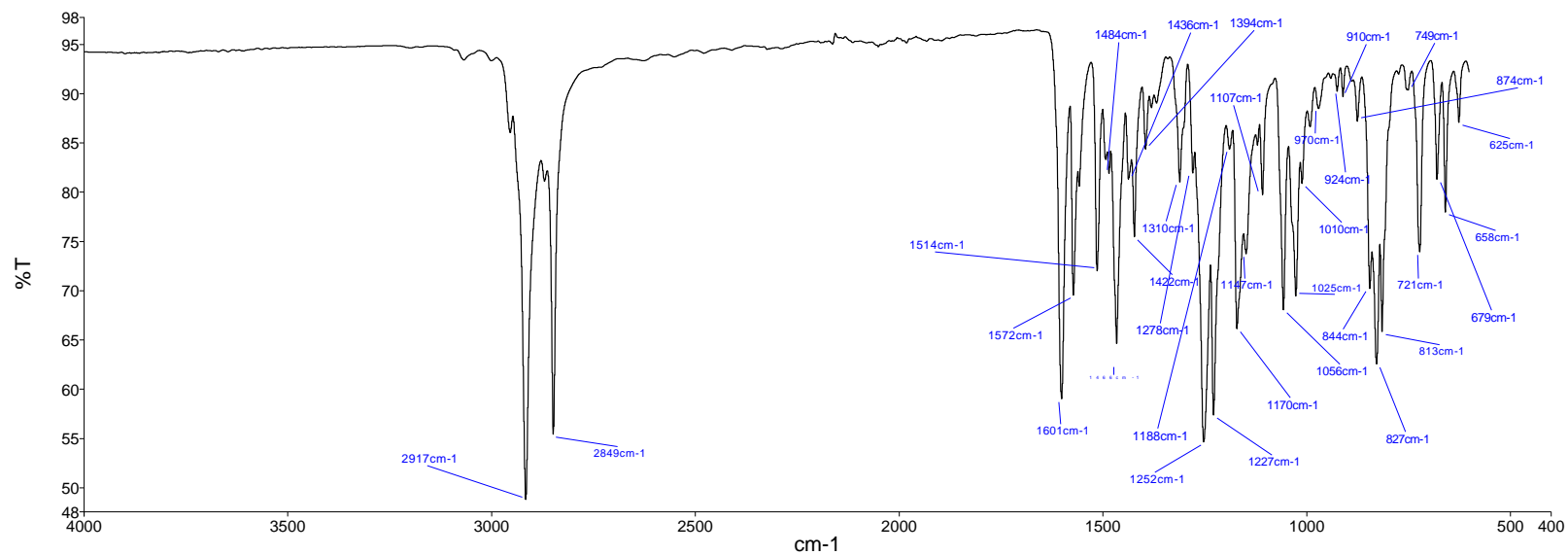


A7 ATR Spectrum of **BRLC12**

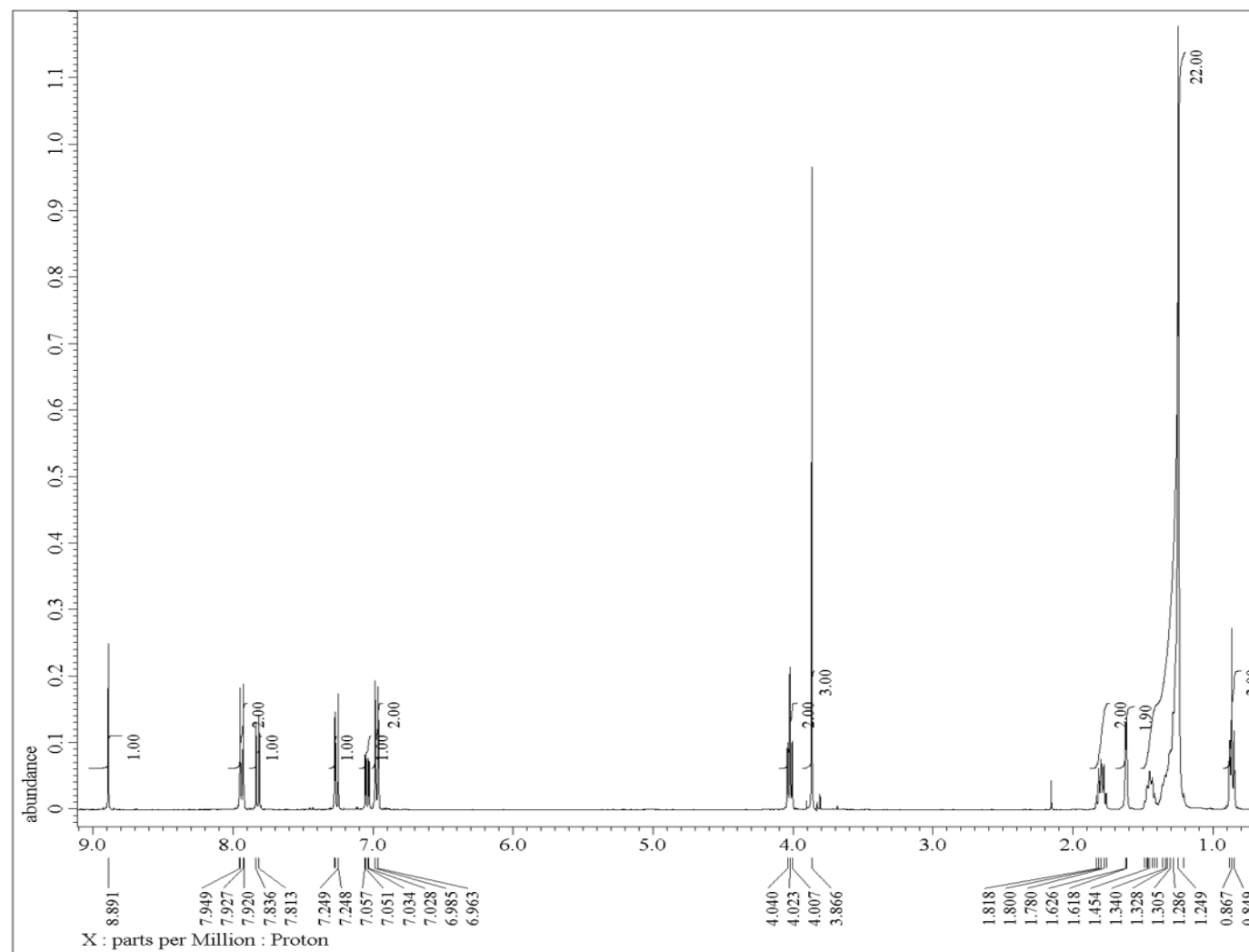


A8 ATR Spectrum of **BRLC14**

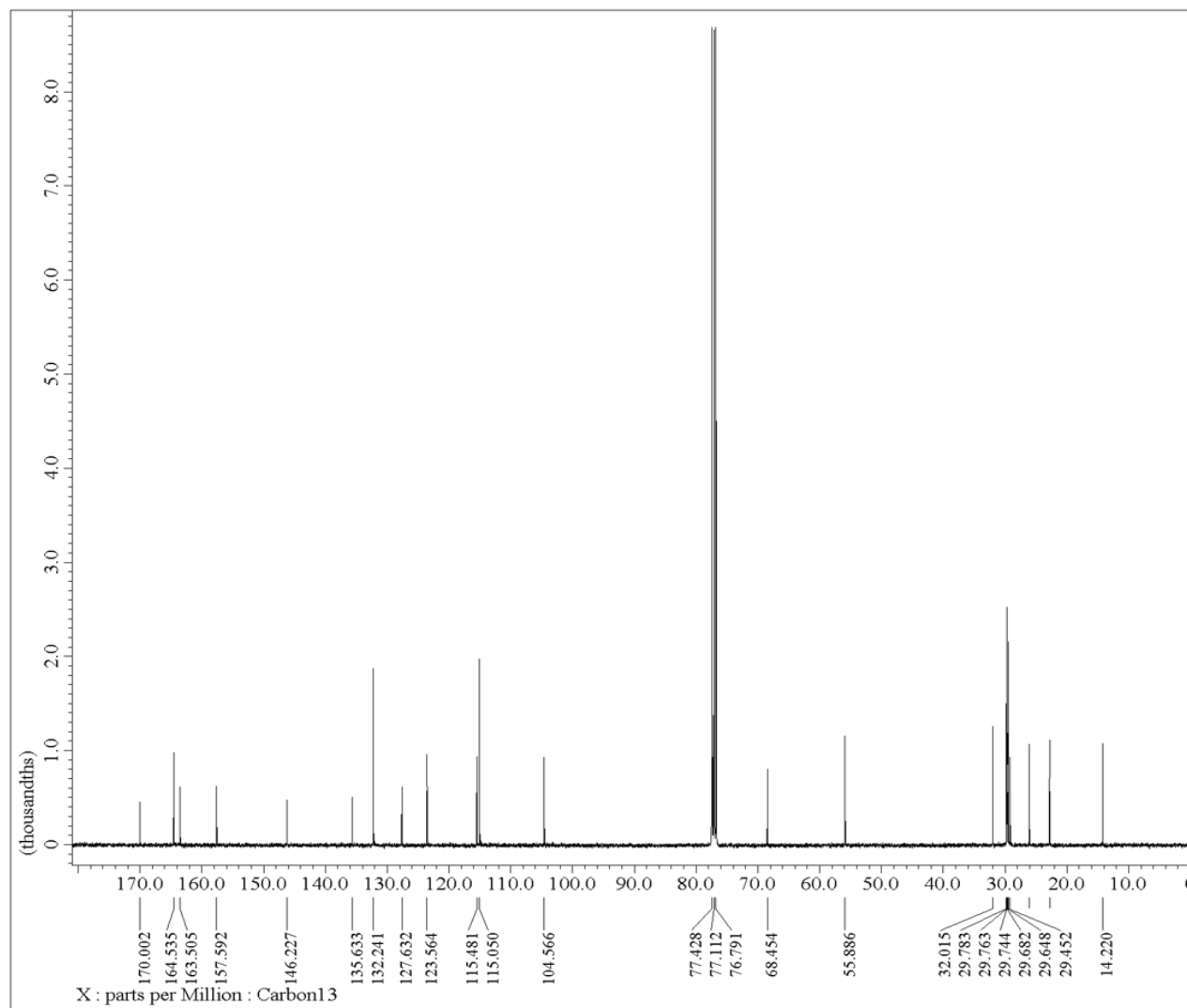




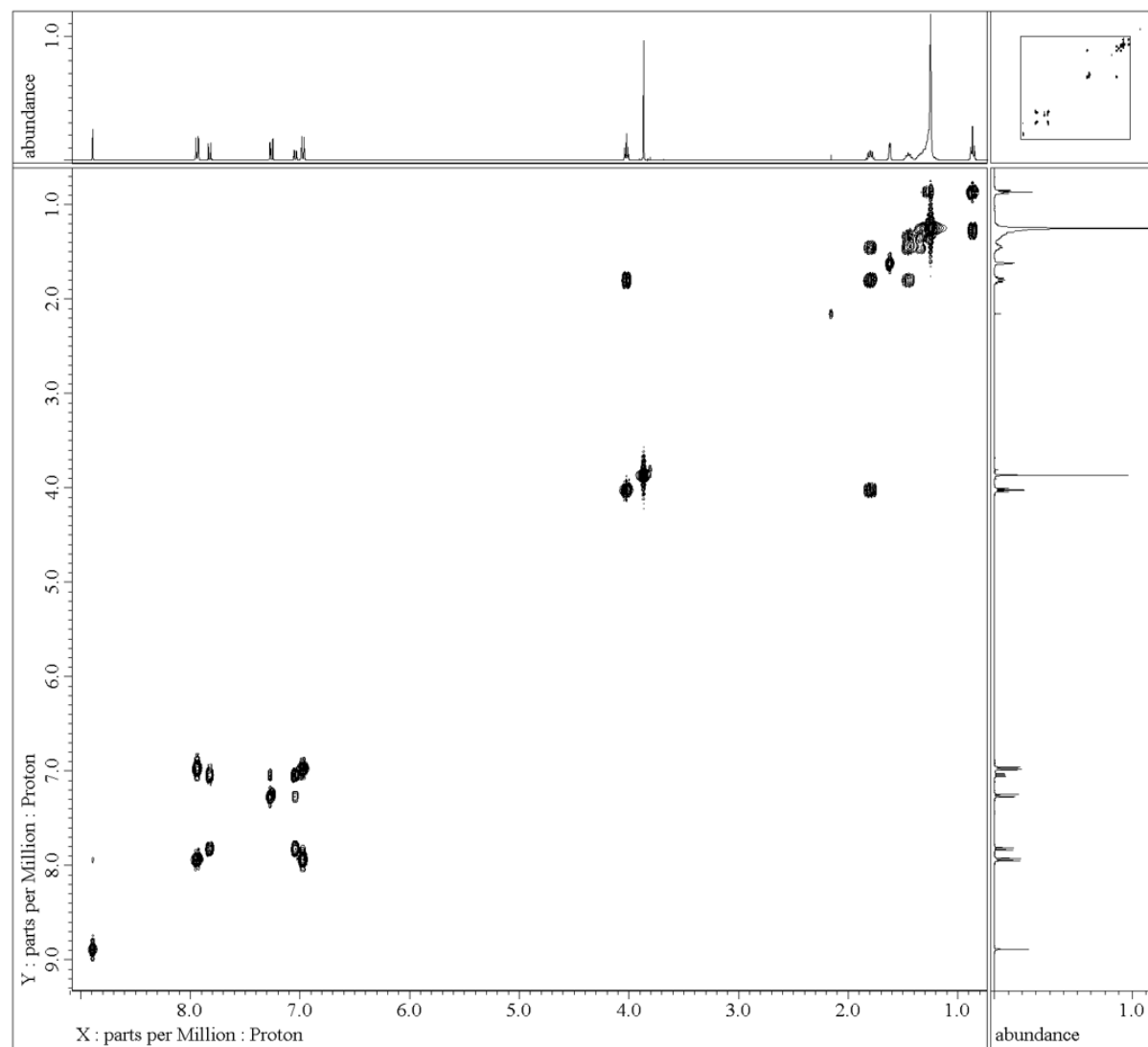
A9 ATR Spectrum of **BRLC18**



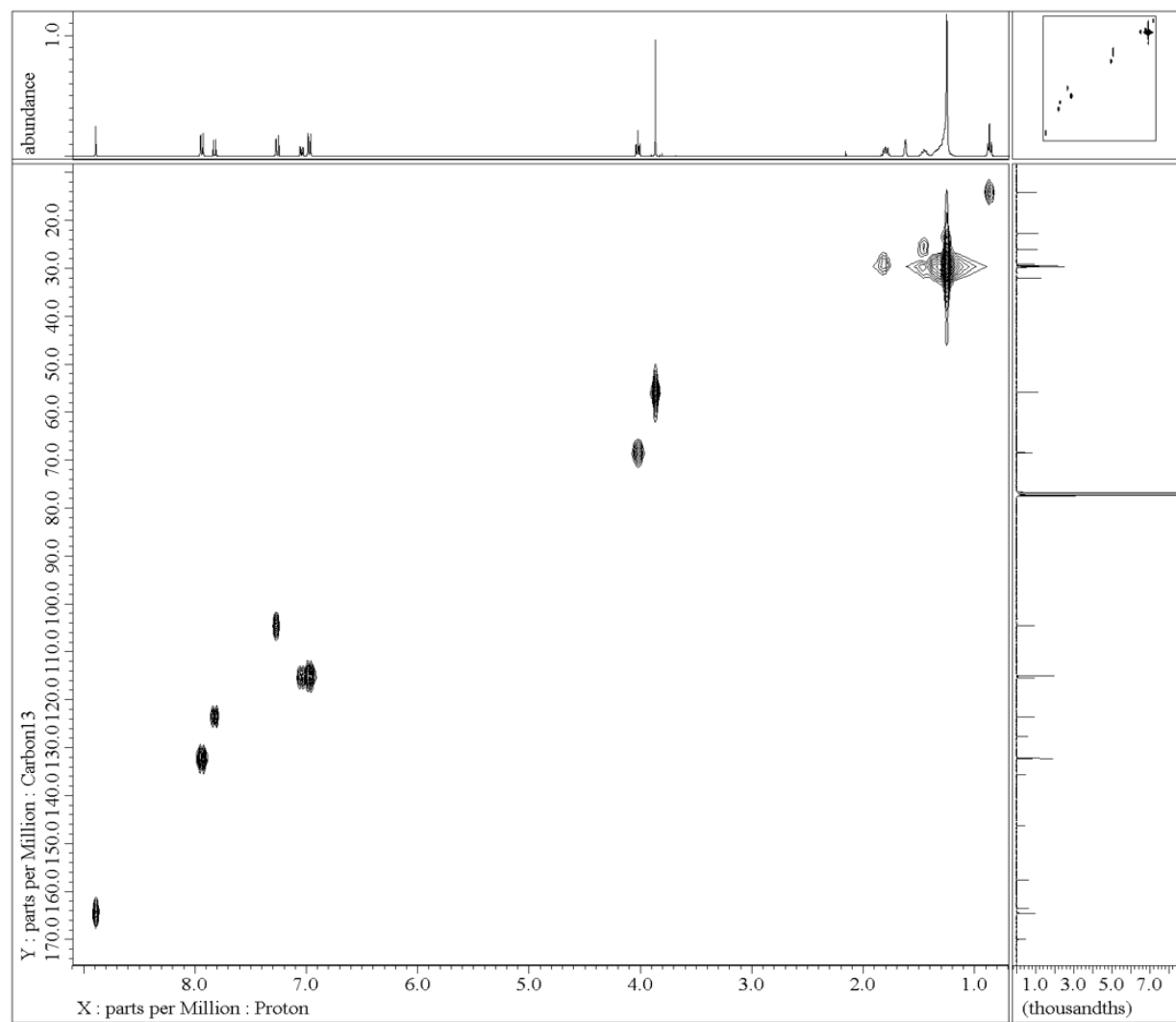
A10  $^1\text{H}$  NMR Spectrum of **BRLC14**



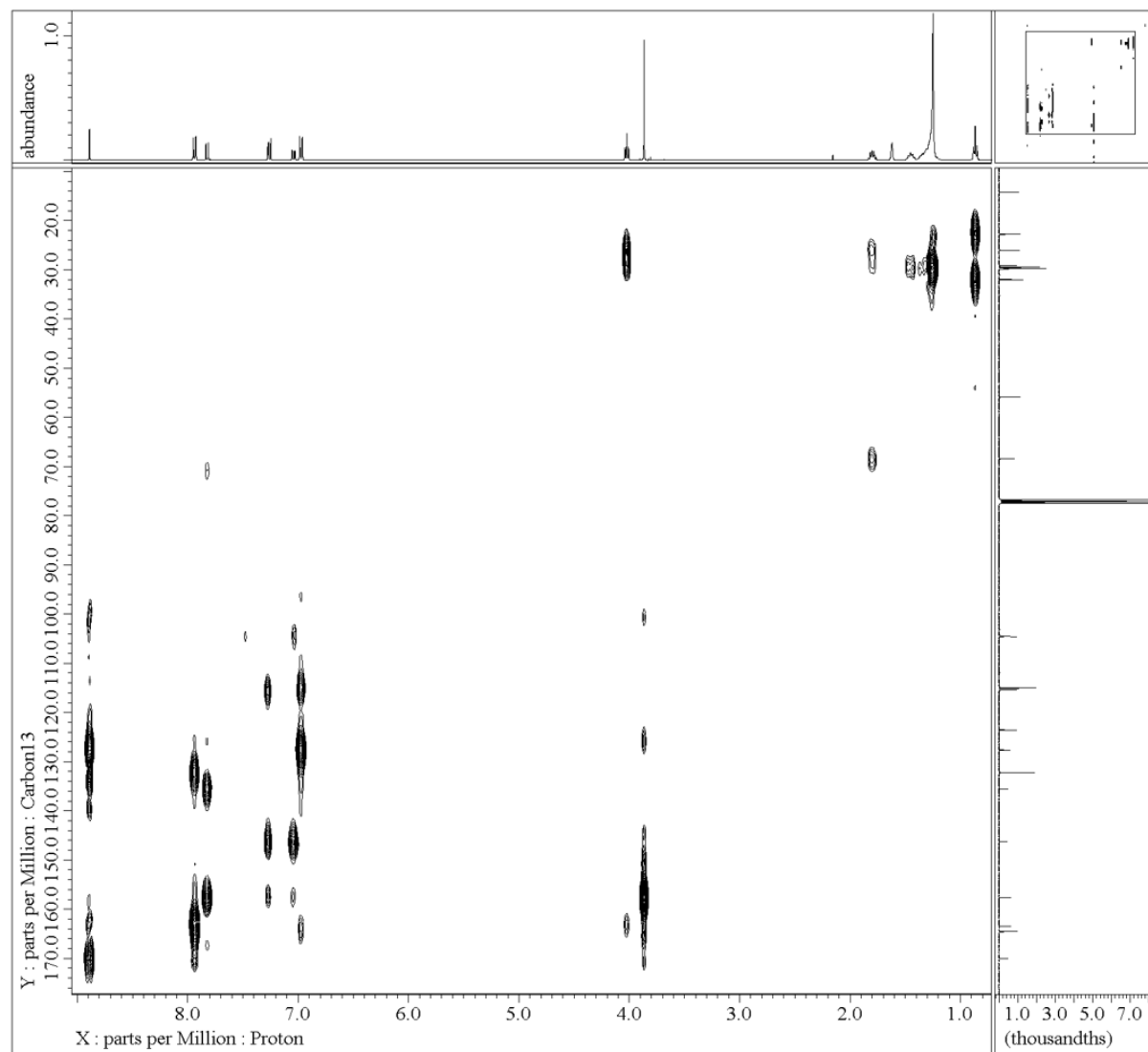
A11  $^{13}\text{C}$  NMR Spectrum of **BRLC14**



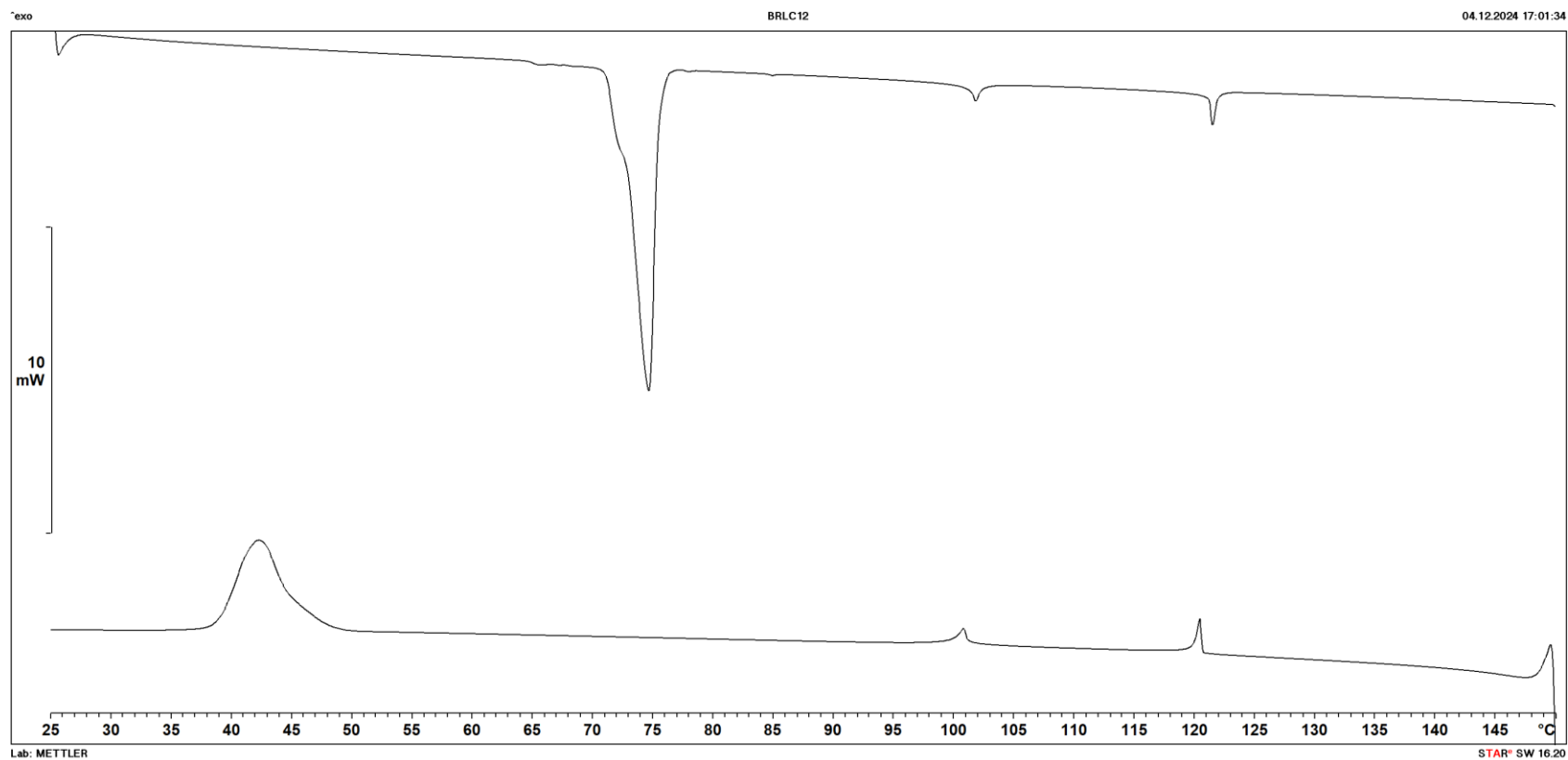
A12 2D COSY NMR Spectrum of **BRLC14**



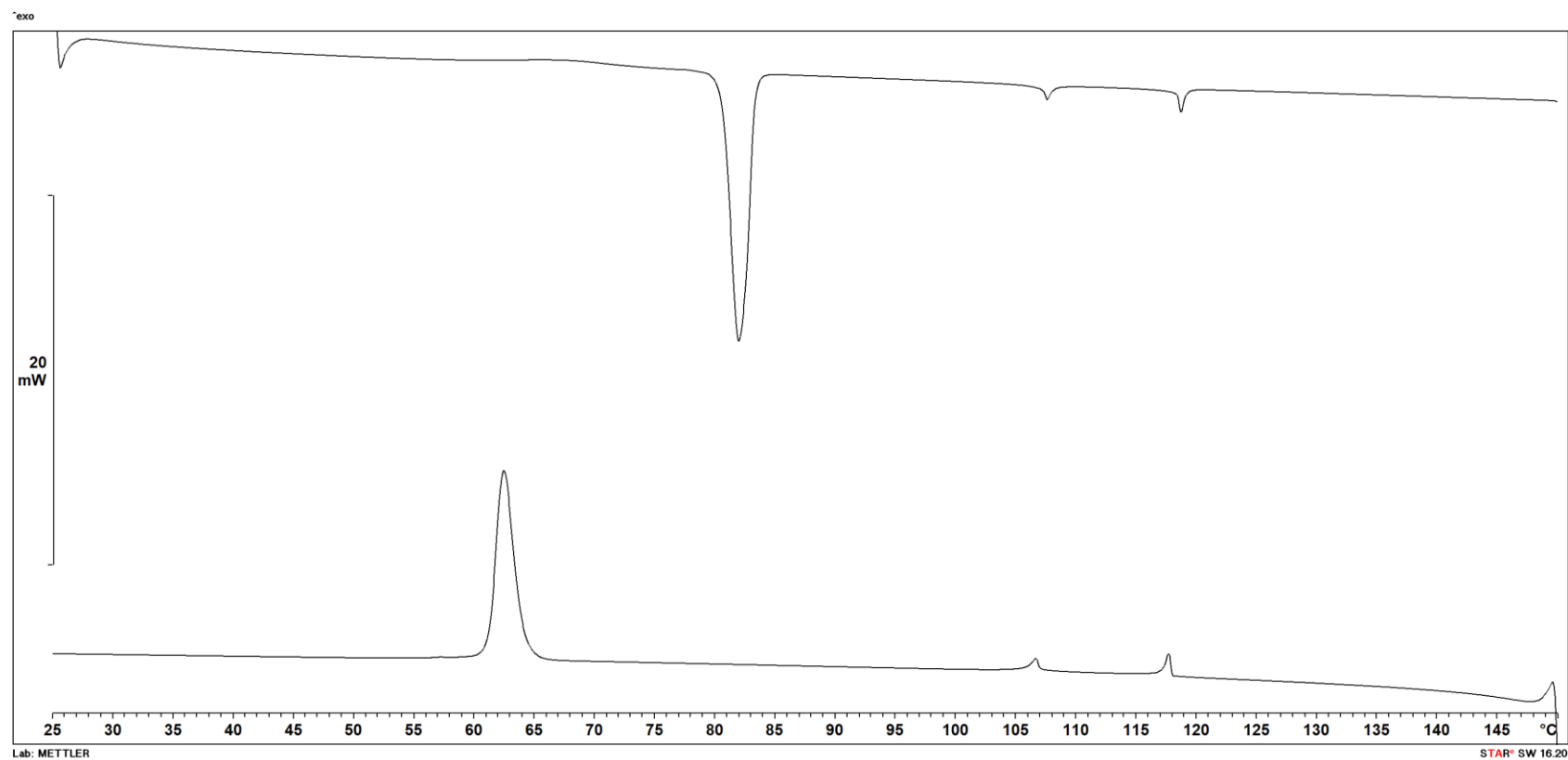
A13 2D HMQC NMR Spectrum of **BRLC14**



A14 2D HMBC NMR Spectrum of **BRLC14**

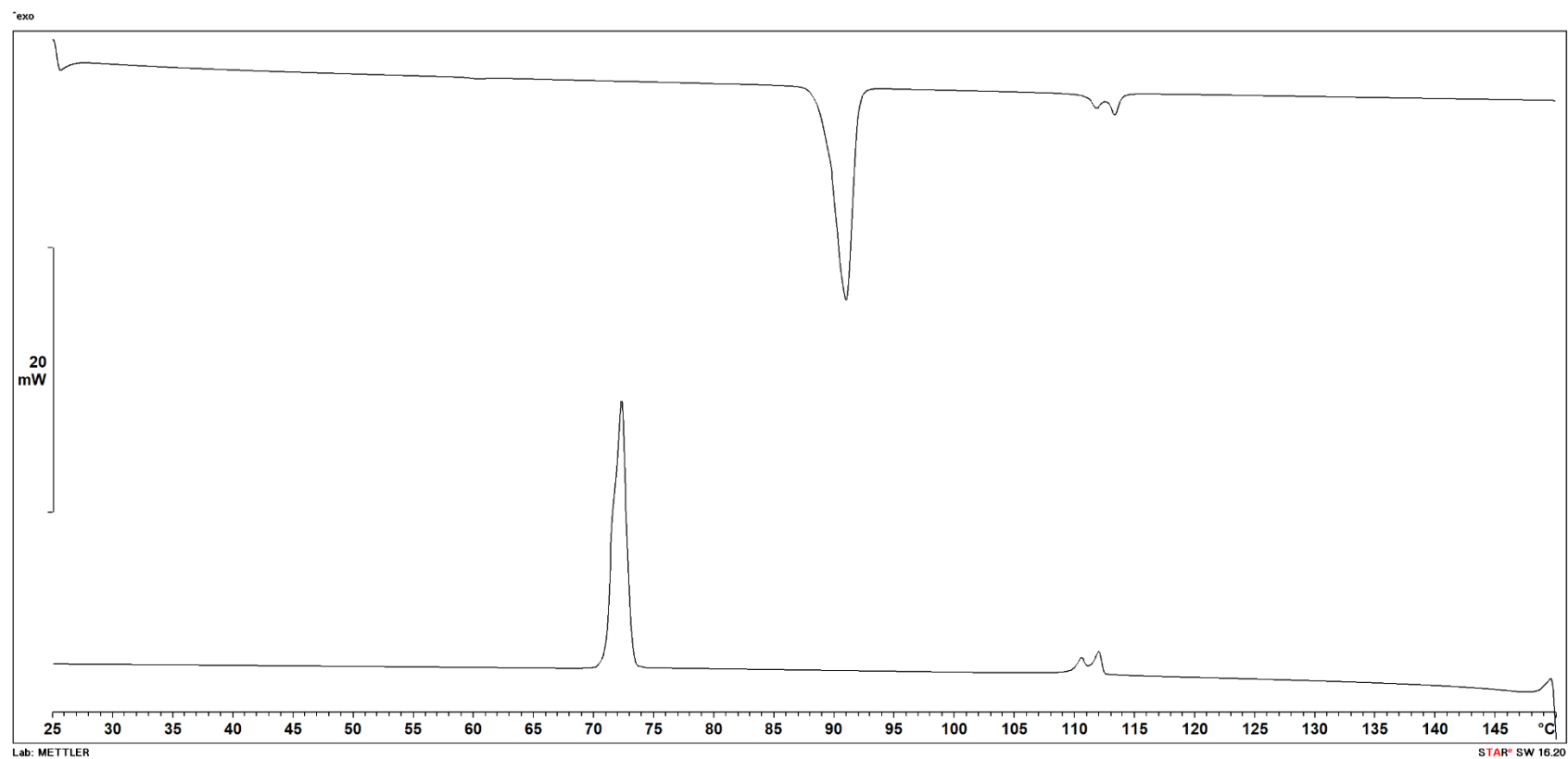


A15 DSC thermogram of **BRLC12**

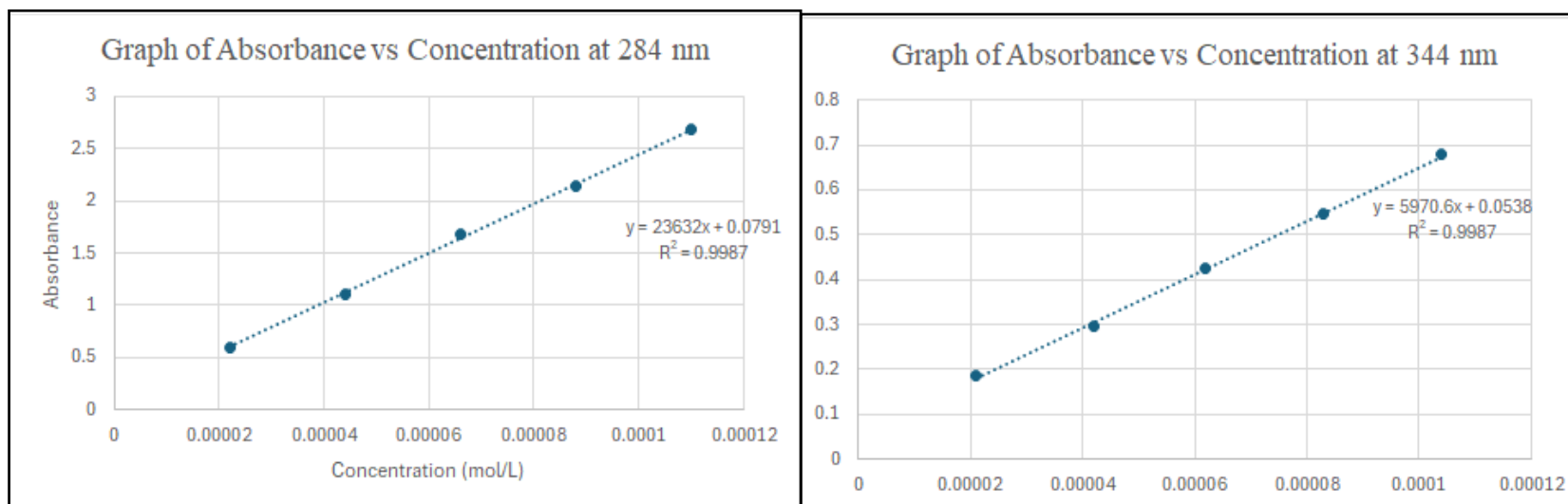


A16 DSC thermogram of **BRLC14**

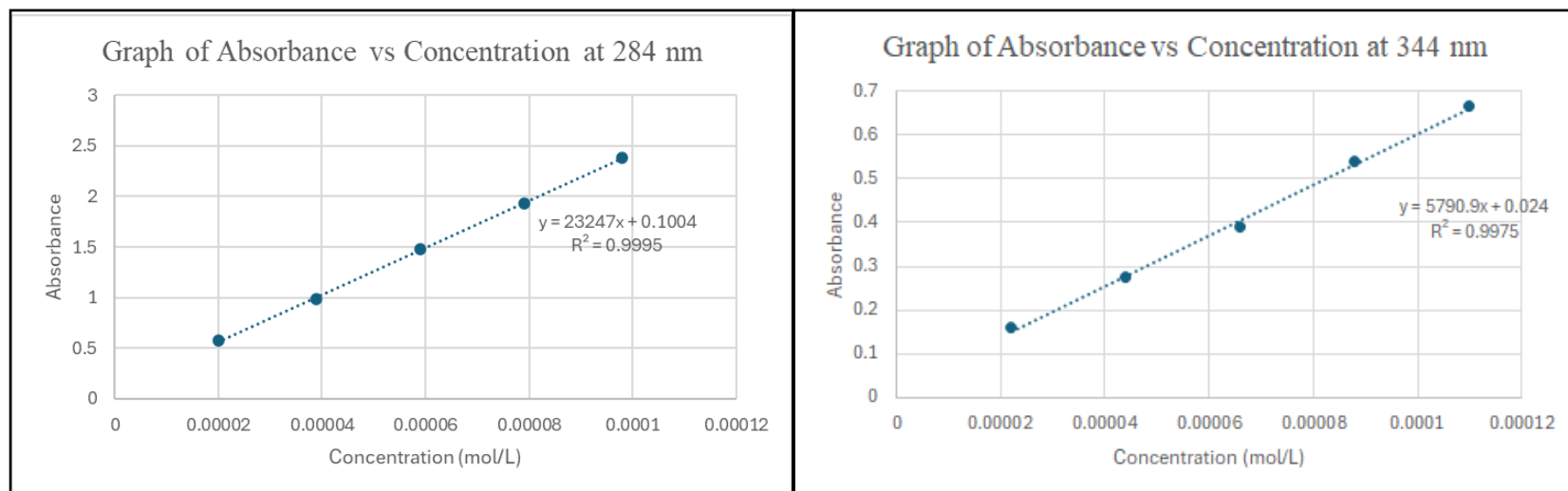




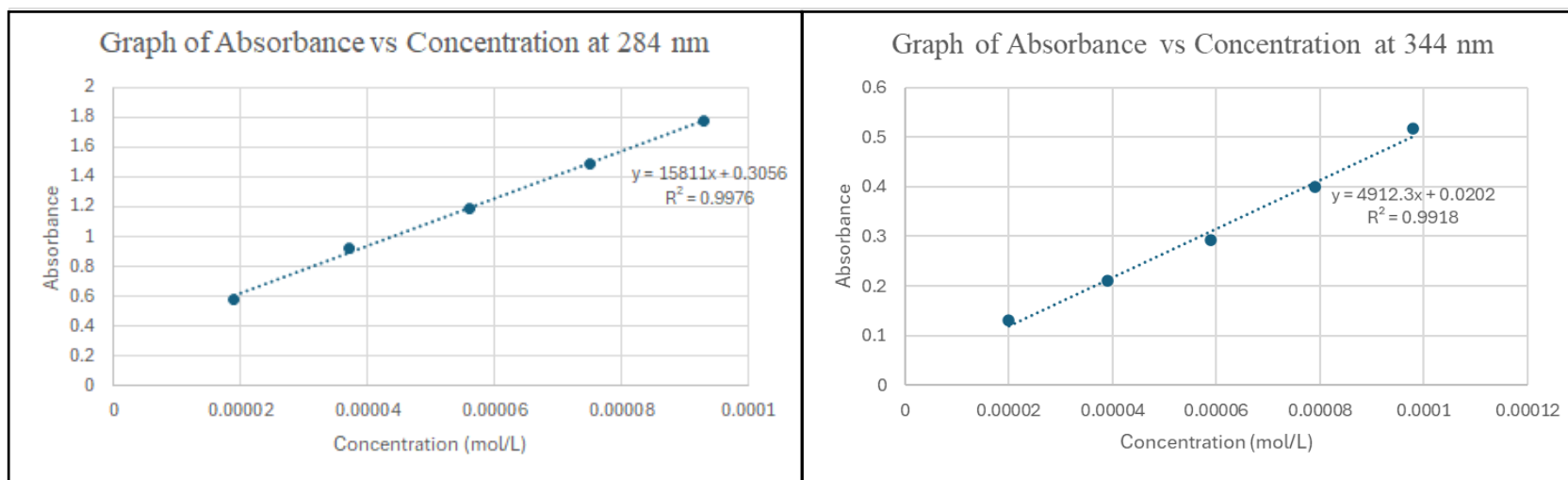
A17 DSC thermogram of **BRLC18**



A18 Graph of absorbance against concentration of **BRLC12** at 284 and 344 nm



A19 Graph of absorbance against concentration of **BRLC14** at 284 and 344 nm



A20 Graph of absorbance against concentration of **BRLC18** at 284 and 344 nm

